University of Naples FEDERICO II
Department of Structural Engineering

PH.D. PROGRAMME IN MATERIALS AND STRUCTURES
COORDINATORS PROFF. D. ACIERNO AND G. MENSITIERI
XXIII CYCLE

EUGENIO CHIOCCARELLI

PH.D. THESIS

DESIGN EARTHQUAKES AND SEISMIC DEMAND FOR PBEE IN FAR-FIELD AND NEAR-SOURCE CONDITIONS

TUTOR PROF. GAETANO MANFREDI
CO-TUTOR DR. IUNIO IERVOLINO

Table of contents

LIST OF FIGURES

CHAPTER 1.
INTRODUCTION

1.1 Motivations

In this thesis the problem of identification of design earthquakes and seismic demand for performance based earthquake engineering (PBEE) is studied referring to far-field and near-source conditions.

Ordinary probability seismic hazard analyses (PSHA), usually referred to far-field conditions, are the base of hazard evaluation of the most advanced seismic codes (e.g. Eurocode 8, 2006, CS.LL.PP. 2008, etc.). PSHA allows to identify for each considered site the probability of exceedance of different ground motion intensity measure (IM) levels in a time interval of interest: choosing a return period, and assuming as IM the elastic spectral acceleration at different structural periods, it is possible to build the uniform hazard spectrum (UHS); i.e., the response spectrum with a constant exceedance probability for all ordinates (Reiter, 1990); e.g., 10% in 50 years in the case of design for life-safety structural performance. UHS is not the only possible PSHA-based design spectrum (e.g., Baker 2011), but it is, to date, the most used basis for the definition of design seismic actions on structures. Recent studies are focused on the possibility of reducing uncertainties of PSHA analyses because it will produce a significant reduction of hazard values.

Despite that, ordinary PSHA and UHS can be considered as a consolidated procedure which is not discussed here.

If the seismic assessment of structures is carried out via non-linear dynamic analysis, knowledge of design response spectra is not enough and selecting the seismic input is seen to be one of the most critical issue which is sometimes considered more important even than structural modeling. In general, the signals that can be used for the seismic structural analysis are of three types: (1) artificial waveforms; (2) simulated accelerograms; and (3) natural records (Bommer and Acevedo, 2004). Spectrum-compatible signals of type (1) are obtained, for example, generating a power spectral density function from a code-specified response spectrum, and deriving signals compatible to that. However, this approach may lead to accelerograms not reflecting the real phasing of seismic waves and cycles of motion, and therefore energy. Simulation records (2) are obtained via modeling of the seismological source and may account for path and site effects but, they often require setting of some rupture parameters, such as the rise-time, which are hard to determine. Finally, of type (3) are ground-motion records from real events. The availability of on-line, user-friendly, databases of strong-motion recordings, and the rapid development of digital seismic networks worldwide, have increased the accessibility to recorded accelerograms, which, therefore, have become the most promising candidates for the seismic assessment of structures (Iervolino and Manfredi, 2008).

In the code approach, selection of natural records has to identify a set compatible with the code-specified spectrum which should include implicitly information about the features of the seismogenic sources determining the seismic hazard at the construction site. Moreover, prudently, the practitioner is often required to also account explicitly for them: for example, Eurocode 8 states that accelerograms should be *adequately qualified with regard to the seismogenetic features of the sources* […]. In practical engineering application, accounting for seismological features of the sources is usually not compatible with information and/or ability of practitioners but, in accordance with probabilistic approach, for a given UHS, *disaggregation* of seismic hazard

(Bazzurro and Cornell, 1999), for the exceedance return period and for the spectral ordinate of interest, allows to identify the contribution to the hazard of each seismological features considered in PSHA. Thus earthquakes dominating the hazard at the site (or *design earthquakes*) may be considered as the events characterized by the seismological features with the maximum contributions to the hazard (McGuire, 1995).

In the first part of this work issues and findings related to identification of design earthquakes are taken to the Italian national level extending preliminary investigations of Convertito et al., 2009 which were referred to a case study region in the Southern Italy. In a recent work of Barani et al. (2009). disaggregation analyses of Italy were presented but different criteria for identification of design earthquakes were chosen.

A large part of results obtained here can be considered independent from the specific sites considered and correlated to the typology of analyses: for example it is discussed how and why design earthquakes change with the spectral period (i.e., the dynamic characteristics of the considered structure), or why return period of seismic action may increase the hazard contribution of moderate events respect to the strong distant earthquakes. Moreover general trends of results for Italian sites are identified and a methodology for extracting one or more design earthquakes given disaggregation results is proposed and discussed. Finally, it is illustrated how these concepts may be easily included in engineering practice complementing design hazard maps and effectively enriching definition of seismic action with relatively small effort. The attention to the practical applicability of presented analyses is summarized in their implementation in an already existing and freely distributed software addressed to the code-based record selection (Iervolino et al., 2010 and Galasso et al. 2010).

In the second part of the work, near-source conditions are considered analyzing the problem of rupture directivity effects. Generally speaking sites that are in a particular geometrical configuration with respect to the rupture may be reached contemporarily by seismic waves generated in different instant of time and velocity fault-normal signals may show a large pulse which occurs

at the beginning of the record and contains the most of energy (Somerville et al., 1997). The results are waveforms different from ordinary ground motions recorded in the far field or in geometrical conditions not favorable with respect to directivity (Singh, 1985 and Reiter, 1990). Current attenuations laws are not able to capture such effect well but, unfortunately, it is believed that structures with dynamic behavior in a range of periods related to the pulse period may be subjected to underestimated seismic demand (Tothong and Cornell, 2006).

So although directivity effects are known since many years to both seismologists and earthquake engineers, many aspects are still to be deepening. A systematic procedure for (i) analyzing resultant signals, (ii) studying structural effects and (iii) including these issues in hazard assessment is still far to be consolidated and as consequence, main European seismic codes do not account for the problem.

In this work an attempt of improving each one of the previous points is presented. Regarding quantification of structural effects, a strong-motions' American database, already classified in pulse-like and non pulse-like signals, is analyzed and three main characteristics of pulse-like records are outlined: (1) the elastic demand is generally larger than that of ordinary recordings, particularly concerning the fault-normal direction; (2) the spectral shape is non-standard with an increment of spectral ordinates in the range around the pulse period; (3) because the pulse period is generally a low frequency one (i.e., in the same order of magnitude of that of the most of common structures) the inelastic demand can be particularly high (Tothong and Luco, 2007) and developed in a comparatively short time which may facilitate fragile collapse mechanisms in structures not properly designed.

Using previous results as benchmark, signals of the recent L'Aquila earthquake mainshock are analyzed investigating if directivity effects occurred. In particular, near-source records from the mainshock, rotated in fault-normal (FN) and fault-parallel (FP) directions, are analyzed extracting pulses with the same procedure used for the NGA dataset. Those found as likely containing velocity pulses were compared to: (1) those not identified as pulse-like; (2) the un-rotated components, and (3) to predictive models for the

occurrence of directivity pulses and for the pulse period. The features of L'Aquila records were also compared to those of the NGA database to check whether they are in agreement to what expected for impulsive and non impulsive near-source records. The analyses include also rupture-rotated and vertical components of motion.

Finally all the recent models regarding pulse-like effects (applied also in the analyses mentioned above) are used for a PSHA which is modified in order to account for near-source conditions (Iervolino and Cornell, 2008). Also disaggregation analysis is adapted to near source conditions as suggested by literatures (Thotong et al., 2007). Illustrative cases are analyzed: they can be considered as some of the first numerical applications of the most recent procedures and they are a way for identifying advantages and limits and for contributing to future improvements.

1.2 Organization of the thesis

In **Chapter 2** a disaggregation analysis of the entire Italian territory is performed proposing a synthetic representation of results based on first and second modal values of disaggregation distribution. Two spectral period (PGA and 1.0sec) and four return periods (50, 475, 975 and 2475 yrs) are considered. Analysis of many single sites are reported pointing out advantages and limits of the modal values. Moreover all the general trends of results (e.g. influence of return period, influence of spectral period, etc.) are discussed. The fundamental role of seismogenetic source model and of adopted ground motion prediction equation are explained.

In **Chapter 3** rupture directivity effects are analyzed looking at Next Generation Attenuation (NGA) database of American ground-motions already classified by Baker (2007) in pulse-like and non-pulse-like records. Main structural effects of directivity influenced signals are analyzed referring to linear and non linear single degree of freedom (SDoF) systems and unexpected inelastic displacement demand are found comparing with ordinary records.

In **Chapter 4** L'Aquila earthquake is considered looking for possible directivity effects. Analysis is also a way to define a simple procedure for detecting directivity effect in single seismic events.

In **Chapter 5** probabilistic seismic hazard analysis is performed in near source condition applying all available models to account for directivity effects and result are compared with those obtained via an ordinary PSHA. Some important consideration are presented about the best way to analyze the problem and the limits of ordinary hazard representation in these particular conditions. Moreover some indications about possible development are obtained in particular referring to the best way of accounting for directivity effects in record selection.

Finally in **Chapter 6** a review of the work and the main conclusions are presented.

References

Baker, J. W. (2007) Quantitative Classification of Near-Fault Ground Motions Using Wavelet Analysis, Bull. Seism. Soc. Am., 97(5), 1486-1501.

Baker, J.W. (2011). "The Conditional Mean Spectrum: A tool for ground motion selection," Journal of Structural Engineering, (in press).

Barani, S., Spallarossa, D. and Bazzurro, P. (2009). Disaggregation of probabilistic ground motion hazard in Italy. Bull. Seismol. Soc. Am. 99, 2638-2661.

Bazzurro, P., and C. A. Cornell (1999). Disaggregation of seismic hazard, Bull. Seismol. Soc. Am. 89, 501–520.

Bommer, J J and Acevedo, A.B. The use of real earthquake accelerograms as input to dynamic analysis. Journal of Earthquake Engineering, Vol.8:43{91, 2004. Special Issue, 1.

Convertito, V., Iervolino, I. and Herrero, A. (2009). Importance of mapping design earthquakes: insights for the southern apennines, Italy. Bull. Seismol. Soc. Am. 99, 2979-2991

CS.LL.PP. (2008). DM 14 gennaio 2008 Norme Tecniche per le Costruzioni. Gazzetta Ufficiale della repubblica Italiana 29 (in Italian).

Eurocode 8 (2006). Design provisions for earthquake resistance of structures. Part 1.3: General rules. Specific rules for various materials and elements. Eur. Comm. for Standardisation, Brussels, Belgium.

Galasso, C., Chioccarelli, E., Iervolino, I. (2010). Advances in record selection for Italian Seismic code, Proc. Of 29° Convegno nazionale GNGTS, Prato, Italy, October 26-28, 2010.

Iervolino I., Manfredi G. (2008). Review of ground motion record selection strategies for dynamic structural analysis. In Modern Testing Techniques of Mechanical and Structural Systems, Oreste S. Bursi, David J. Wagg (Editors), CISM Courses and Lectures 502, Springer.

Iervolino, I., Cornell, C. A. (2008) Probability of Occurrence of Velocity Pulses in Near-Source Ground Motions, Bull. Seism. Soc. Am., 98(5), 2262-2277.

Iervolino, I., Galasso, C., Cosenza, E. (2010b). REXEL: computed aided record selection for code-based seismic structural analysis. Bulletin of Earthquake Engineering, 8, 339-362.

McGuire, R. 1995. Probabilistic seismic hazard analysis and design earthquakes: Closing the loop. Bulletin of the Seismological Society of America, 85: 1275-1284

Reiter, L. (1990) Earthquake Hazard Analysis, Issues and Insights, Columbia University Press, NY.

Singh, P. J. (1985) Earthquake Ground Motions: Implications for Designing Structures and Reconciling Structural Damage, Earthquake Spectra 1(2), 239-270.

Somerville, P. G., Smith, N. F., Graves, R.W., Abrahamson, N. A. (1997) Modification of Empirical Strong Motion Attenuation Relations to Include the Amplitude and Duration Effect of Rupture Directivity, Seism. Res. Lett., 68(1), 199-122.

Thotong, P., Cornell, C. A., and Baker, J. W. (2007). Explicit directivity-pulse inclusion in probabilistic seismic hazard analysis, earthquake Spectra 23, 867-891.

Tothong, P., Cornell C. A. (2006) Probabilistic Seismic Demand Analysis Using Advanced Ground Motion Intensity Measures, Attenuation

Relationships, and Near Fault Effect, PEER Report 2006/11, Pacific Earthquake Engineering Reserch Center, Berkeley, CA.

Tothong, P., Luco, N. (2007) Probabilistic seismic demand analysis using advanced ground motion intensity measures, Earthquake Eng. Struct. Dyn., 36, 1837–1860.

CHAPTER 2.
DESIGN EARTHQUAKES FOR ITALIAN SITES

2.1 Introduction

Earthquake resistant design in international seismic codes widely relies on a target spectrum to define seismic actions on structures. Being a representation of ground motion, the design spectrum should include implicitly information about the features of the seismogenic sources determining the seismic hazard at the construction site. On the other hand, along with matching the design spectrum, prudently, the practitioner is often required to also account explicitly for them, for example, when dealing with ground motion record selection for seismic structural analysis. For example, Eurocode 8 (CEN, 2003) states: *in the range of periods between $0.2T_1$ and $2T_1$, where T_1 is the fundamental period of the structure in the direction where the accelerogram will be applied, no value of the mean 5% damping elastic spectrum, calculated from all time histories, should be less than 90% of the corresponding value of the 5% damping elastic response spectrum*. Moreover, accelerograms should be *adequately qualified with regard to the seismogenetic features of the sources* […].

While the design spectrum is assigned by the code, it is unlikely that the engineer has the information and/or is able to qualify the input ground

motions with respect to the seismological features of the sources. However, if the design spectrum is derived from probabilistic seismic hazard analysis (PSHA), it is possible to obtain design earthquakes in terms of magnitude and location (and others). In fact, PSHA allows to identify for each considered site the probability of exceedance of different ground motion intensity measure (IM) levels in a time interval of interest: choosing a return period, and assuming as IM the elastic spectral acceleration at different structural periods, it is possible to build the uniform hazard spectrum (UHS); i.e., the response spectrum with a constant exceedance probability for all ordinates (Reiter, 1990); e.g., 10% in 50 years in the case of design for life-safety structural performance.

UHS is not the only possible PSHA-based design spectrum (e.g., Baker 2011), but it is, to date, the basis for the definition of design seismic actions on structures currently in the most advanced seismic codes (e.g., CS.LL.PP., 2008). In fact, the Italian seismic code is based on the work of the *Instituto Nazionale di Geofisica e Vulcanologia* (INGV) which, computed uniform hazard spectra (UHS) over a grid of more than 10000 points for 9 return periods (Tr) (from 30 to 2475 years) and 10 spectral ordinates, from 0.1 to 2.0 sec (http://esse1.mi.ingv.it/). As consequence, design spectra are a close approximation of the UHS of each Italian site.

If UHS is the design spectrum, *disaggregation* of seismic hazard (Bazzurro and Cornell, 1999) for the exceedance return period for the spectral ordinate of interest allows to identify the values of some characteristics providing the largest contributions to the hazard in terms of exceeding a specified spectral ordinate value. These events may be referred to as the earthquakes dominating the seismic hazard in a probabilistic sense, and may be used as design earthquakes as conceptually sketched by McGuire (1995). In a previous work (Convertito et al., 2009) the authors preliminarily investigated this topic referring to a case-study region in southern Italy. Herein, the issues and findings related to identification of design earthquakes are taken to a national level as in Italy the code relies completely on PSHA to define design spectra yet giving limited, if any, information about design earthquakes. Then,

it may be useful to develop tools based on disaggregation which allow the practitioner to identify the scenario seismic events of interest (e.g., maps of design earthquakes) as also suggested by Bommer (2004).

In the presented study design earthquakes are identified disaggregating the probabilistic seismic hazard, computed for two spectral ordinates, intended to represent the short and long period portions of the response spectrum, and four return periods, in terms of the values of magnitude (M), source to site distance (R) and ε (the number of standard deviations that the ground motion parameter is away from its median value estimated by the assumed attenuation relationship) providing the largest contributions to the hazard in terms of exceeding a specified IM value[1]. It is shown first that, for the most Italian sites, two design earthquake exist, a moderate close one and a strong distant one, and it is explained why this depend on modeling of seismic sources and of ground motion prediction equations considered in PSHA.

Along with mapping of design events, results of the study include discussion of how and why design earthquakes change with the spectral period (i.e., the dynamic characteristics of the considered structure), the return period of the seismic action and with relative distance to seismogenic zones. It is also demonstrated why the contribution of the moderate event increases with the return period with respect to the strong distant earthquake.

Finally, it will be illustrated how maps of design earthquakes may be easy yet useful complements to design acceleration maps, for both ordinary and advanced engineering practice.

2.2 Methodology

Given a seismic source model, probabilistic seismic hazard analysis (PSHA) provides, for a selected site, the hazard curve representing the probability of exceedance of a ground motion intensity measure IM in a time

[1] In principle other source features considered (e.g., faulting style, hanging/foot wall, etc) yet their relevance with respect to engineering practice is not fully proven to date.

interval of interest. Starting from PSHA results, disaggregation is a procedure which allows the decomposition of a selected point on the hazard curve identifying the hazard contribution of each vector {M, R, ε}. Analytically disaggregation's result is the joint probability density function (PDF) of {M, R, ε} conditional to the exceedance of a IM threshold of interest (IM_0), Eq. (1).

$$f\left(m,r,\varepsilon\left|IM>IM_0\right.\right)=\frac{\sum_{i=1}^{N_{sources}}\alpha_i I\left[IM>IM_0\left|m,r,\varepsilon\right.\right]\cdot f\left(m,r,\varepsilon\right)}{\sum_{i=1}^{N_{fault}}E_i\left(IM>IM_0\right)} \quad (1)$$

In Eq. (1) I is an indicator function that equals 1 if IM is larger than IM_0 for a given distance r, magnitude m, and ε, N_{source} is the number of seismic sources relevant for the hazard at the site, α_i is the earthquake occurrence probability for the fault i, $E_i\left(IM>IM_0\right)$ is the probability of exceeding IM_0 (i.e, the hazard) due to the fault i.

It is clear how computing $f\left(m,r,\varepsilon\left|IM>IM_0\right.\right)$ requires hazard information and, on the other hand, having available such PDF allows to identify the {M, R, ε} triplets of the most contributing, in a frequentistic sense, the hazard at the site. Therefore, it is the basis of the study presented in the following. Because disaggregation results may change with the considered spectral period, in this work design earthquakes were computed for two different spectral accelerations[2], Sa, at 0 sec (i.e., peak ground acceleration or PGA) and 1.0 sec in order to account for short and long period response spectrum regions.

To perform disaggregation it is required to compute hazard first for the two IM considered. Both PSHA and disaggregation analyses were performed by a Fortran program specifically developed and used first in Convertito et al. (2009). The whole country was discretized using the same grid of about 10760 points adopted by INGV and, therefore, by the Italian seismic code (distance

[2] INGV also indirectly provides data about the seismic scenarios mostly contributing to the hazard, but only referring to peak ground acceleration (PGA) values of UHSs.

between close points is about 5 km). The modeling of seismogenic zones is that of Meletti et al. (2008), also adopted by INGV (Figure 2.1) and seismic parameters of each zone are those used by Barani et al. (2009), reported in Table 2.1.

According to Ambraseys et al. (1996), which is the ground motion prediction equation (GMPE) considered, magnitude is that of surface waves (Ms). Because soil site classification are not available for all sites, all the analyses refer to rock or stiff soil conditions. Assuming a uniform epicenter distribution in each seismogetic zones, epicentral distance distribution is that appropriate, but because used GMPE is referred to closest horizontal distance to the surface projection of the fault plane (R_{jb}) as defined by Joyner and Boore (1981), the former was converted into the latter via the linear relationship given in *Gruppo di Lavoro* (2004). Distance applicability limits of Ambraseys et al. (1996) GMPE were respected and earthquakes distant more than 200 km from the site were neglected in the hazard computation. Hazard was computed with respect to four return periods, Tr, corresponding to the reference limit states for civil and strategic structures (50, 475, 975 and 2475 years).

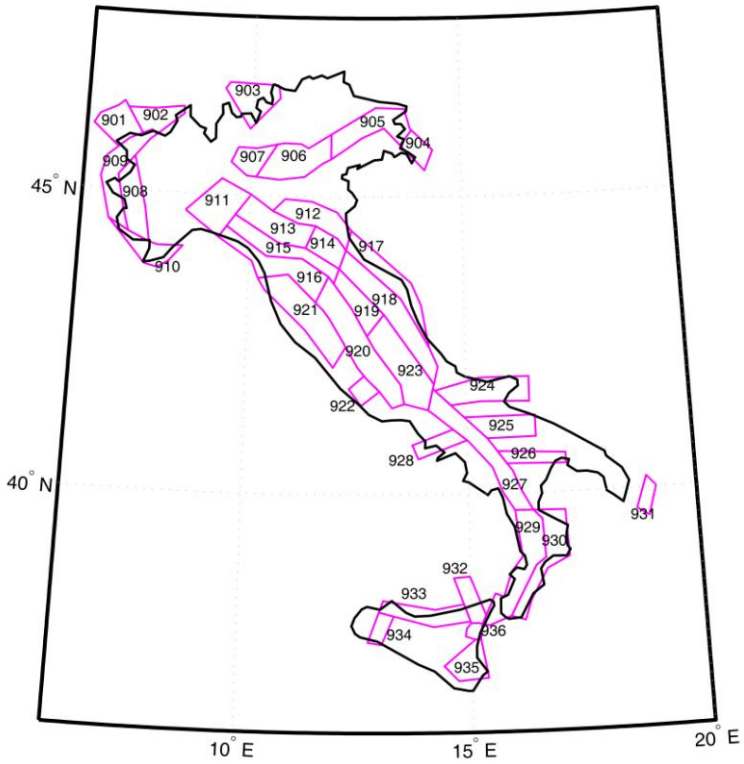

Figure 2.1*. Seismogenetic zones for Italy according to Meletti et al. (2008).*

Table 2.1. *Characterization of seismic sources according to Barani et al. (2009). For each zone it is provided: minimum (M_{min}) and maximum magnitude (M_{max}); annual rate of earthquake occurrence above $M_{min,}$ (υ); and negative slope of Gutenberg-Richter relationship (b).*

Zone	M_{min}	M_{max}	υ	b
901	4.3	5.8	0.045	1.133
902	4.3	6.1	0.103	0.935
903	4.3	5.8	0.117	1.786
904	4.3	5.5	0.050	0.939
905	4.3	6.6	0.316	0.853
906	4.3	6.6	0.135	1.092
907	4.3	5.8	0.065	1 396
908	4.3	5.5	0.140	1.408
909	4.3	5.5	0.055	0.972
910	4.3	6.4	0.085	0.788
911	4.3	5.5	0.050	1.242
912	4.3	6.1	0.091	1.004

913	4.3	5.8	0.204	1.204
914	4.3	5.8	0.183	1.093
915	4.3	6.6	0.311	1.083
916	4.3	5.5	0.089	1.503
917	4.3	6.1	0.121	0.794
918	4.3	6.4	0.217	0.840
919	4.3	6.4	0.242	0.875
920	4.3	5.5	0.317	1.676
921	4.3	5.8	0.298	1.409
922	4.3	5.2	0.090	1.436
923	4.3	7.3	0.645	0.802
924	4.3	7.0	0.192	0.945
925	4.3	7.0	0.071	0.508
926	4.3	5.8	0.061	1.017
927	4.3	7.3	0.362	0.557
928	4.3	5.8	0.054	1.056
929	4.3	7.6	0.394	0.676
930	4.3	6.6	0.146	0.715
931	4.3	7.0	0.045	0.490
932	4.3	6.1	0.118	0.847
933	4.3	6.1	0.172	1.160
934	4.3	6.1	0.043	0.778
935	4.3	7.6	0.090	0.609
936	3.7	5.2	0.448	1.219

2.3 PSHA's Results

Hazard curves were computed using thirty values[3] of the IMs equally distributed between 0.001g and 1.5g. Computed hazard maps for the two spectral ordinates and the four return periods are reported in Figure 2.2 and Figure 2.3.

Although computing hazard is not the primary scope of this study, in order to validate these results, and therefore to provide a sound basis for the following disaggregation analysis, INGV hazard was considered as benchmark; it considers an elaborated logic-tree accounting for two earthquake

3 Results' accuracy and computational effort are both dependent on IM discretization, even if with opposite trends. Authors' choice of thirty points, was a compromise that seems to provide trends of results generally acceptable.

catalogs, two different seismic rate model and maximum magnitude estimation, and four attenuation models (Stucchi et al., 2010). Although the simplicity of hazard scheme used herein, hazard results are in good general agreement with those of INGV. Finally a complete comparison between computed results and INGV data is reported in Figure 2.4 and 2.5 where maps of differences are shown for PGA and Sa and for all return period considered in this work.

However, an explicit and therefore more direct comparison of disaggregation results of this study and those of INGV is given in Section 2.4.6, for those cases when the latter is available.

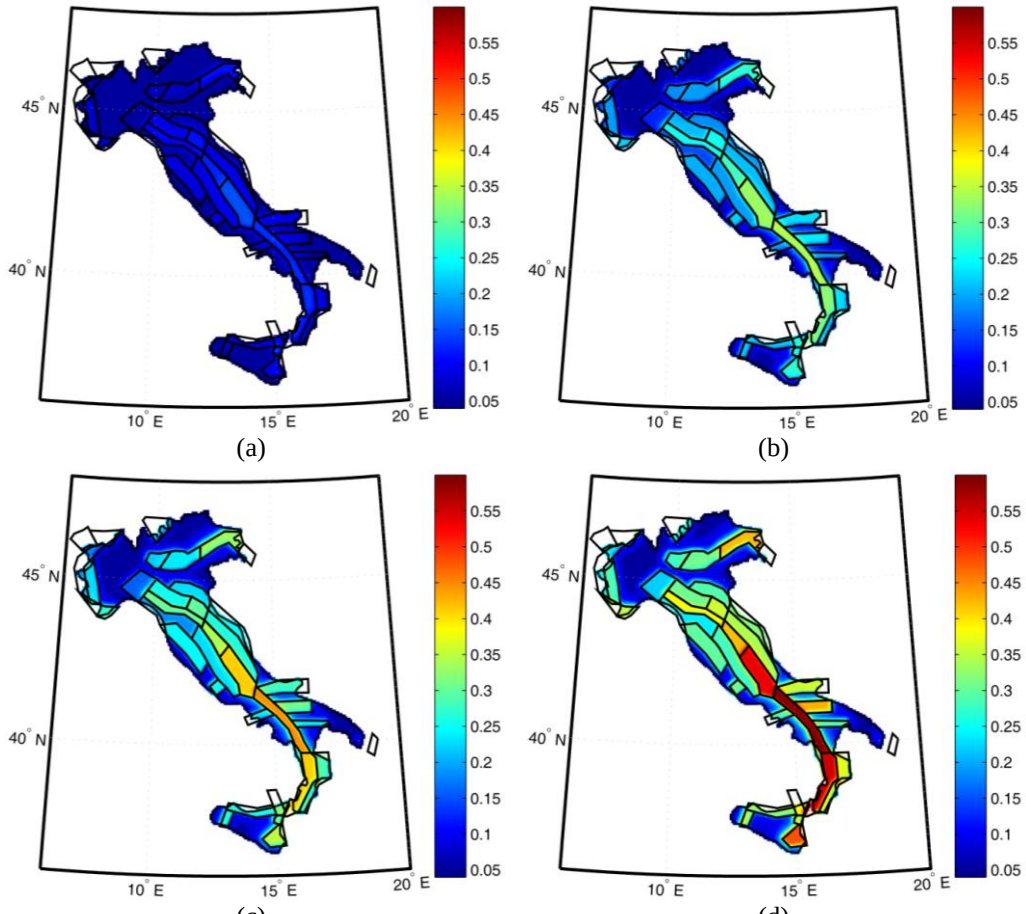

Figure 2.2. *Hazard maps of PGA (in g) for Tr equal to 50 (a), 475 (b), 975 (c) and 2475(d) years.*

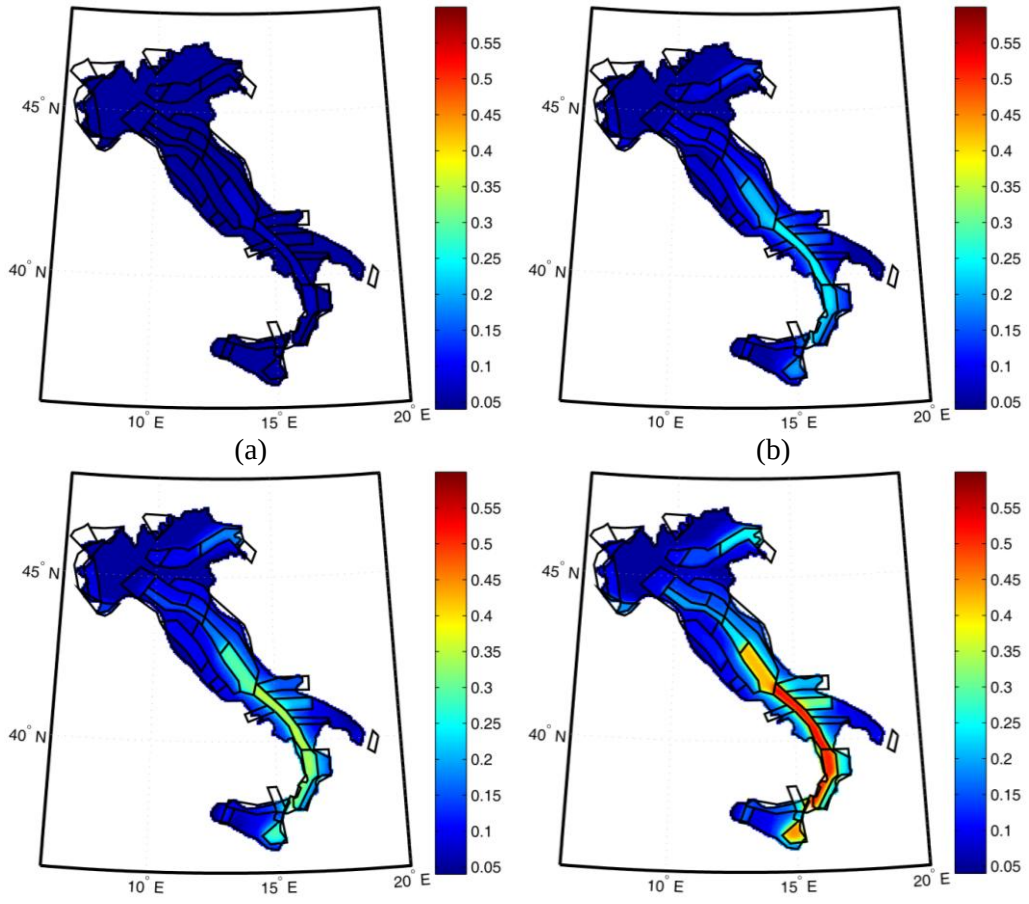

***Figure 2.3**. Hazard maps of Sa(T=1.0sec) (in g) for Tr equal to 50 (a), 475 (b), 975 (c) and 2475(d) years.*

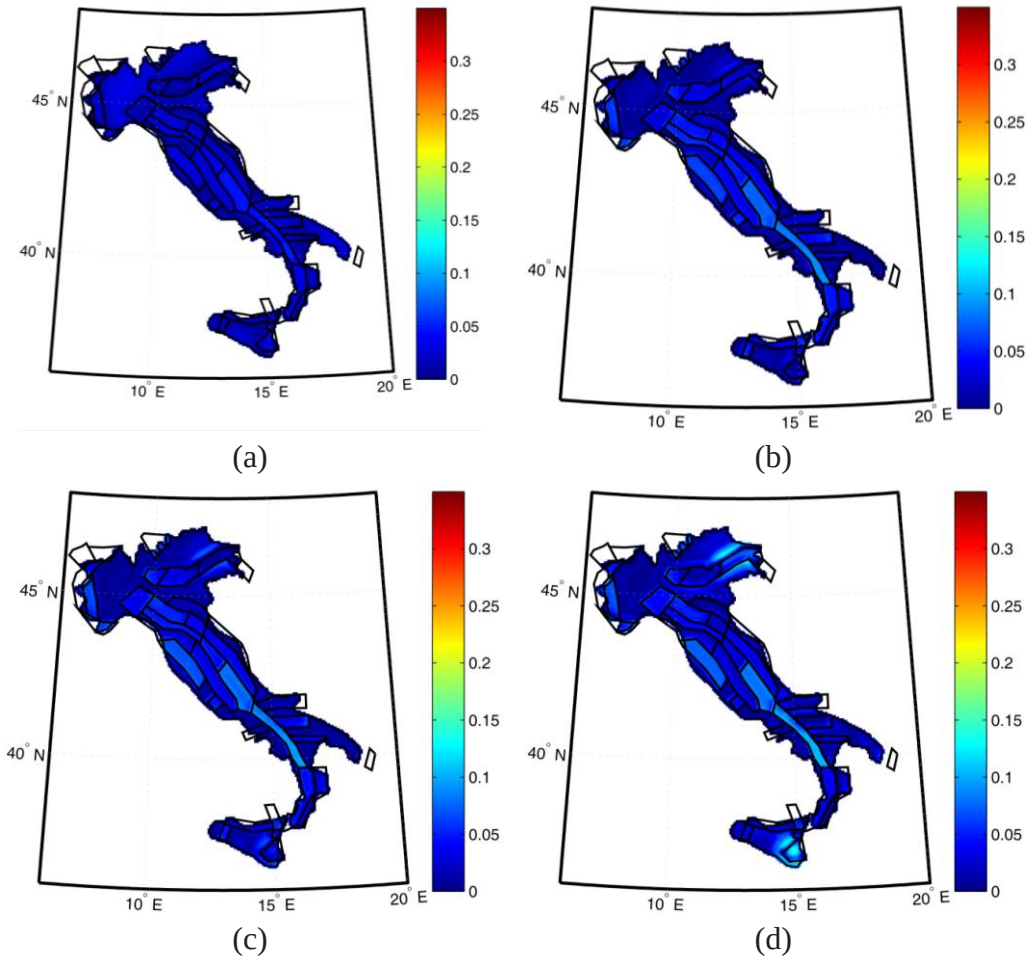

***Figure 2.4**. Differences between INGV and computed hazard values (in g) for PGA: Tr=50 (a), 475 (b), 975 (c) and 2475yrs (d).*

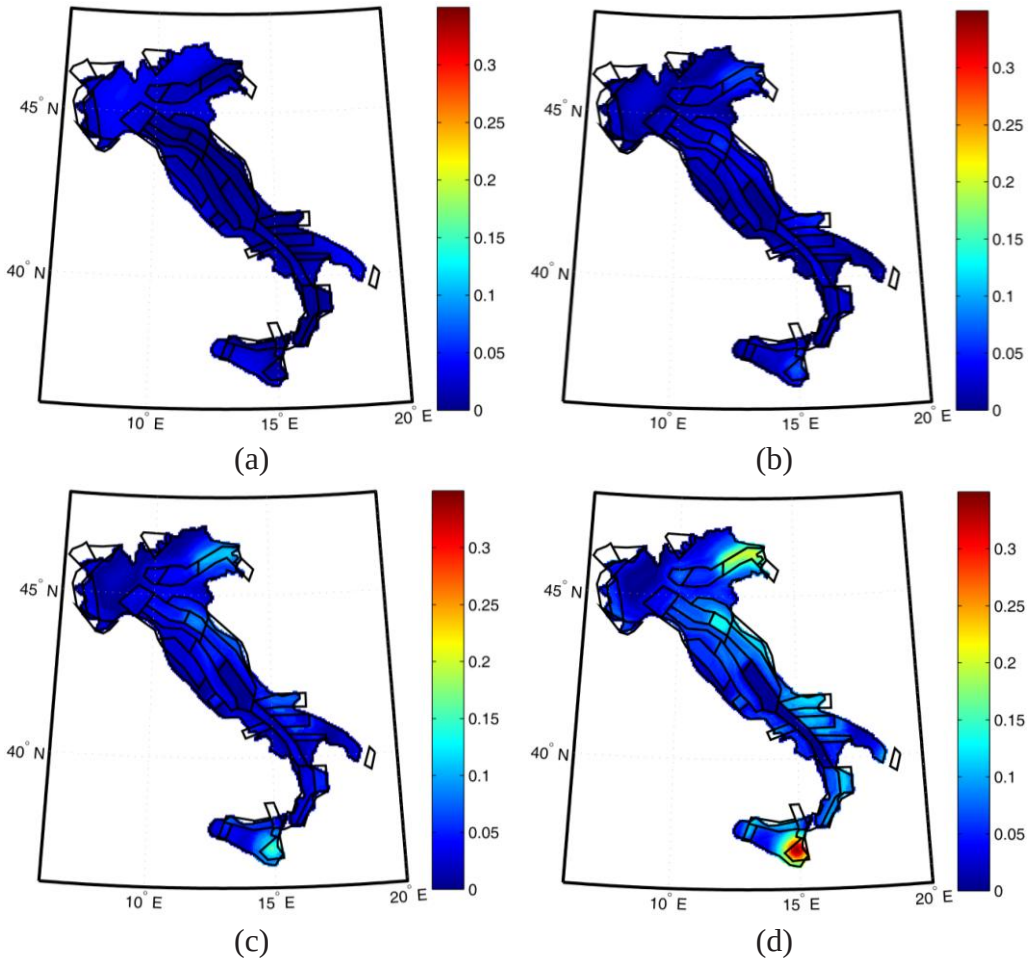

Figure 2.5. *Differences between INGV and computed hazard values (in g) for Sa(1.0sec): Tr=50 (a), 475 (b), 975 (c) and 2475yrs (d).*

It has also to be noted that some regions with low seismicity (e.g., Northern Italy) are subjected to little increments of hazard increasing Tr. In fact, results for these sites may be more affected by the chosen discretization of IM axis in the construction of the hazard curves. Results for Pavia, in the Northern Italy, are reported as a numerical example. In Table 2.2 values of PGA and Sa computed with the original discretization of the hazard curves and with a double discretization (60 point equally distributed between 0.001g and 1.5g) are compared. Also INGV hazard values are reported in the table. The

higher discretization provides results closer to the INGV ones but the computation time associated to the second choice is too high to be applied to all Italian region. Because hazard results have to be considered as a preliminary step of this study and the main object of the work is related to design earthquakes, another revision of discretization influence will be reported referring to disaggregation results.

Table 2.2. *Hazard results for Pavia, Northern Italy.*

			PGA [g]				Sa (T=1sec) [g]			
N. points of IM	Long.	Lat.	Tr = 50	Tr = 475	Tr = 975	Tr = 2475	Tr = 50	Tr = 475	Tr = 975	Tr = 2475
30	9.16	45.19	0.0520	0.0837	0.1030	0.1500	0.0517	0.0526	0.0527	0.0527
60	9.16	45.19	0.0264	0.0736	0.0101	0.0147	0.0260	0.0341	0.0455	0.0533
INGV	9.16	45.19	0.025 - 0.050	0.050 - 0.075	0.075 - 0.100	0.100 - 0.125	< 0.025	0.025 - 0.050	0.050 - 0.075	0.075 - 0.100

2.4 First and second design earthquakes'maps

Disaggregation integral in Eq. 1 is computed numerically by the software using bins of 0.05, 1.0 and 0.5 for M, R and ε respectively (minimum and maximum values used for ε are -3 and +3). This means that the disaggregation PDF, which is continuous in principle, is computed as a discrete function.

The maps given in Figures from 2.6 to 2.29 show the *design earthquakes* obtained from disaggregation. In fact, as mentioned, for each site, return period and spectral ordinate, disaggregation result is a four dimensional surface providing the contribution to hazard of M, R and ε variables. In order to map such results, synthetic informations representative of the main disaggregation results are required. Therefore, the *first* design earthquake is defined as the first mode of the joint PDF; i.e., the components of the vector {M*, R*, ε*} with the maximum contribution to the frequency of exceedance of the IM threshold considered. Moreover, as extensively discussed in

Convertito et al. (2009), because analyses show that in many cases disaggregation PDF has more than a single mode significantly contributing to hazard, a *second* design earthquake is defined as the second relative maximum of the $f\left(m,r,\varepsilon|IM>IM_0\right)$ distribution (see also Section 2.4.1 and 2.4.5 for a discussion). First and second mode are chosen as synthetic parameters representing design earthquakes and they are reported in the following plots. Herein, to ensure the second design earthquake to be of practical relevance, two additional (arbitrary) conditions were imposed for its identification:

1. The second mode is identified as an event different from the first design earthquake if the two earthquakes differ of 5.0 km in distance and/or 0.25 in magnitude.
2. The second design earthquake is considered as such if the second mode of the disaggregation PDF gives a contribution to hazard larger than 10^{-4}.

Condition 1 is to assure different design earthquakes from a seismological perspective, and the second one to have a significant second design scenario.

Looking at disaggregation maps it is possible to identify some general trends: (i) the first mode corresponds to an earthquake caused by the closer source (or the source the site is enclosed into) and with low-to-moderate magnitude, (ii) the second mode accounts for the influence of the more distant zones usually with larger magnitude, and (iii) moving from PGA to Sa, the number of sites with two design earthquakes increases. As consequence of (ii) and (iii), it can be inferred that the influence of more distant zones is higher for Sa than for PGA.

Each of these conclusions will be deepened and explained via case studies referring to specific sites in the following. It may be anticipated that, of course, all disaggregation results can be motivated looking at GMPE and seismogenetic model adopted; however, because most of the ordinary GMPEs have similar trends, of crucial importance is the model adopted for seismic sources. In other words, using another GMPEs, it is believed that results may have change only slightly without losing general trends. Conversely, changing the seismic source model can alter results dramatically.

For all the site-specific case studies reported below, disaggregation surfaces will be shown in 3D; i.e., after marginalization of $f\left(m,r,\varepsilon\left|IM>IM_0\right.\right)$ with respect to ε so to obtain $f\left(m,r\left|IM>IM_0\right.\right)$; i.e., Eq. 2. Despite this choice, modal values presented are always computed on the four-dimensional disaggregation surface[4].

$$f\left(m,r\left|IM>IM_0\right.\right)=\int_{\varepsilon} f\left(m,r,\varepsilon\left|IM>IM_0\right.\right)d\varepsilon \qquad (2)$$

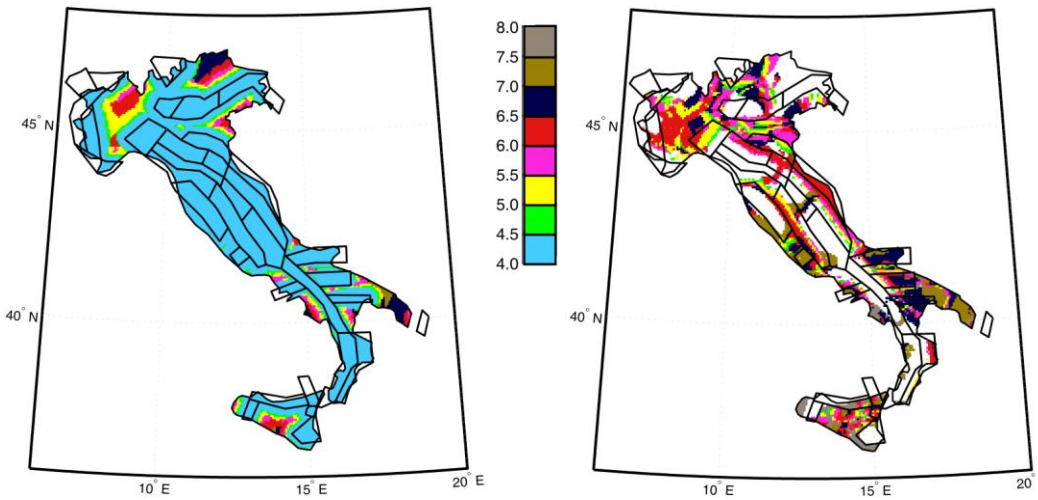

Figure 2.6*. First (left) and second (right) modal values of magnitude for PGA and Tr=50yrs.*

[4] Adopted bins in the plots and integration on the ε values may cause little difference between modal values computed by the software and the same values graphically individuated from the plots.

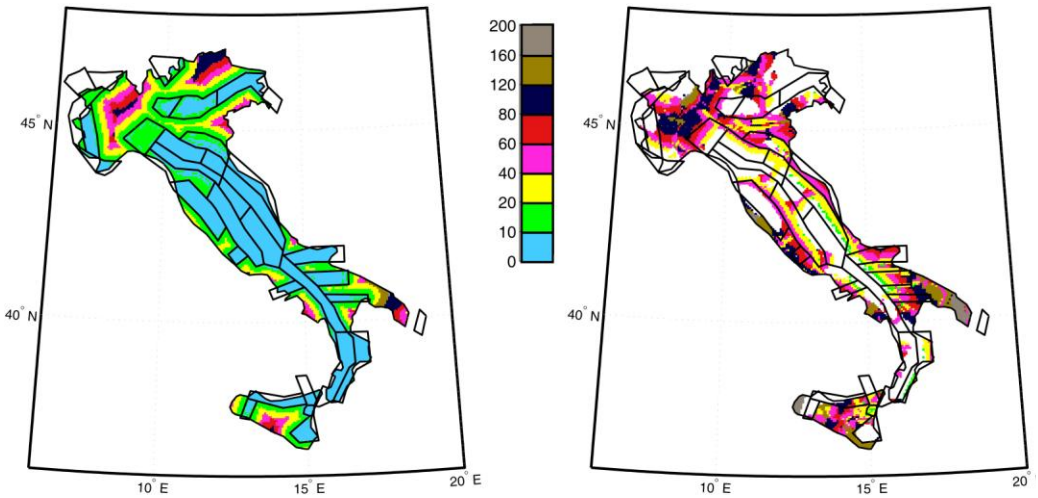

Figure 2.7*. First (left) and second (right) modal values of distance (in km) for PGA and Tr=50yrs.*

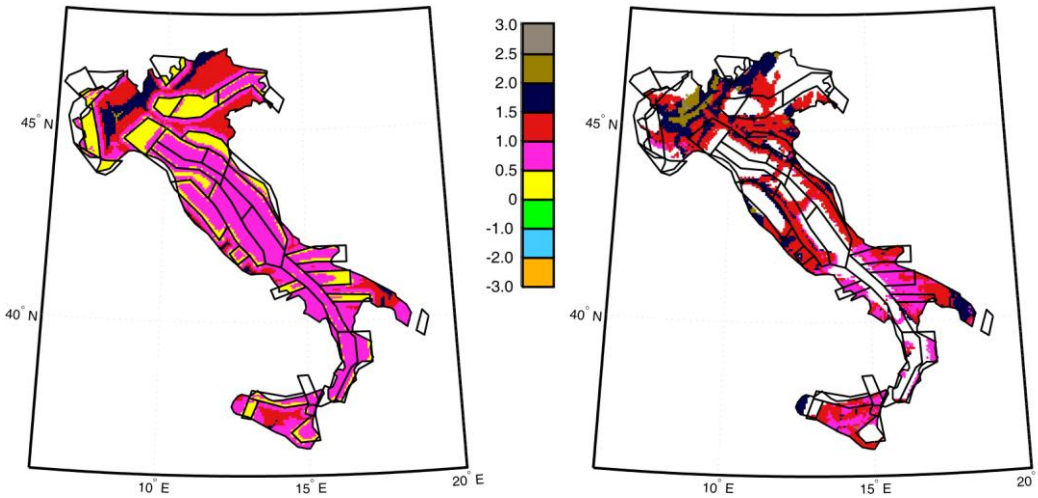

Figure 2.8*. First (left) and second (right) modal values of ε for PGA and Tr=50yrs.*

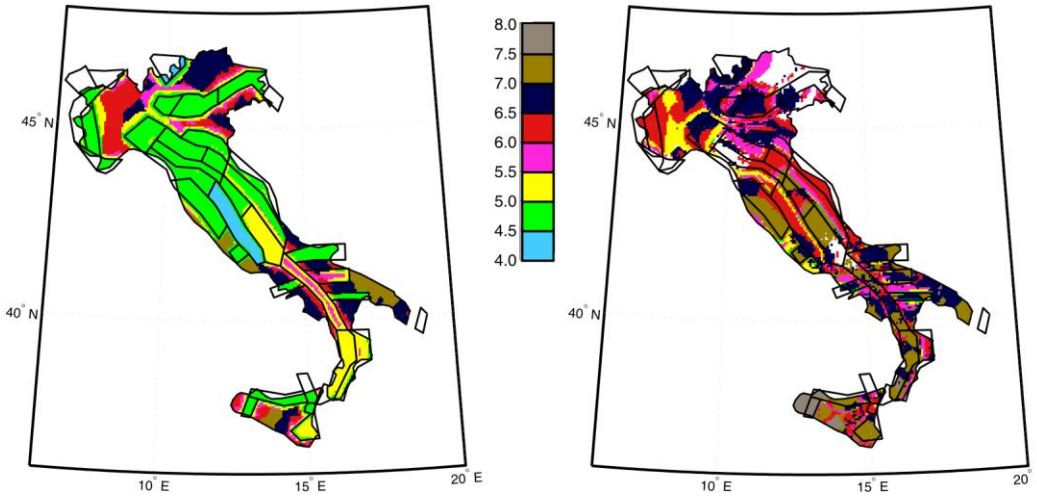

Figure 2.9.*. First (left) and second (right) modal values of magnitude for Sa and Tr=50yrs.*

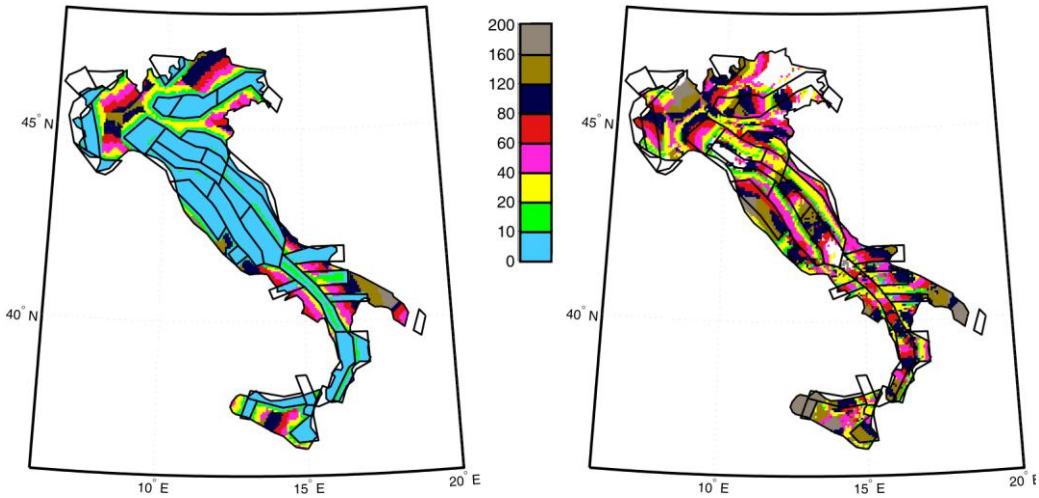

Figure 2.10*. First (left) and second (right) modal values of distance (in km) for Sa and Tr=50yrs.*

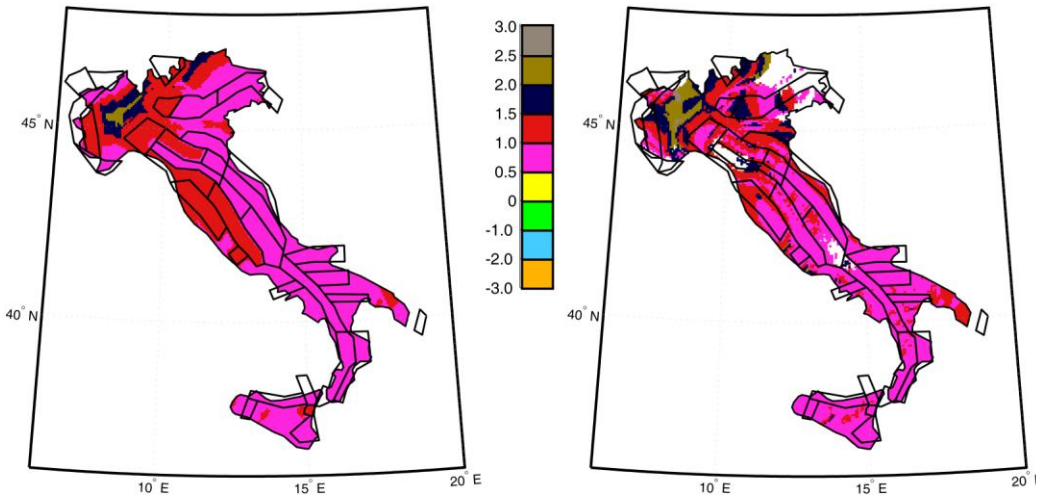

Figure 2.11. *First (left) and second (right) modal values of ε for Sa and Tr= 50yrs.*

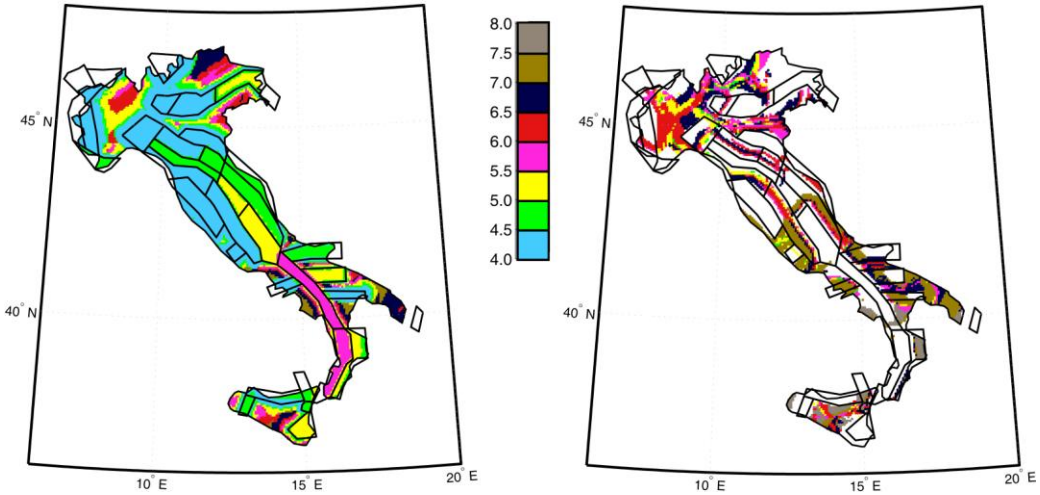

Figure 2.12. *First (left) and second (right) modal values of magnitude for PGA and Tr=475yrs.*

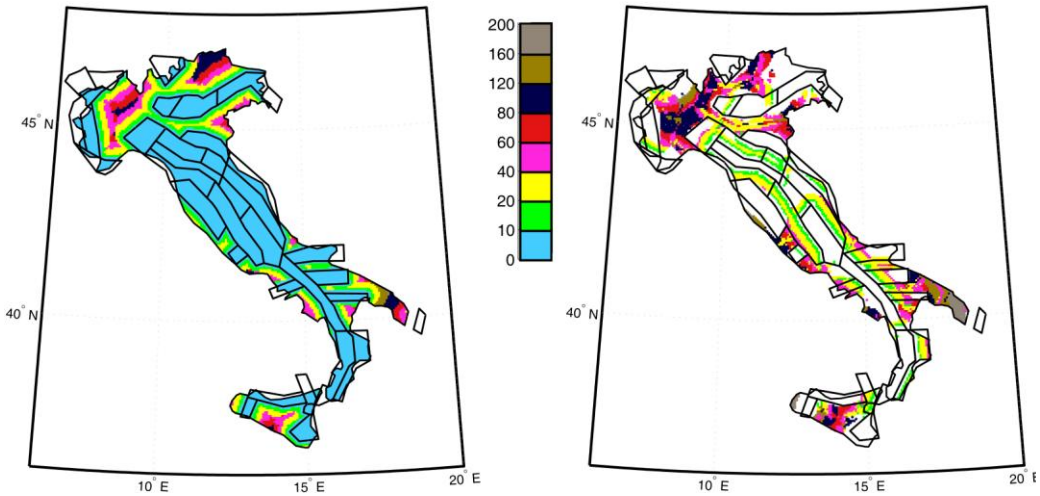

***Figure 2.13**. First (left) and second (right) modal values of distance (in km) for PGA and Tr=475yrs.*

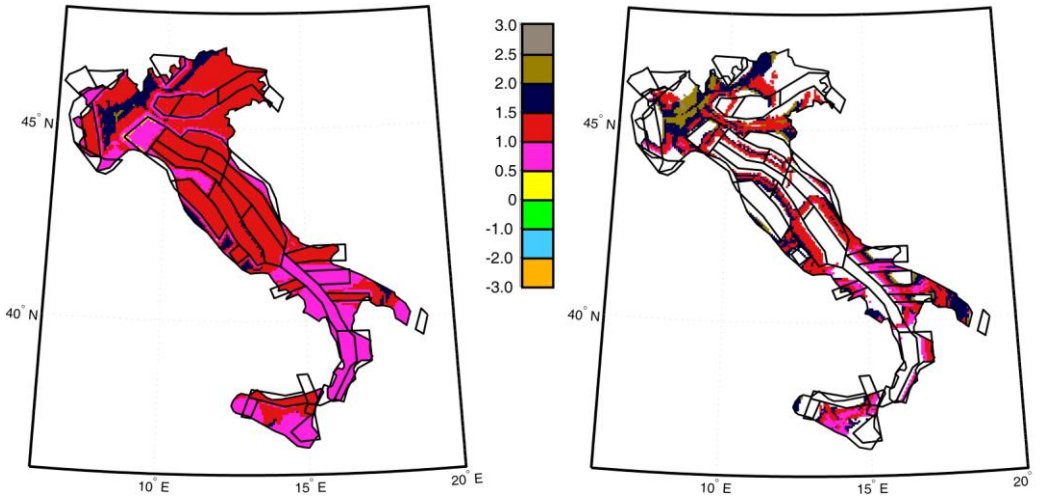

***Figure 2.14**. First (left) and second (right) modal values of ε for PGA and Tr=475yrs.*

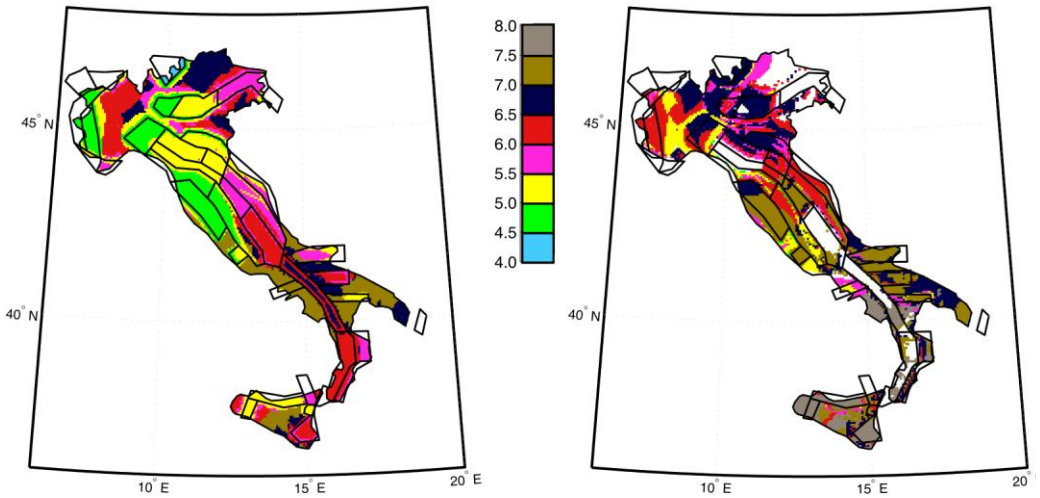

Figure 2.15. *First (left) and second (right) modal values of magnitude for Sa and Tr=475yrs.*

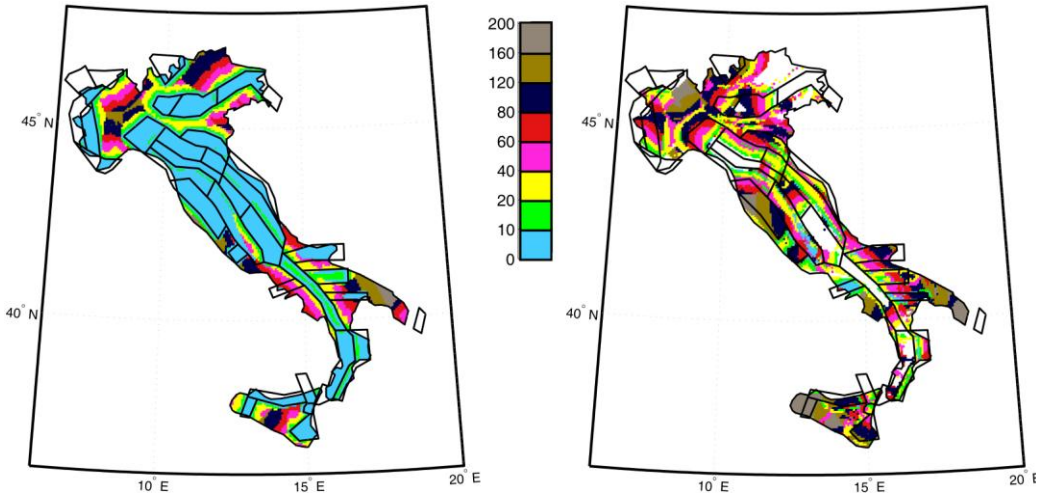

Figure 2.16. *First (left) and second (right) modal values of distance (in km) for Sa and Tr=475yrs.*

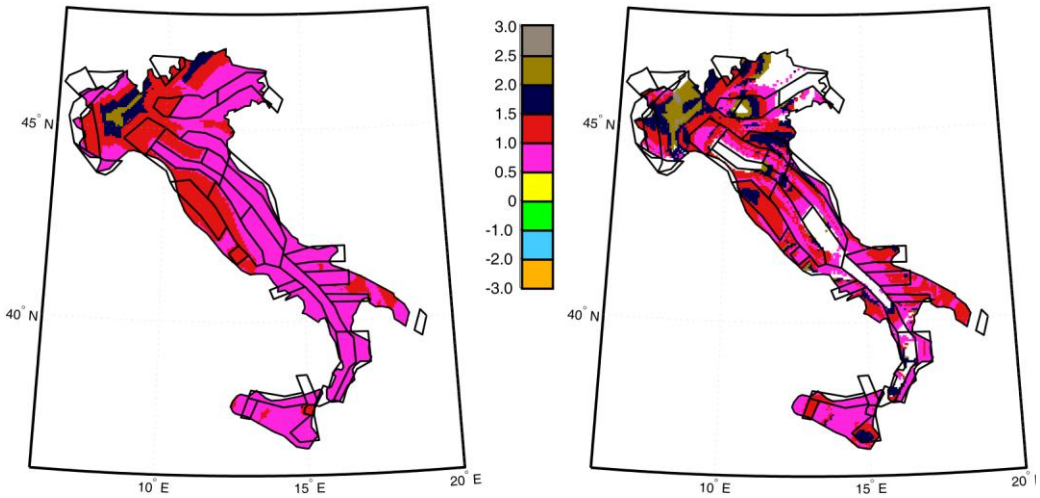

***Figure 2.17**. First (left) and second (right) modal values of ε for Sa and Tr=475yrs.*

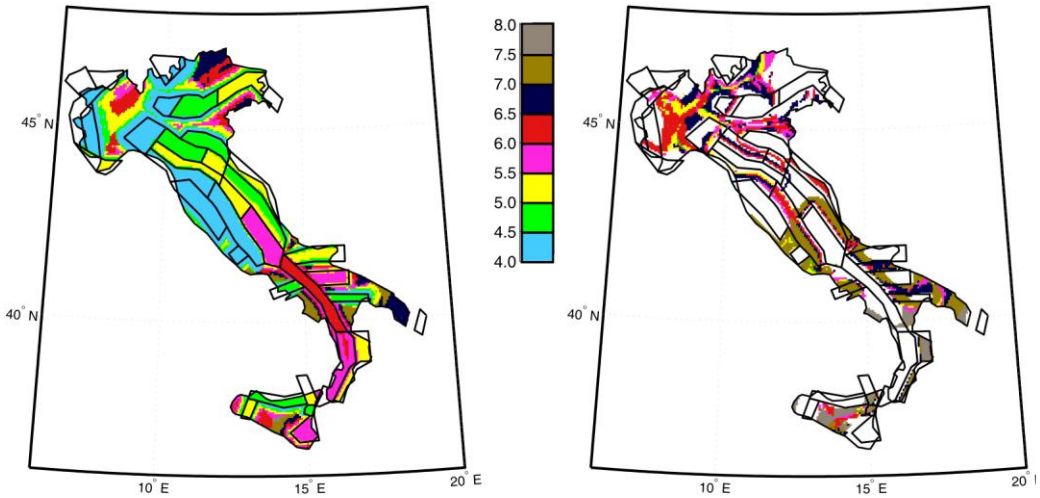

***Figure 2.18**. First (left) and second (right) modal values of magnitude for PGA and Tr=975yrs.*

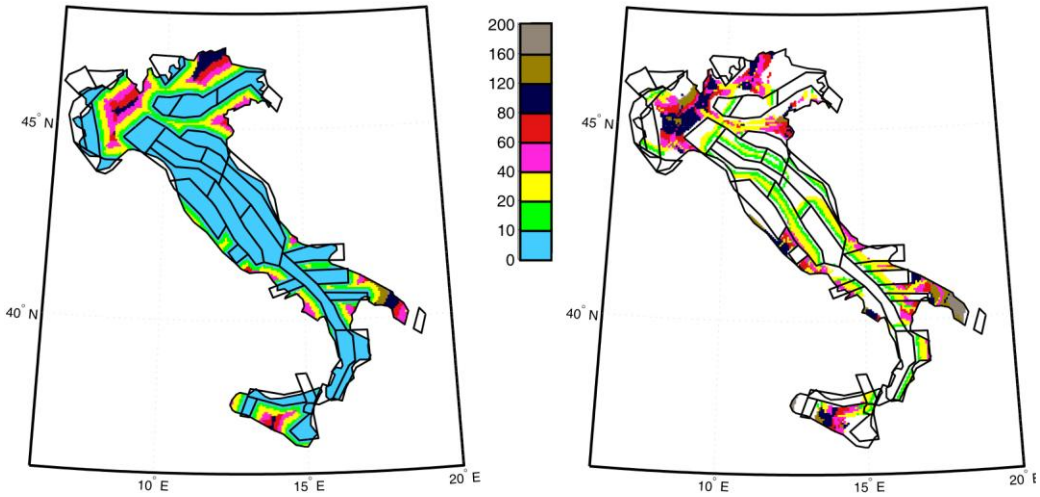

***Figure 2.19**. First (left) and second (right) modal values of distance (in km) for PGA and Tr=975yrs.*

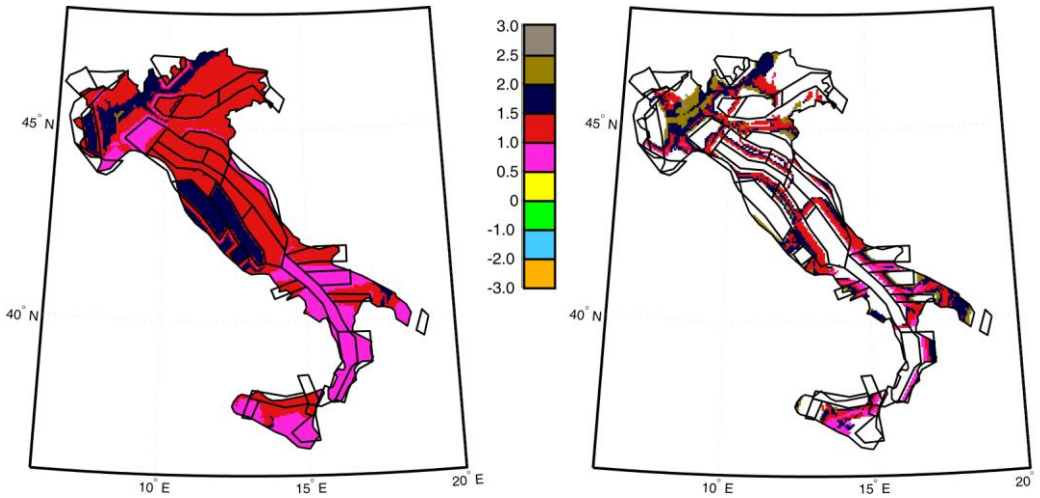

***Figure 2.20**. First (left) and second (right) modal values of ε for PGA and Tr=975yrs.*

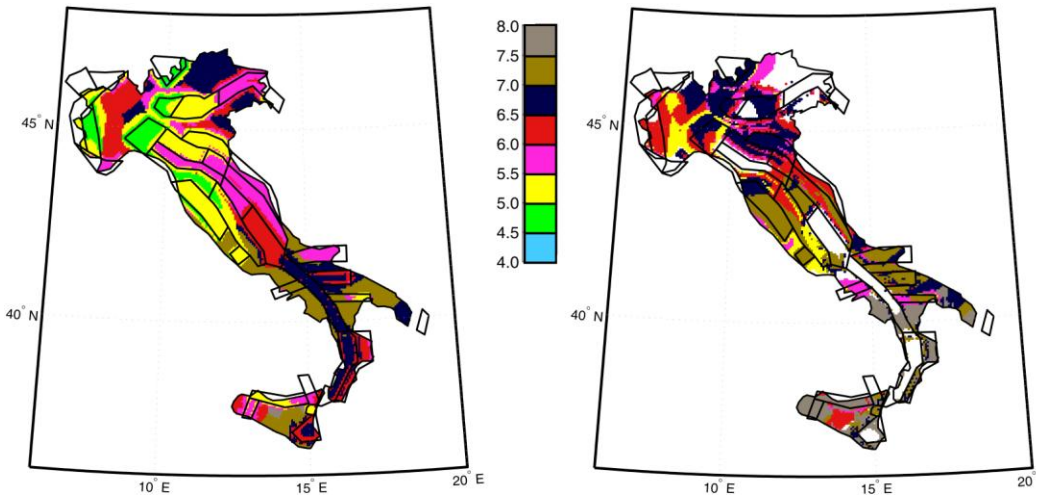

Figure 2.21. *First (left) and second (right) modal values of magnitude for Sa and Tr=975yrs.*

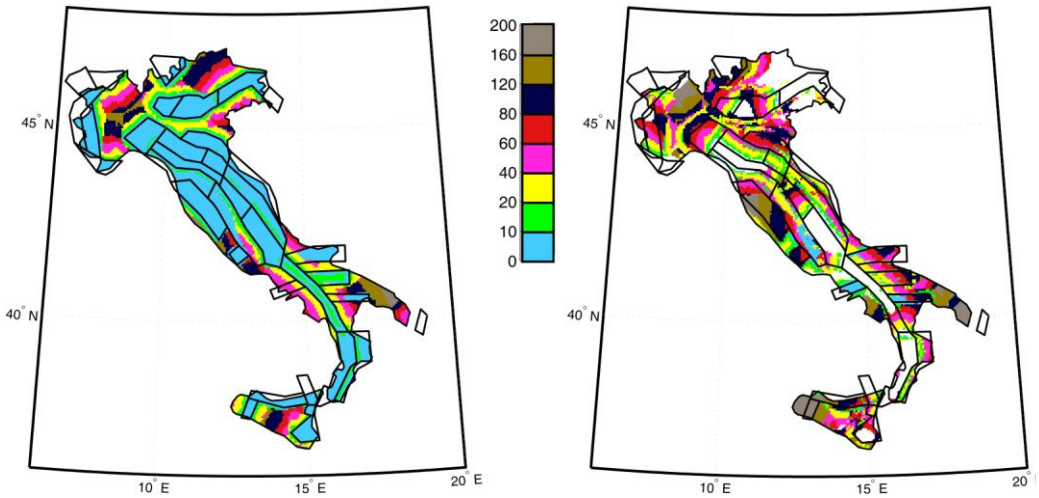

Figure 2.22. *First (left) and second (right) modal values of distance (in km) for Sa and Tr=975yrs.*

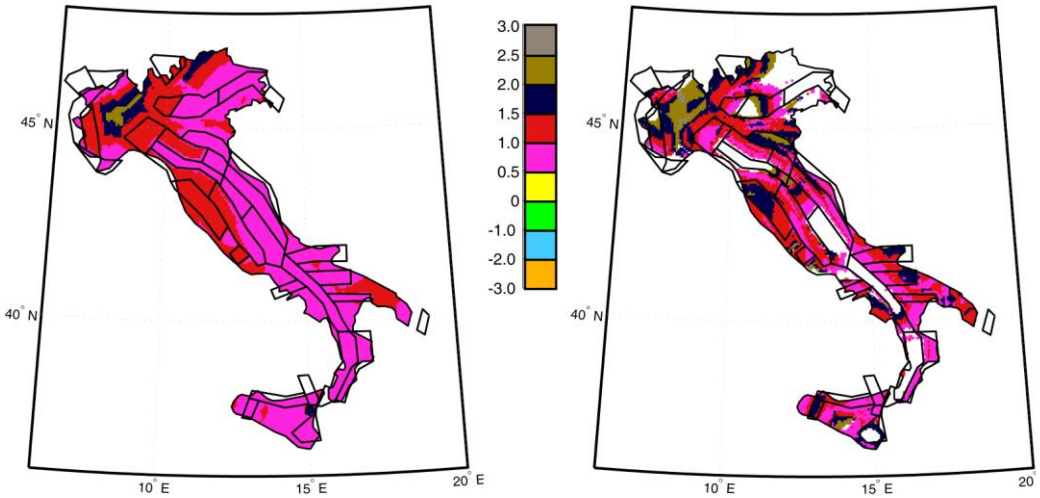

Figure 2.23. *First (left) and second (right) modal values of ε for Sa and Tr=975yrs.*

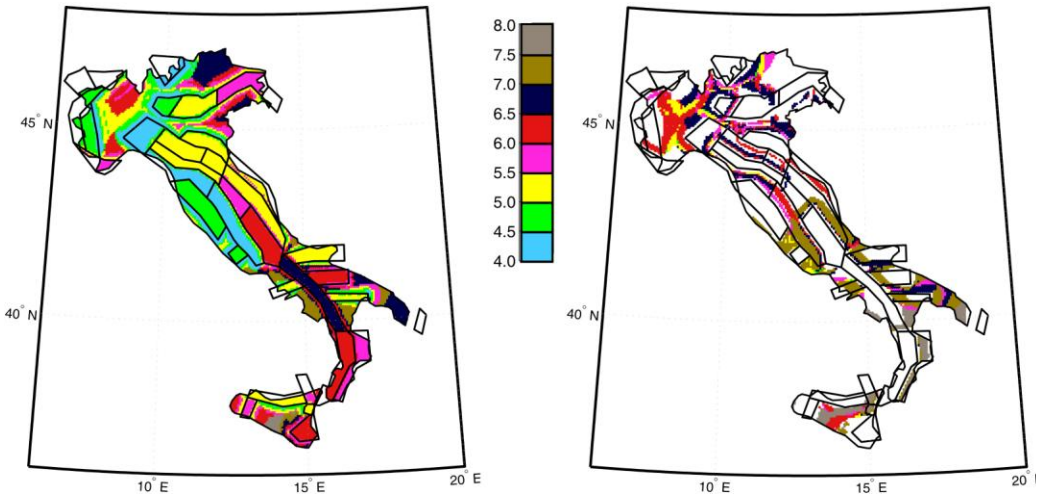

Figure 2.24. *First (left) and second (right) modal values of magnitude for PGA and Tr=2475yrs.*

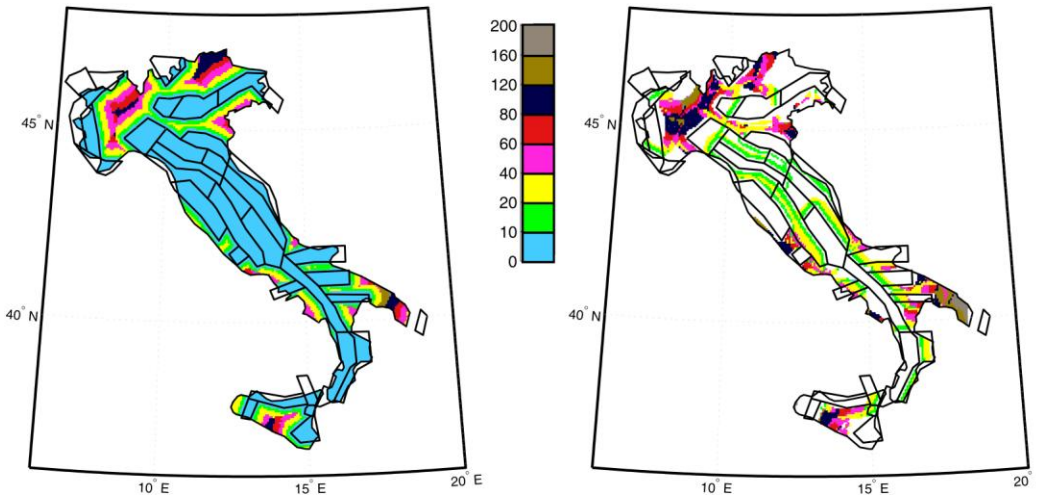

***Figure 2.25**. First (left) and second (right) modal values of distance (in km) for PGA and Tr=2475yrs.*

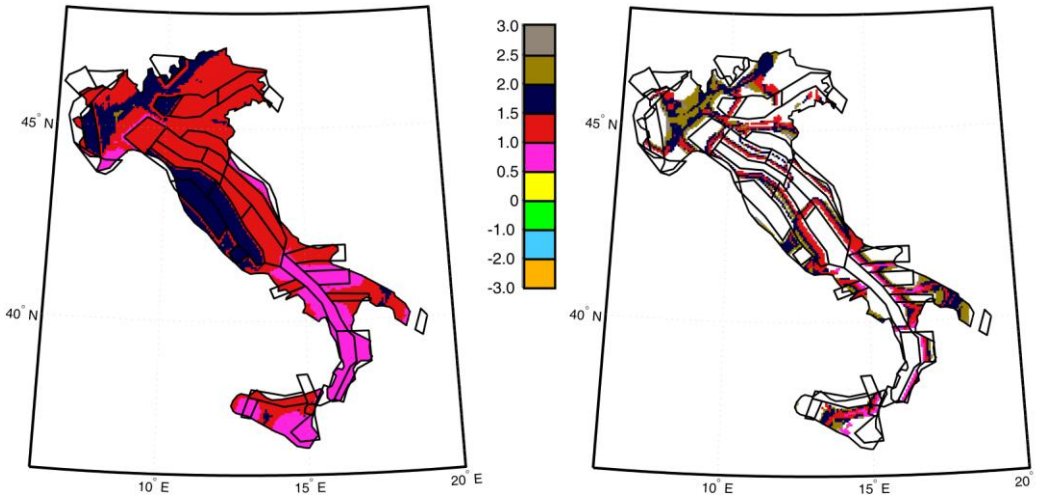

***Figure 2.26**. First (left) and second (right) modal values of ε for PGA and Tr=2475yrs.*

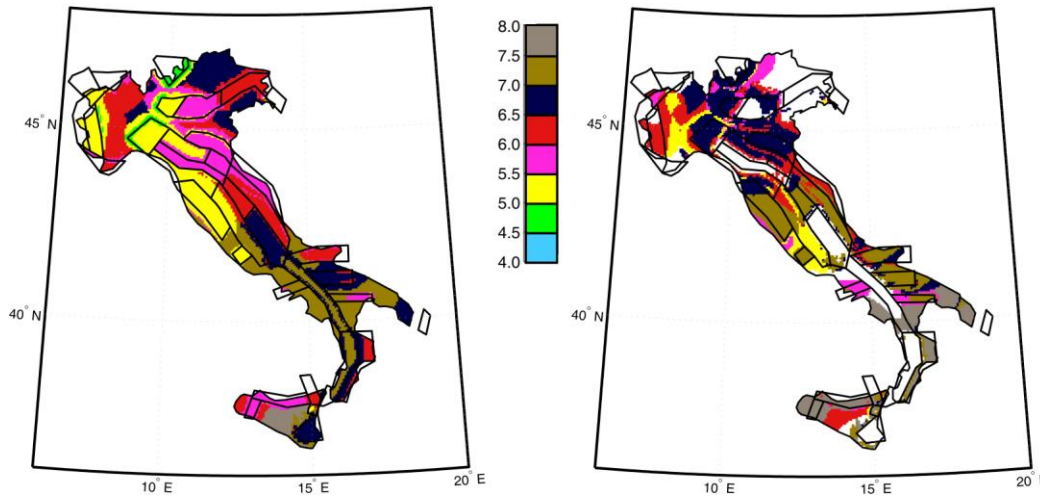

***Figure 2.27**. First (left) and second (right) modal values of magnitude for Sa and Tr=2475yrs.*

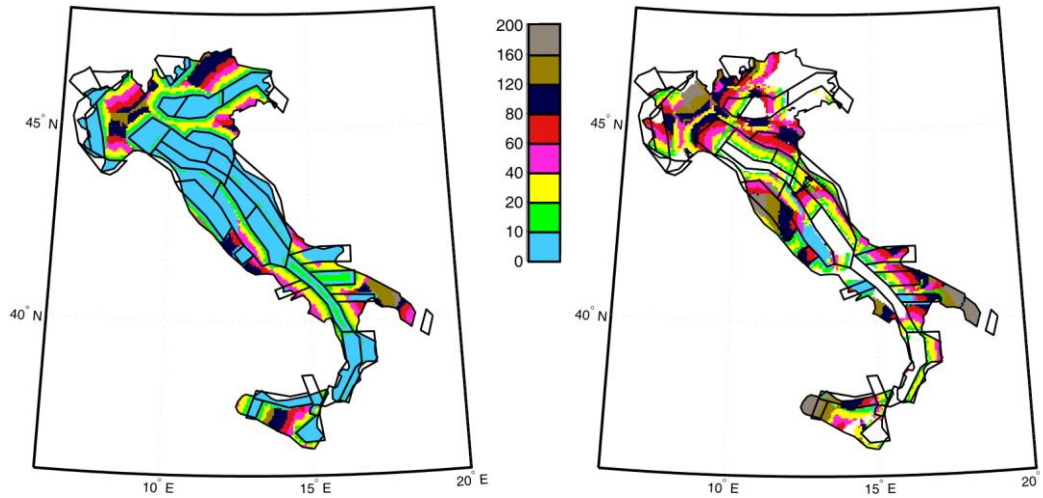

***Figure 2.28**. First (left) and second (right) modal values of distance for Sa and Tr=2475yrs.*

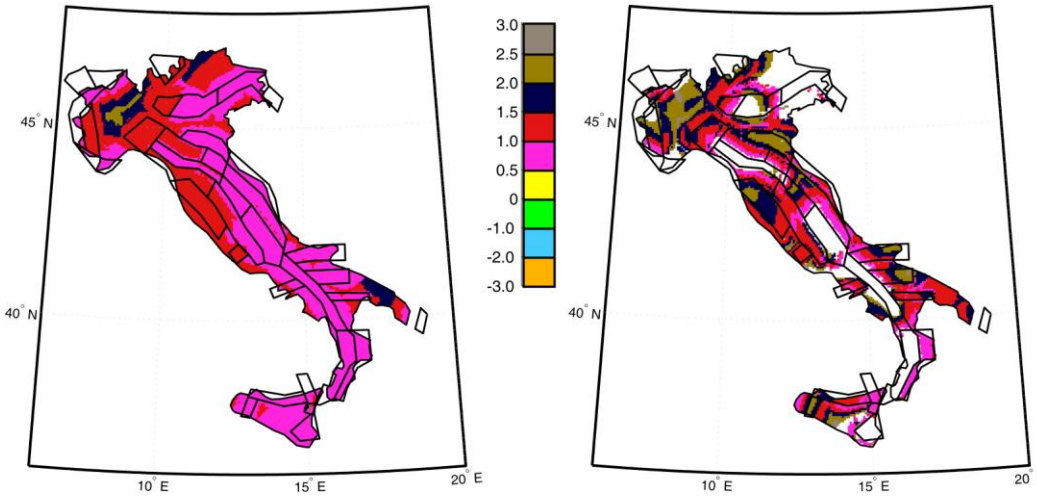

Figure 2.29*. First (left) and second (right) modal values of ε for Sa and Tr=2475yrs.*

2.4.1 Sites with unimodal or bimodal disaggregation PDF

If a site is enclosed or close to a seismic source zone with high seismicity (in term of combination of magnitude interval, annual rate of earthquake and b value of Gutenberg-Richter) comparing to the other surrounding zones, it is easy to understand that the stronger zone dominates the hazard of the site and, as consequence, disaggregation surface will be concentrated in a relatively narrow M and R domain whose limits generally correspond to the minimum and maximum values of magnitude and distance of the zone. Consequently, the effect of the other zones may be minor. For these sites, given the return period and the spectral ordinate of interest, the disaggregation PDF is unimodal and, therefore, characterized by single design earthquake, which however is still a synthetic representation of a distribution which shows some dispersion.

One of these cases is represented by L'Aquila (13.396° E, 42.365° N) whose disaggregation is reported here for a return period equal to 975yrs (Figure 2.30). The site is in fact enclose in the zone 923 characterized by maximum magnitude values of 7.3, annual rate of earthquake occurrence (υ) equal to 0.645 and a *b* value of 0.802. All the other close zones (918, 919, 920) have lower maximum magnitude, lower υ and higher b value; minimum

magnitude is equal for the four considered zones. Each one of the previous number suggest that zone 923 has the higher seismicity so no other considerations are necessary in order to explain the unimodal characteristic of the site shown in Figure 2.30.

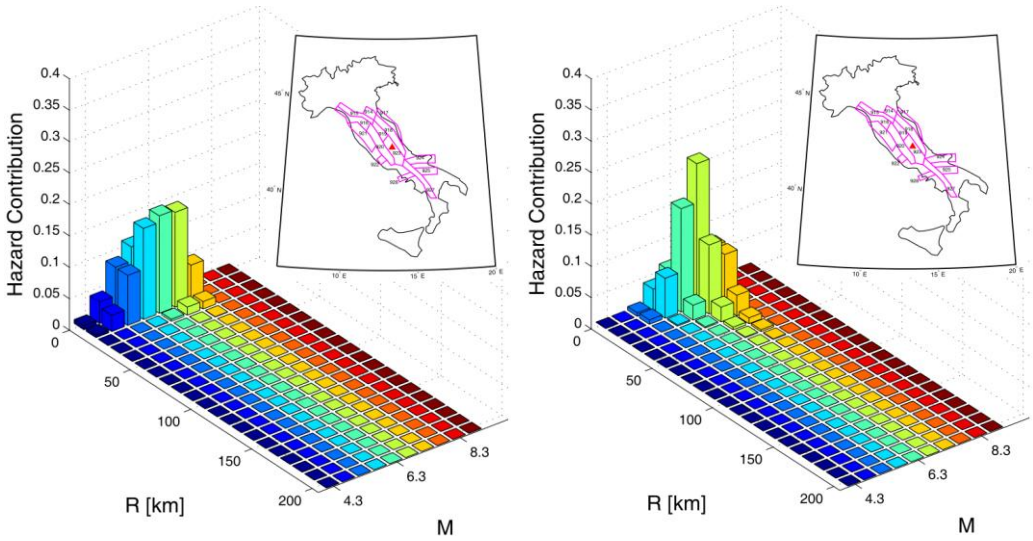

(a) (b)

Figure 2.30. *Disaggregation results for L'Aquila, Tr=975, PGA(a) and Sa(1sec)(b).*

There are many sites in which disaggregation results suggest to identify, at least, two different design earthquakes. An example is the city of Bari (16.879° E, 41.113° N) in the southern. Figure 2.31a shows disaggregation for PGA and Tr=50; disaggregation for Sa and Tr=475yrs is reported in Figure 2.31b. Both disaggregations have two significant modes. It will be discussed in the next section how dominant earthquakes change with the structural period and with return period. At this step it is, however, worth to anticipate that bimodal cases are more easily available for Sa than for PGA; although variation with return period can be completely explained, no equivalent general rules can be formulated. For this particular site, increasing return period, the influence of mode with minor distance decreases.

Disaggregation of PGA provides first and second modal values in terms of R, M and ε equal respectively to {35.5; 5.8; 0.5} and {125.5; 7.3; 1.0} while

first and second mode of Sa disaggregation are {132.5; 7.3; 1.0} and {35.5; 6.7; 0.5}. In the latter case, the first and second modes of joint disaggregation distribution are inverted comparing to what shown by marginal disaggregation of magnitude and distance (reported in the figure).

Closer zones to the site are 924, 925 926 and 927. Zone 925 is the closest one and it determines the first modal value of disaggregations. Zones 924 and 926 have approximately the same distance from the site but zone 924 has higher seismicity having higher maximum magnitude and earthquake annual rate (see Table 2.1). Zone 927 is slightly more distant but its seismic parameters are significantly higher than those associated to all the other zones here considered. In fact, the maximum magnitude is 7.3 (7.0 is the maximum magnitude of zone 924) and υ values is almost twice of the maximum correspondent values of the other zones. The presence of a very strong but distant zone causes the relevant second mode of disaggregation.

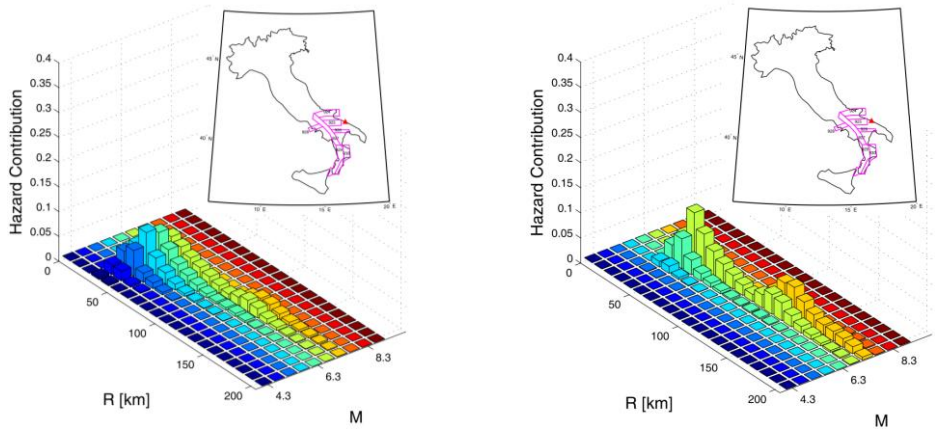

(a) (b)

Figure 2.31. *Disaggregation results of Bari, Tr=50 for PGA (a) and Tr=475 for Sa(1sec) (b).*

It is finally worth to note that there are also a few cases for which disaggregation is trimodal. Chosen example is Ancona (13.506° E, 43.589° N) for which Tr equal to 50yrs is considered (Figure 2.32a). Disaggregation distribution for Sa shows three modal values: the first two modes (recorded by the software) are for R, M and ε are {7.5; 5.0; 0.5} and {33.5; 6.2; 0.5}. Third

mode shown by the Figure 2.32b is for R and M equal to 110 and 6.8 respectively.

The reason because there are three modes is the same explaining why there are two. In fact, for this particular case, zone 917 and 918 determine the first two modes (being the first zone closer and the second with slightly higher seismicity) but a more distant zone (i.e. 923) has a strong seismicity and has non negligible influence on the hazard of the site (third mode).

Because the contribution of the third mode, if any, is expected to be minor, this study is focused on the first two modes.

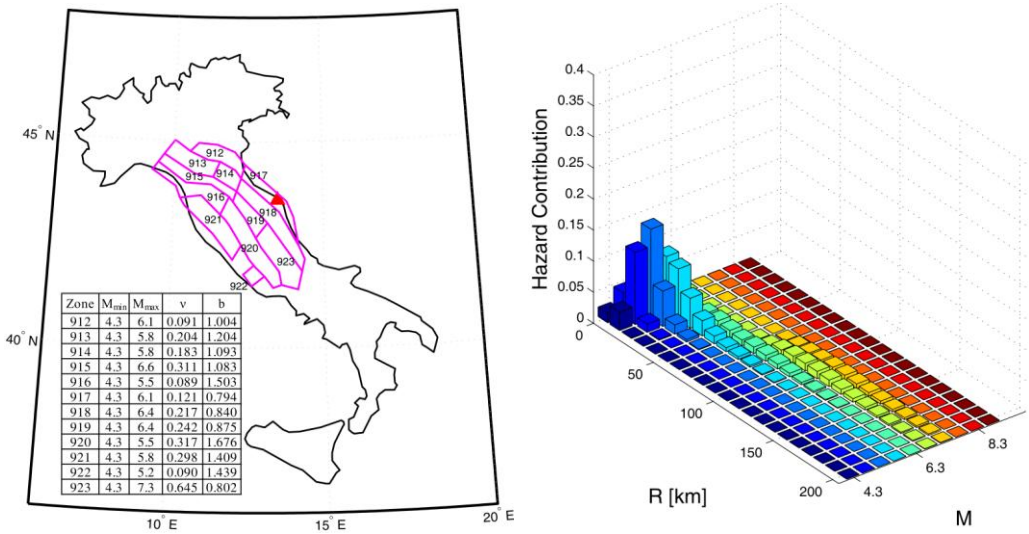

Zone	M_{min}	M_{max}	v	b
912	4.3	6.1	0.091	1.004
913	4.3	5.8	0.204	1.204
914	4.3	5.8	0.183	1.093
915	4.3	6.6	0.311	1.083
916	4.3	5.5	0.089	1.503
917	4.3	6.1	0.121	0.794
918	4.3	6.4	0.217	0.840
919	4.3	6.4	0.242	0.875
920	4.3	5.5	0.317	1.676
921	4.3	5.8	0.298	1.409
922	4.3	5.2	0.090	1.439
923	4.3	7.3	0.645	0.802

(a) (b)

Figure 2.32. Map of Ancona location (a) and disaggregation at Sa for Tr=50 yrs (b).

2.4.2 Influence of Structural Period

Disaggregation results can change significantly changing the considered structural period. This conclusion was anticipated looking at the disaggregation maps and it is also shown for the specific site of Viterbo (12.107° E, 42.426° N) considering a return period equal to 475yrs (Figure 2.33). The example demonstrate that unimodal disaggregation results for PGA may become clearly bimodal for Sa with a new hazard contribution of higher magnitude and

distance design earthquake. As consequence it is apparent that record selection based on information provided by PGA disaggregation can be incomplete for all the structure with non particularly short fundamental period.

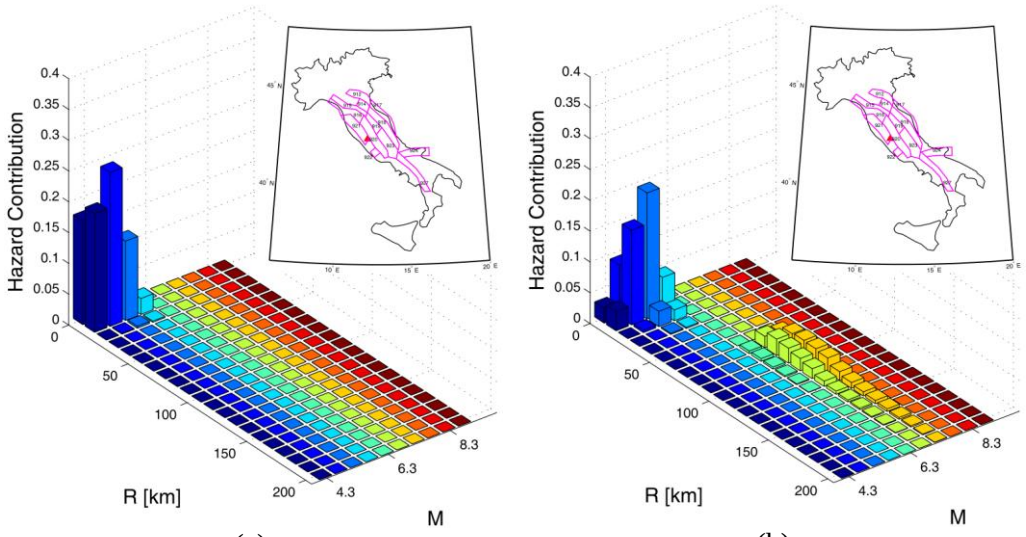

(a) (b)

Figure 2.33. *Disaggregation results for Viterbo, Tr=475, PGA(a) and 1sec(b).*

The reason of changes of disaggregation for different structural period has to be found in the GMPE; in fact, for a fixed site and return period, variation of dominating earthquake for different spectra periods can only depend on the used prediction equation. From seismological knowledge it is expected that seismic waves with higher frequencies are more attenuated with distance so referring to the structural response, spectra ordinates associated to higher period (1.0 sec in this case) are more influenced by distant events than the first spectral ordinate (PGA). In other words, distant zones with negligible influence on PGA hazard, can show non-negligible effects on the Sa hazard at the same site, as also noted in Convertito et al. (2009).

2.4.3 Influence of Return Period

It was found that for those Italian sites for which two modes exist,

increasing the return period of the acceleration being disaggregated, in the most of cases, the hazard contribution of the first mode (close-moderate earthquake) increases with respect to the second mode. One example of such is San Severo (15.377° E, 41.687° N), whose location and seismic parameters of closer zones are reported in Figure 2.34, while disaggregation results for a return period equal to 50 and 2475yr are reported in Figure 2.35. In this case, the influence of return period is not negligible for both PGA and 1 second Sa even if for PGA the effect is minor because, as already explained, more distant zones have lower influence on PGA results. Modal values recorded are reported in Table 2.3.

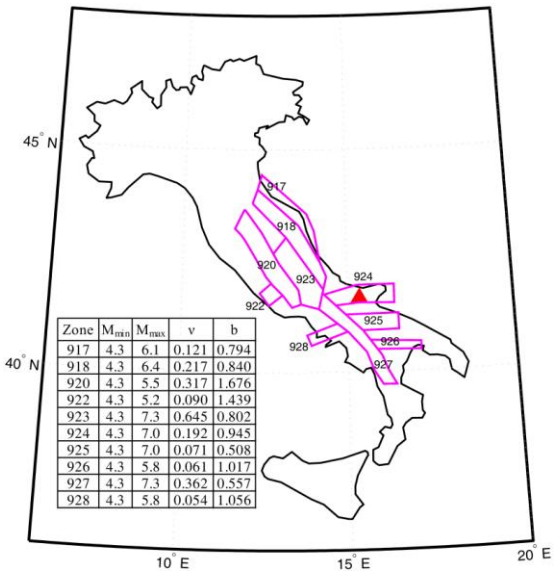

Zone	M_{min}	M_{max}	v	b
917	4.3	6.1	0.121	0.794
918	4.3	6.4	0.217	0.840
920	4.3	5.5	0.317	1.676
922	4.3	5.2	0.090	1.439
923	4.3	7.3	0.645	0.802
924	4.3	7.0	0.192	0.945
925	4.3	7.0	0.071	0.508
926	4.3	5.8	0.061	1.017
927	4.3	7.3	0.362	0.557
928	4.3	5.8	0.054	1.056

Figure 2.34. *Seismogenetic zones closer than 200 km from the site.*

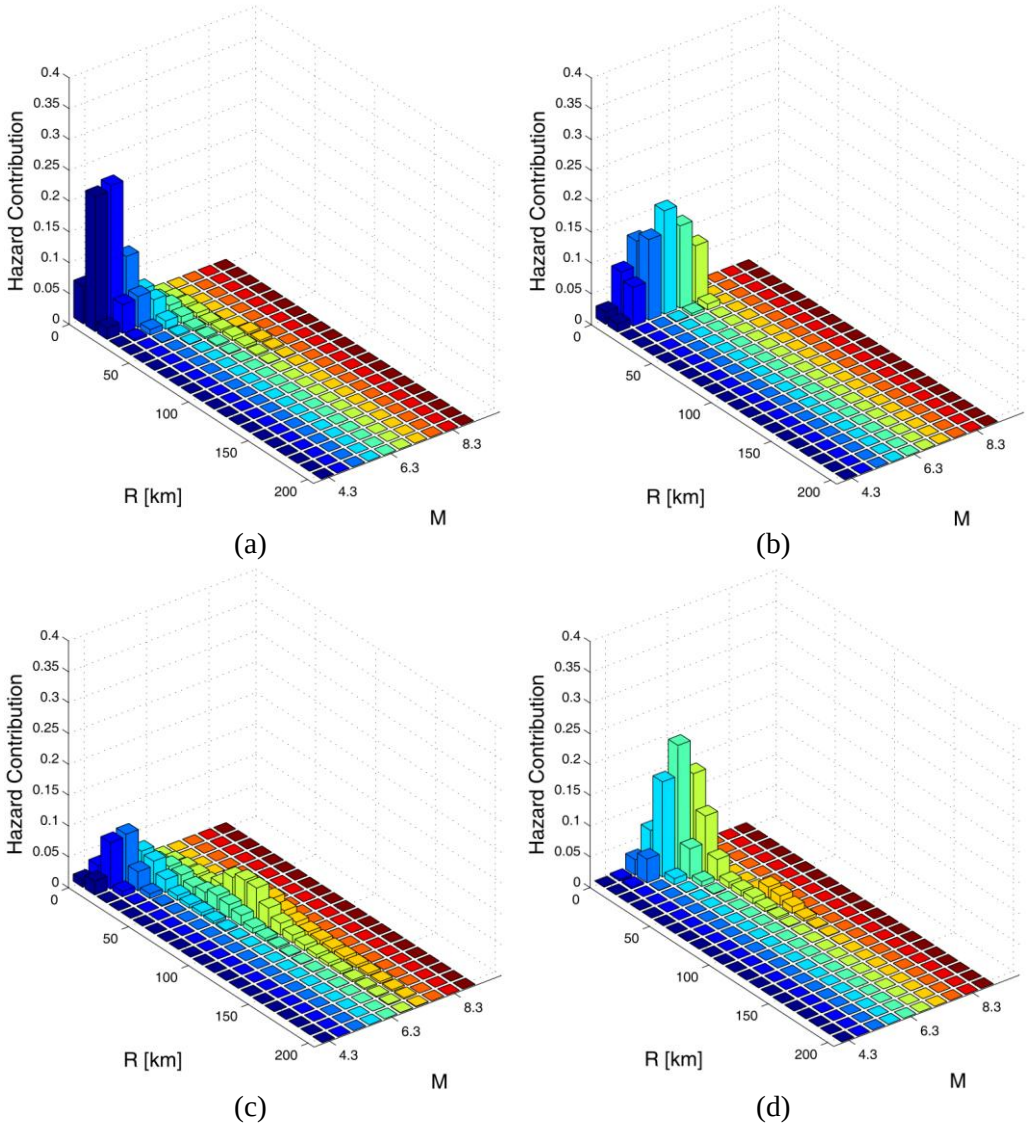

Figure 2.35. *Disaggregation results for San Severo at PGA for Tr=50(a) and 2475(b) and at Sa for Tr50(c) and 2475(d).*

Table 2.3. *Modal values for San Severo.*

			1st mode		2nd mode	
	Longitude [°]	Latitude [°]	R [km]	M	R [km]	M
PGA 50 yrs	15.37	41.67	8.50	4.33	58.50	6.98
PGA 2475yrs	15.37	41.67	5.50	5.43	-	-
Sa(1.0sec) 50 yrs	15.37	41.67	6.50	4.88	82.50	6.98
Sa(1.0sec) 2475 yrs	15.37	41.67	6.50	6.08	63.50	7.28

In order to analyze the influence of Tr on disaggregation results, it is useful to consider an ideal example of one site influenced by two seismogenic zones identified as Z_1 and Z_2. Starting from equation (1) and applying Bayes theorem, hazard contribution (HC) of all the magnitude and distance values due to Z_1 and Z_2 are reported in Eqs. 3 and 4 respectively:

$$HC_{z_1} = f\left(m,r\middle|IM > IM_0\right)\Big|_{Z_1} = \frac{f\left(IM > IM_0\middle|m,r\right)\Big|_{Z_1} \cdot f\left(m,r\right)\Big|_{Z_1}}{f\left(IM > IM_0\right)} \tag{3}$$

$$HC_{z_2} = f\left(m,r\middle|IM > IM_0\right)\Big|_{Z_2} = \frac{f\left(IM > IM_0\middle|m,r\right)\Big|_{Z_2} \cdot f\left(m,r\right)\Big|_{Z_2}}{f\left(IM > IM_0\right)} \tag{4}$$

$f\left(IM > IM_0\right)$ is a marginal probability (from the Bayes theorem) and it doesn't depend on the considered zone; $f\left(m,r\right)\Big|_Z$ and $f\left(IM > IM_0\middle|m,r\right)\Big|_Z$ depend on the two zones and they are usually called prior and posterior distributions. Prior probability is the joint distribution of magnitude and distance due to a specific zone so it is a function of relative site-zone position and of seismic parameters of the zone (υ, b, M_{max} and M_{min}). Posterior probability is obtained by the GMPE computed for each given values of M and R. Comparison of hazard contribution of the zones can be studied looking at the ratio $HC_{z_1} \Big/ HC_{z_2}$, Eq. 5.

$$HC_{z_1} \Big/ HC_{z_2} = \frac{f\left(IM > IM_0 | m,r\right)_{Z_1}}{f\left(IM > IM_0 | m,r\right)_{Z_2}} \cdot \frac{\left[f\left(m,r\right)\right]_{Z_1}}{\left[f\left(m,r\right)\right]_{Z_2}} \tag{5}$$

For a given return period, the zone with the higher product of prior and posterior probability has the higher hazard contribution. Increasing return period, ratio between prior probabilities doesn't change in fact source to site distance and magnitude distribution are not dependent on Tr. Conversely, IM_0 increases and posterior probability ratio determines all the variations of disaggregation results with Tr.

A numerical example is proposed below in order to analyze how posterior probability ratio can change changing IM_0. The easiest hypothesis of only one possible earthquake magnitude for each zone is assumed. In particular M equal to 5 and 6.5 is used for zone Z1 and Z2 respectively. Moreover average epicentral distances associated to Z_1 and Z_2 are 5 and 135 km. The simple scheme of site and zones considered is sketched in Figures 2.37. Using the average distances in the place of the whole distance distributions, variation of posterior probabilities ratio can be easily analyzed. In Figure 2.36a average intensity measure (in logarithmic scale) computed by Ambraseys et al. (1996) attenuation relationship are reported for the considered characteristic magnitudes. In particular spectral acceleration for period equal to 1.0 second is considered. For each value of distance, GMPE provide a normal distribution of log(Sa) with a constant standard deviation. Lognormal distributions are reported in the plot for the selected average distances. Performed PSHA has provided the values of Sa for Tr equal to 50 and 2475 yr and these values are indentified in the figure by the black and red horizontal lines. Posterior probability ratio is the ratio of the complementary cumulative lognormal distribution functions (CCDF) computed for the Sa obtained by PSHA. For the considered case, the trend of the ratio is a positive slope as reported in Figure 2.36b. As consequence, it is possible to anticipate that increasing Tr, the hazard contribution of Z_1 increases respect to the Z_2. The result is confirmed by disaggregation results for Tr=50 and 2475yr reported in Figure 2.37a and

2.37b where it is shown that the site can be considered as bimodal for Tr=50 and unimodal for Tr=2475yr.

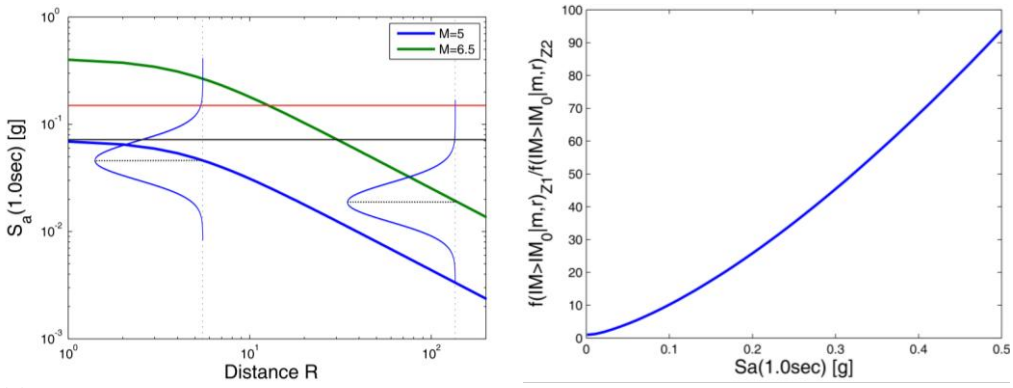

(a) (b)

Figure 2.36. *Sa(T=1.0sec) predicted by Ambraseys et al. GMPE for fixed magnitude values (a) and ratio of CCDFs referred to Z1 and Z2.*

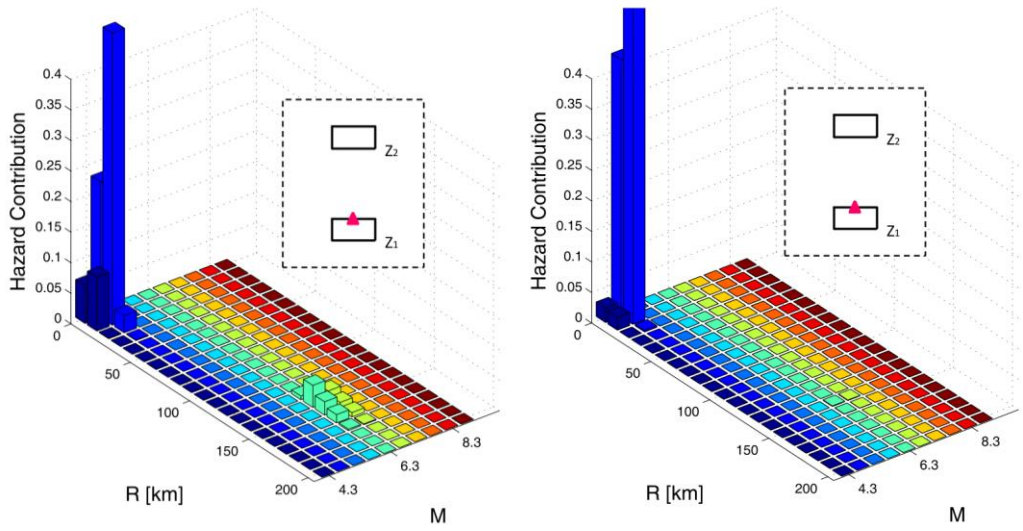

(a) (b)

Figure 2.37. *Disaggregation results for Sa referring to Tr=50yrs(a) and 2475 yrs (b).*

Starting from the proposed example, it is important to underline that earthquake occurrence rates of the zones have influence on the determination of the hazard values. Because ordinary PSHA is referred to the IM exceedance

probability, usually identified hazard level correspond to a positive ε value of IM distribution computed by GMPE. Moreover if the zone with higher average Sa (Z_1 in this case) has also an higher υ rate, the influence of the second zone is practically negligible also for low Tr (so disaggregation results don't change significantly with Tr). In the presented case, in order to show different results for different Tr, υ rate associated to Z_1 is lower than the rate associated to Z_2 (0.08 and0.65 respectively).

A possible alternative condition can be verified when magnitudes and distances associated to the closer zone provide average IM lower than the more distant zone. This situation is conceptually not so different from the previous one, but it has opposite consequences for increasing Tr. In fact the hazard contribution that becomes negligible for higher Tr is that of the closer zone and the second scenario results of increasing importance. As an example, the case of Frosinone (13.336° E, 41.639° N) is reported in Figure 2.38 along with location and affecting seismic zones. Disaggregation results are reported in Figure 2.39a and 2.39b where it is shown that increasing return period, hazard influence of the closest zone decreases.

The site is also interesting for the significance of modal values. In fact for Tr=50yr, first and second modal values for Sa are {5.5; 4.48; 1.0} and {75.70; 6.88; 0.50}. These values are in good accordance with the plot in Figure 2.39a. Same results for Tr=2475yr are {34.50; 7.28; 0.5} and {24.50, 6.98, 0.50}. In this case, second mode is different from the value suggested by the plot (i.e. 10; 5.3) and it can be inferred that, the original four dimensional surface (before the numerical integration over all the ε values) has a second mode close to the first one that is hidden by the integration and by the bins representation. In cases like this, the real third mode is not negligible and the chosen synthetic representation of disaggregation results is not completely informative. Some other examples of site disaggregation analyses will be shown below in order to underline peculiar results and possible limits of modal values' significance.

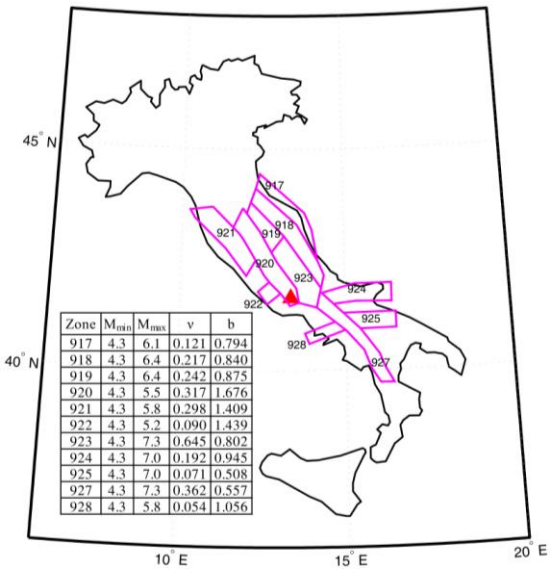

Zone	M_{min}	M_{max}	v	b
917	4.3	6.1	0.121	0.794
918	4.3	6.4	0.217	0.840
919	4.3	6.4	0.242	0.875
920	4.3	5.5	0.317	1.676
921	4.3	5.8	0.298	1.409
922	4.3	5.2	0.090	1.439
923	4.3	7.3	0.645	0.802
924	4.3	7.0	0.192	0.945
925	4.3	7.0	0.071	0.508
927	4.3	7.3	0.362	0.557
928	4.3	5.8	0.054	1.056

Figure 2.38. *Map of Frosinone location.*

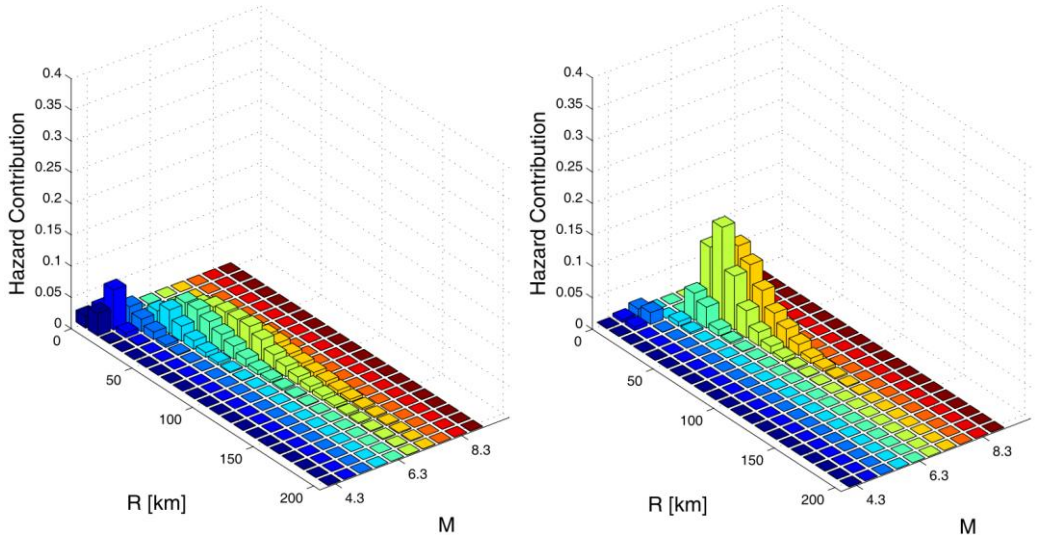

Figure 2.39. *Disaggregation results for Frosinone at Sa for Tr=50(a) and 2475yr (b).*

2.4.4 How representative are maps of modes with respect to disaggregation distributions?

As mentioned the identification of first and second modal values allows to provide the synthetic and more rational representation of the whole disaggregation distribution but significance of these parameters can be criticized if intervals of distance and magnitude with relevant hazard contribution are particularly large. A example is the site of Campobasso (14.668° E, 41.561° N) considered here for Sa and Tr equal to 50 yrs. Geographical position and seismic parameters of closer zones are reported in Figure 2.40a while disaggregation distribution is shown in Figure 2.40b. First and second modal values are respectively {6.5; 4.93, 0.5} and {13.5; 5.53, 0.5} in terms of distance, magnitude and ε and the distribution does not seem to have a third significant mode. Despite that, it is clear that also high distance and magnitude values have an non-negligible hazard contribution because dispersion of distribution is very high.

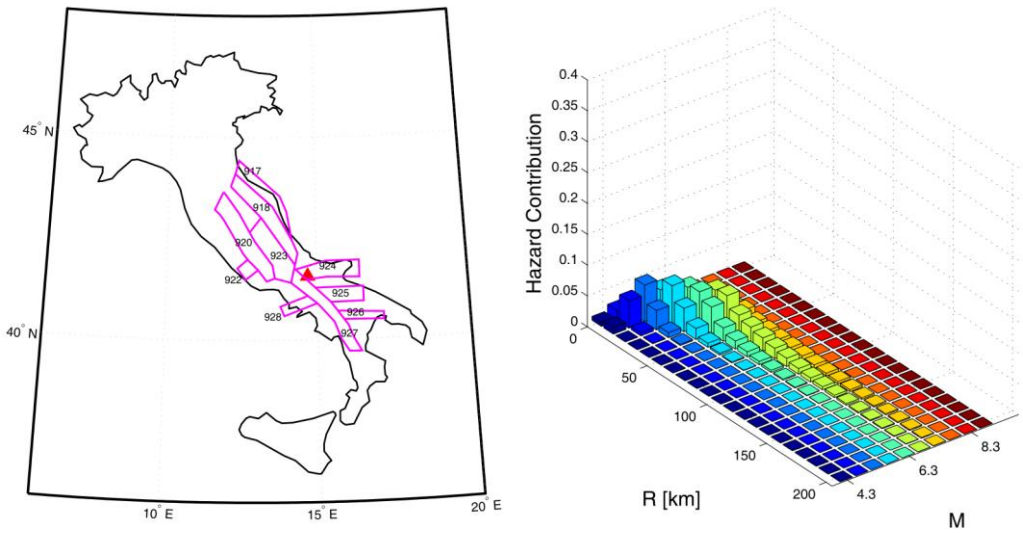

(a) (b)

Figure 2.40. *Map of Campobasso location (a) and disaggregation at Sa for Tr=50 yrs (b).*

2.4.5 Limit of second mode hazard contribution

In Section 2.4, limit value for the minimum second mode contribution (10-4) has been chosen looking at disaggregation for several sites, yet it is still arbitrary and PDFs can have different shapes in a way that an unique assumption may not satisfy all the cases. For example, for the site near Caltanissetta (14.18° E, 37.33° N) whose disaggregation of PGA for Tr=50 yrs is reported in Figure 2.41a, the choice seems to be reasonable because several M and R bins give low but non-negligible contribution to hazard in a way that globally the second mode is really significant. First and second mode for this case are identified for distance, magnitude and ε equal to {54.5; 6.1; 1.0} and {144.5, 7.6; 1.0} and associated probability is 0.0056 and 0.00057 respectively.

In the second case (Figure 2.41b), the site considered is Naples (14.191° E, 40.829° N) for PGA and Tr=475 yrs. The second mode {50.5; 7.3; 1.5} has an hazard contribution equal to 0.00028 but it is contribution seems to be negligible because no other close bins have comparable associated probability.

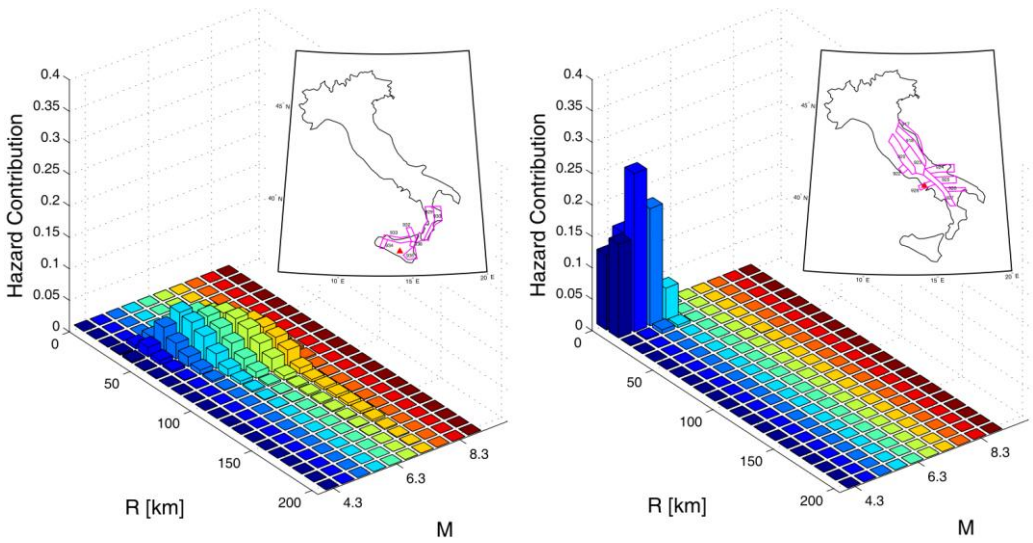

(a) (b)

Figure 2.41. *Limit cases of relevant (a) and negligible (b) second mode hazard contribution.*

2.4.6 Influence of hazard discretization

Showing hazard results, the influence of IM discretization was discussed and a particular site was analyzed (Pavia, 9.16° E, 45.185° N). Results have shown that with an increased IM discretization, computed hazard values are in good accordance with hazard INGV data. Comparison with INGV data has to be shown also for disaggregation results and, as consequence, it has to be referred to the PGA (disaggregation of Sa is not provided by INGV). In Figure 2.42 PGA disaggregation of Pavia are reported for the four computed return periods and using the original and the more discretized IM values. In Figure 2.43, equivalent disaggregation distributions obtained from INGV data are reported.

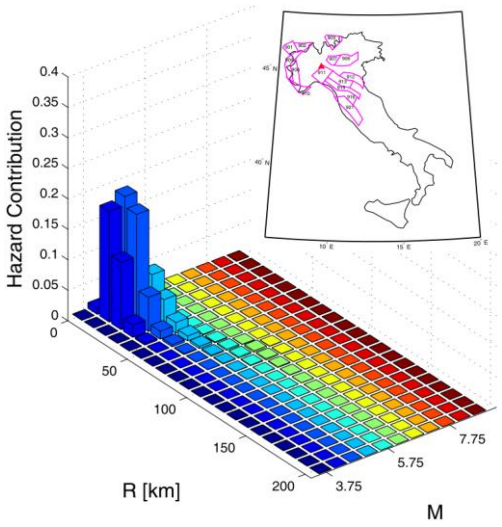

(a)

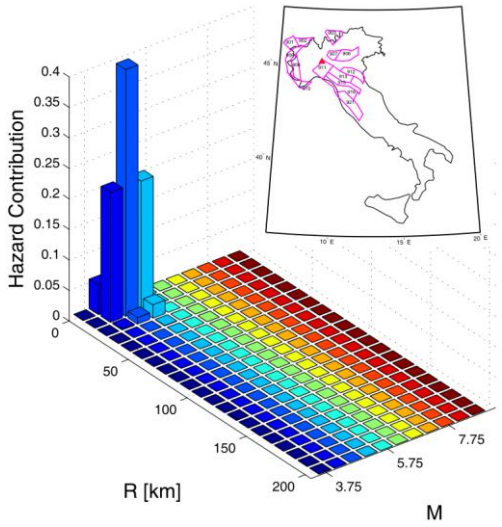

(b)

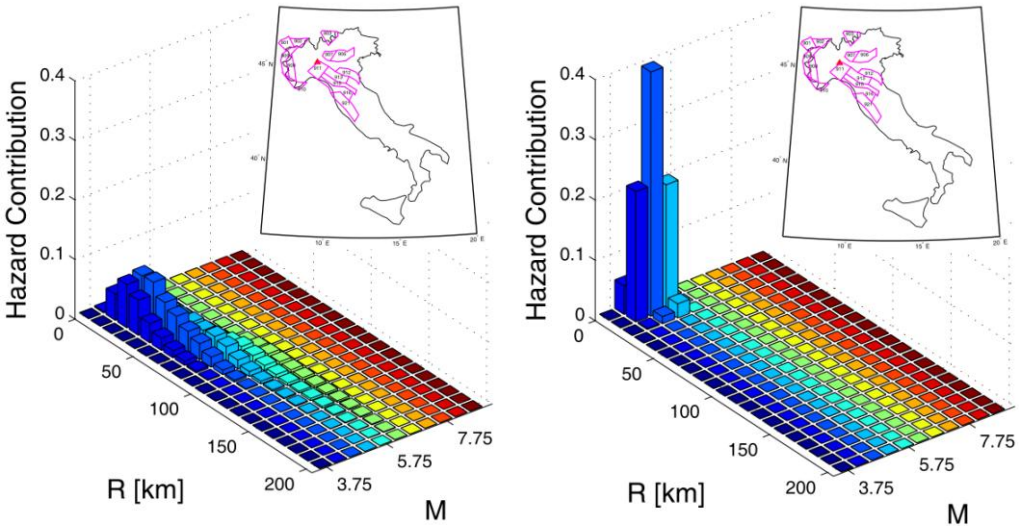

(c) (d)

Figure 2.42. *Disaggregation of PGA for Pavia: original discretization and referring to Tr 50 (a) and Tr=2475 (b): modified discretization and referring to Tr=50 (c) and Tr2475 (d).*

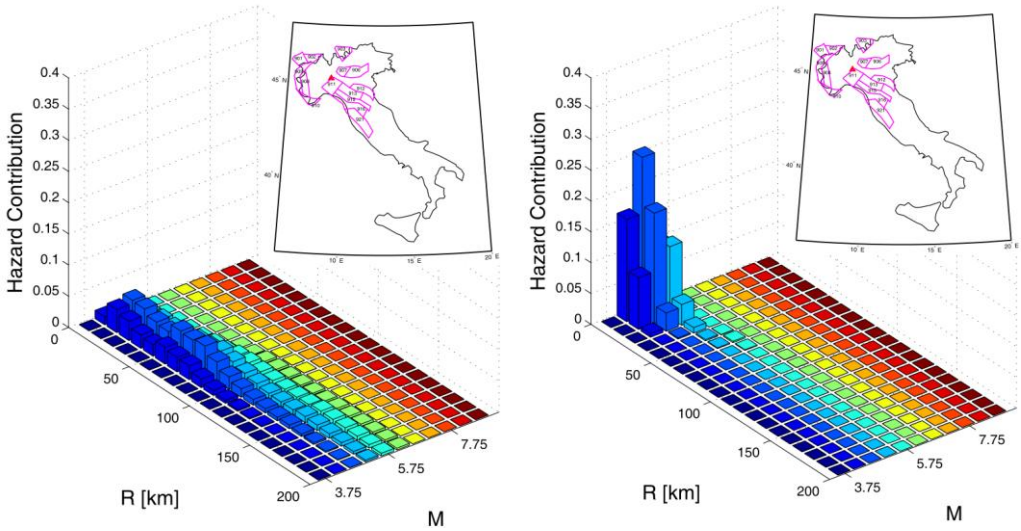

(a) (b)

Figure 2.43. *Disaggregation from INGV data for Pavia: PGA for Tr=50(a) and Tr=2475(b).*

Hazard curves are convex in the probability range of structural interest

and approximation of a convex curve by a limited number of point provides values higher than or at least equal to the real ones. So, even for the original discretization of IM (not sufficient for sites with the lowest seismicity) disaggregation for the highest return period are in good accordance with INGV. More sensible is the analysis of lower return periods and for this site, approximation of original results is not acceptable. As consequence it is extremely important to show another comparison between INGV and computed disaggregation. The site of Enna is chosen because is considered particularly interesting for the irregularity of disaggregation surface. In Figure 2.44 computed disaggregations are compared with INGV ones, for Tr equal to 50, 475, 975 and 2475 yrs.

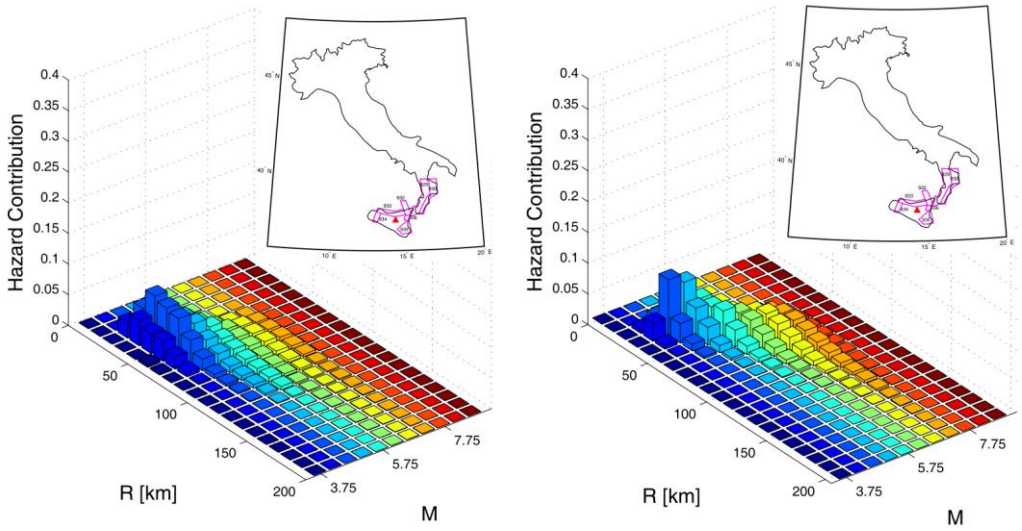

(a) (b)

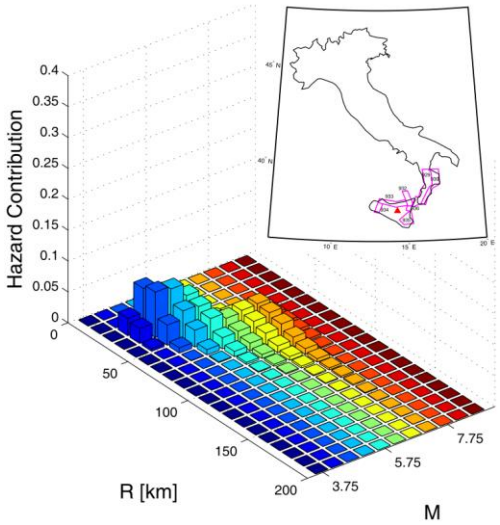
Hazard Contribution
0.4
0.35
0.3
0.25
0.2
0.15
0.1
0.05
0
0
50
100
150
200
R [km]
3.75
5.75
7.75
M

(c)

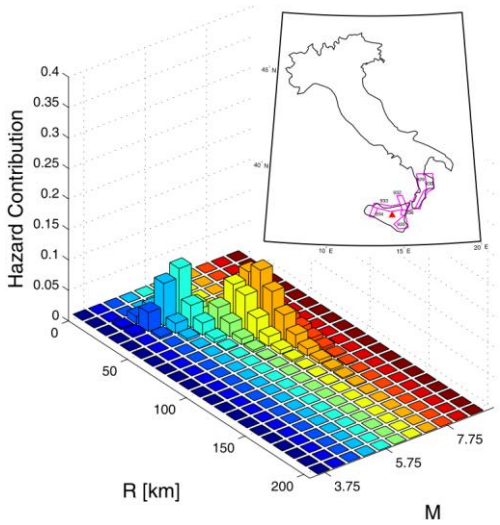
Hazard Contribution
0.4
0.35
0.3
0.25
0.2
0.15
0.1
0.05
0
0
50
100
150
200
R [km]
3.75
5.75
7.75
M

(d)

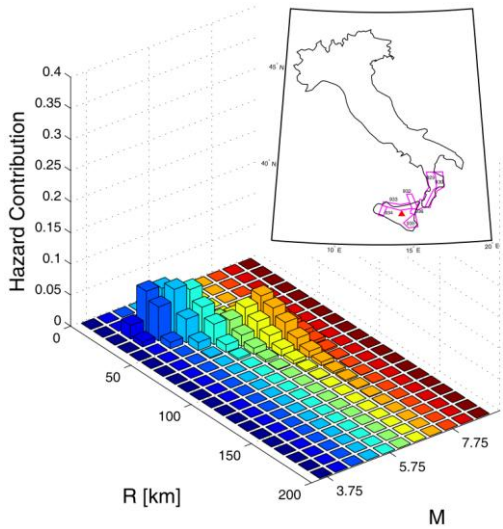
Hazard Contribution
0.4
0.35
0.3
0.25
0.2
0.15
0.1
0.05
0
0
50
100
150
200
R [km]
3.75
5.75
7.75
M

(e)

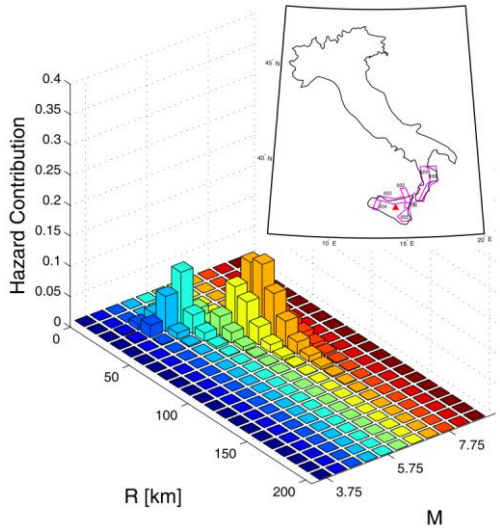
Hazard Contribution
0.4
0.35
0.3
0.25
0.2
0.15
0.1
0.05
0
0
50
100
150
200
R [km]
3.75
5.75
7.75
M

(f)

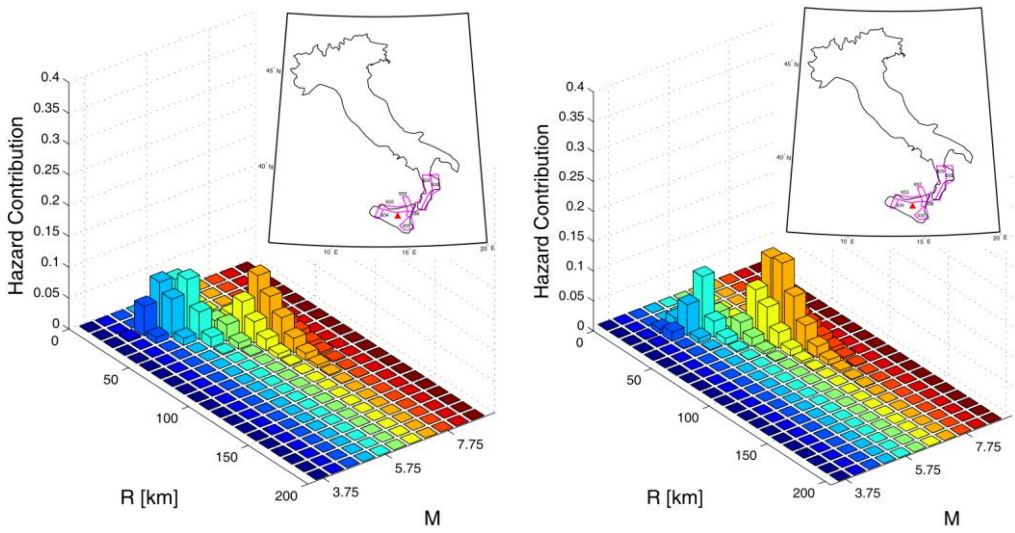

(g) (h)

Figure 2.44. *Disaggregation results for Enna at PGA: INGV data for Tr=50(a), Tr=475(c), Tr=975(e) and 2475(g); computed in this study for Tr=50(b), Tr=475(d), Tr=975(f) and 2475(h).*

Good accordance with INGV data has been found for many checked sites with medium-high seismicity. As general rule, authors have identified a conditions on hazard results to verify if disaggregation can be considered reliable. More specifically, for a given return period, if the difference between IM values obtained by PSHA and the corresponding value for the immediately higher Tr is lower 0.001g, the analyses in the site is assumed to be not enough detailed and disaggregation results are rejected for the considered return period.

2.4.7 Disaggregation for different structural periods

Disaggregation has been performed for structural period equal to one second in order to account for medium-long period of ordinary engineering structures. In this section disaggegation for different structural periods will be shown to provide more information about the range of periods in which results for 1.0 sec can be considered significant. The analyzed site is Viterbo (already presented as example of bimodal distribution) and considered structural

periods are 0.5 and 2.0 sec.

In Figure 2.45 and 2.46 results for Tr=50 and Tr=2475 are reported: in each case, a total of 4 structural period are studied (i.e. 0sec or PGA, 0.5sec, 1.0sec and 2.0sec).

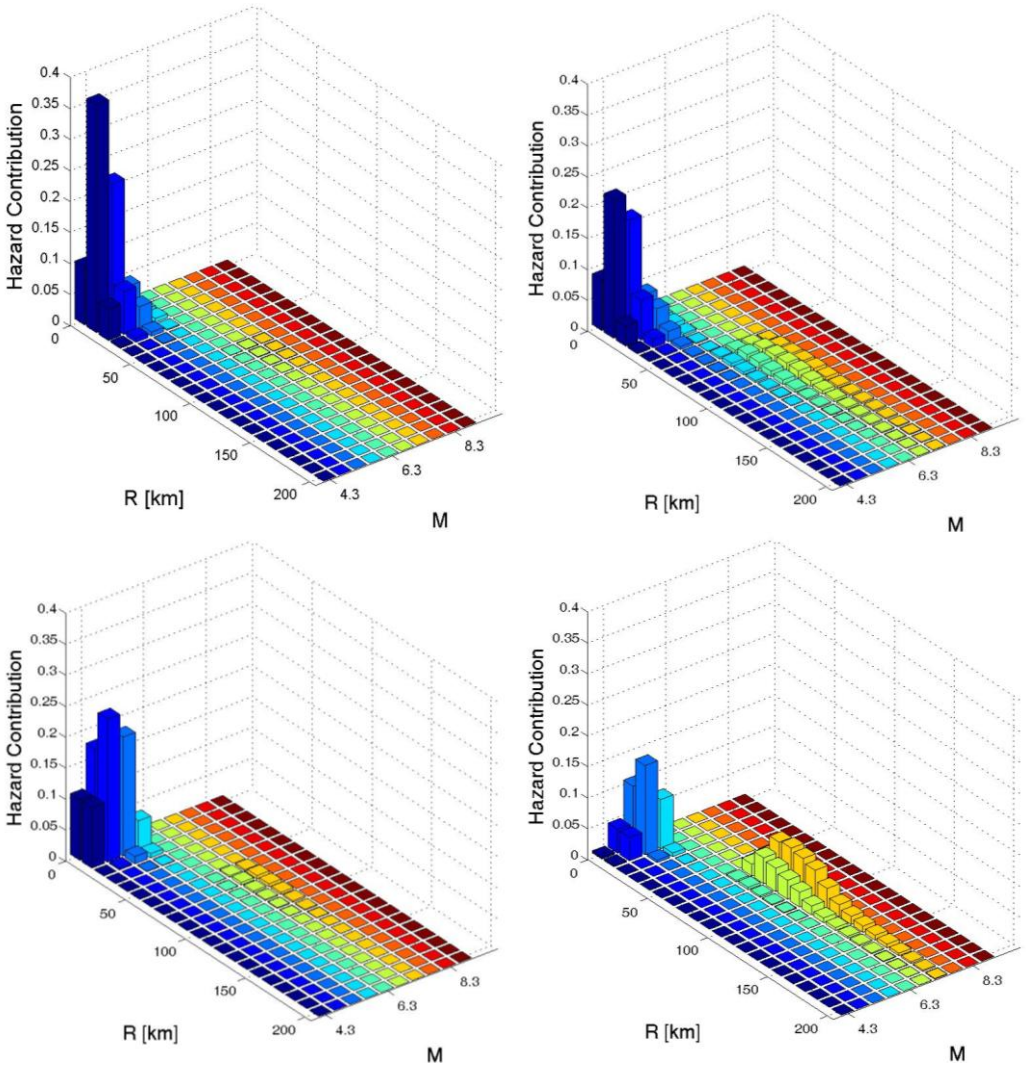

Figure 2.45. *Disaggregation for Viterbo and Tr=50yrs: PGA(a), T=0.5sec(b), T=1.0sec(c) and T=2.0sec(d).*

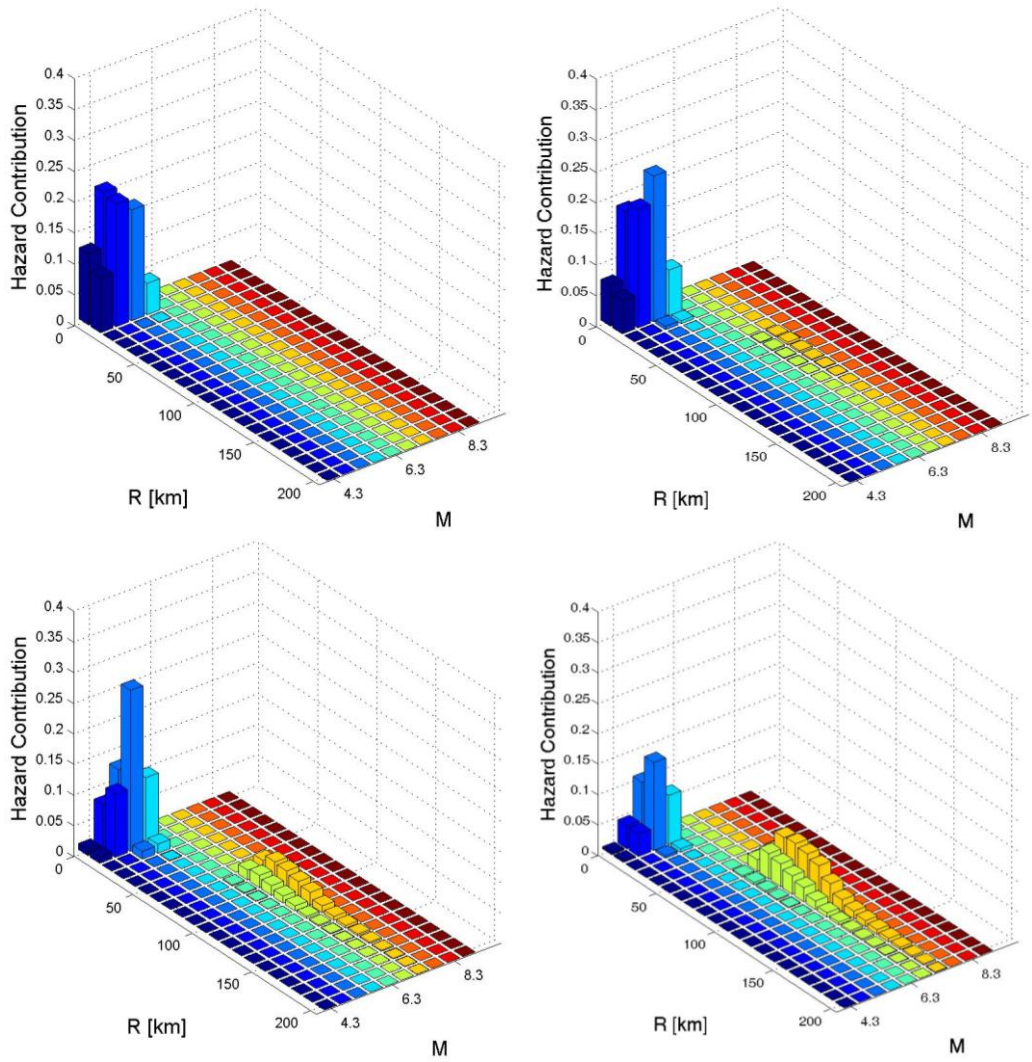

Figure 2.46. *Disaggregation for Viterbo and Tr=2475yrs: PGA(a), T=0.5sec(b), T=1.0sec(c) and T=2.0sec(d).*

Increasing influence of distant zones with higher structural periods is a trend confirmed also by 2.0 sec results. Moreover, looking at Tr=50, it appears clear that results for T=0.5 and 2.0sec are better represented by disaggregation for T=1.0sec than by the case of PGA. Although less evident for Tr=2475, the same conclusion can be accepted because a low hazard contribution of the second mode (evident for T=1.0sec) is visible also for T=0.5sec. In particular

the modal value associated to that range of magnitude and distance is {67.5; 7.28} and has a probability equal to 0.0012 that is higher than the minimum limit introduced conventionally before (0.0001). Suggested conclusion is that disaggregation of PGA has to be used if the considered structures have a fundamental period lower than 0.5 sec. In all other cases, disaggregation for Sa=1.0sec seems to be the most rational choice.

2.5 Application of disaggregation's results: REXEL 3.1 (beta) and Conditional hazard maps

REXEL is a computer software freely distributed over the internet (www.reluis.it), which allows to search for suites of waveforms, currently from the European strong motion database and the ITalian ACcelerometric Archive (ITACA), compatible on average to various types of spectral shapes (Iervolino et al., 2010a). These sets are always compatible to the reference (i.e., target) spectra complying with code provisions, but the new released version of the software (V 3.1) reflect also some research-based criteria considered relevant for seismic structural assessment: in fact users can select the records corresponding to a given range of magnitude and distance, peak ground acceleration (PGA), peak ground velocity (PGV), Cosenza and Manfredi index (I_D) (Manfredi, 2001) or Arias Intensity (I_A).

Utilized software for disaggregation has been implemented in REXEL (which is now able to suggest to the user the better design earthquakes (in term of magnitude and distance) to use as additional criteria for record selection. Structural and return periods of disaggregation implemented in REXEL are the same presented in this paper. So choosing a site and a return period (function of characteristics of the considered structure i.e. *Nominal life*, *Structural type* and *Limit state*), the software provided tridimensional (ε values are not reported) disaggregation distribution for one of the four return period closest to the selected one and for PGA or Sa(T=1.0sec). In Figure 2.47 the software GUI is shown. Implementation should allow for improving record input

selection for earthquake engineering applications in a hazard consistent manner yet easily viable for practitioners.

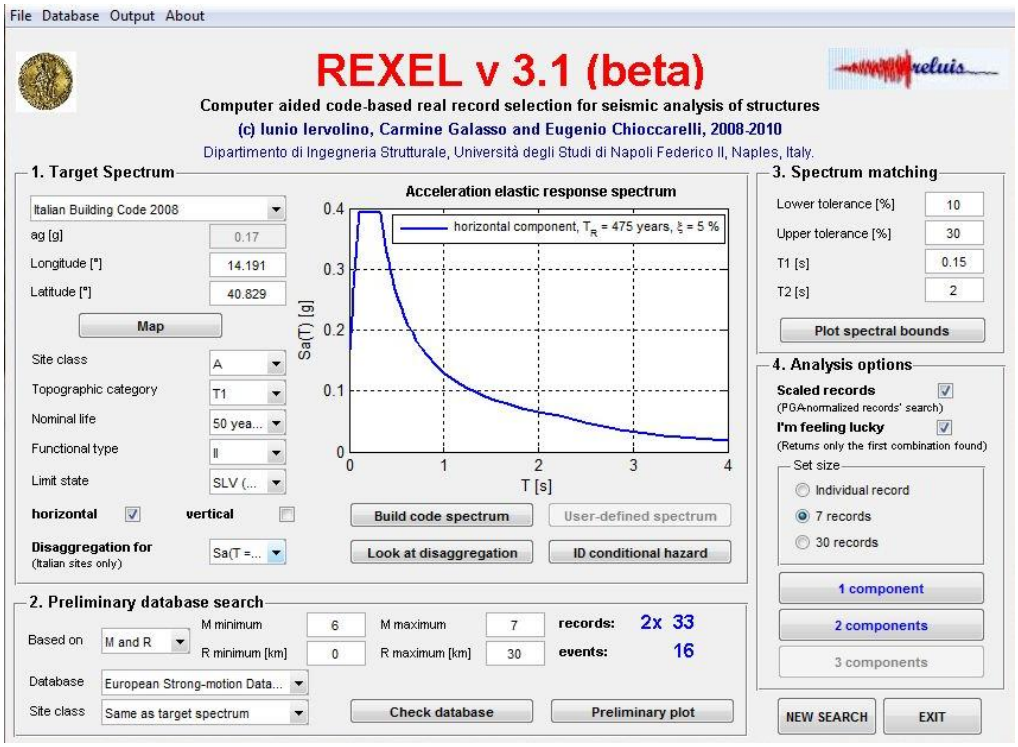

Figure 2.47. *Image of software GUI*

More sophisticated IMs are currently under investigation by many researchers. For example, Baker (2007) discusses vector-valued IMs' potential in terms of efficiency in estimating structural response. Most of the proposed vector-valued IMs are comprised of spectral ordinates or other proxies for the spectral shape in a range of periods believed to be of interest for the nonlinear structural behaviour. This helps to estimate the peak seismic demand especially in terms of displacements.

Integral signal's parameters, as the Arias intensity or significant ground motion duration, are possible IMs, but they are considered related more to the cyclic energy dissipation rather than to the peak structural response. In fact, some studies (e.g., Iervolino et al., 2006) investigated how ground motion

duration-related parameters affect nonlinear structural response. It was found that, generally, spectral ordinates are sufficient (i.e., duration does not add much information) if one is interested in the ductility demand, while duration-related measures do play a role only if the hysteretic structural response is that to assess; i.e., in those cases in which the cumulative damage potential of the earthquake is of concern. However, in general, the integral ground motion parameters associated to duration are less important with respect to peak IMs, as damages to structures, in general, are more due to displacements, and therefore the former IMs may be considered secondary with respect to the latter. In these cases, it seems appropriate to develop *conditional hazard maps*; i.e., maps of percentiles of the secondary IM given the occurrence or exceedance of the primary parameter for which a design hazard map is often already available by national authorities. In Iervolino et al. (2010b) a first application of conditional hazard maps is provided choosing PGA as primary IM and Cosenza and Manfredi index (I_D) as secondary being a cyclic response-related measured which may account for the cumulative damage. Analytically I_D is the ratio of the integral of acceleration squared to the PGA and (PGV) (Equation 6).

$$I_D = \frac{\int_0^{t_E} a^2(t)dt}{PGA \cdot PGV} = \frac{I_A}{PGA \cdot PGV} \tag{6}$$

In the paper an attenuation relation for the logs of ID as a function of M, R and local site conditions is computed starting from Sabetta and Puglise (1996) GMPE. Analytical expression is reported in Eq. 7:

$$\log_{10} I_D = a + bM + \log_{10}\left(\frac{\left(R^2 + h_1^2\right)^{c_1}\left(R^2 + h_2^2\right)^{c_2}}{\left(R^2 + h_3^2\right)^{c_3}}\right)^{\frac{1}{2}} + dS_1 + eS_2 + \varepsilon_{\log_{10} I_D} \tag{7}$$

An illustrative example of I_D conditional hazard maps was presented for

Campania region but using first modal values of PGA disaggregation discussed in this work, application can be easily extended to all the Italian sites. An example is reported in Figure 2.48 in which referring to Tr=50 yrs two percentiles of I_D conditional PDF distribution are shown: 50% in Figure 2.48a and 90% in Figure 2.48(b).

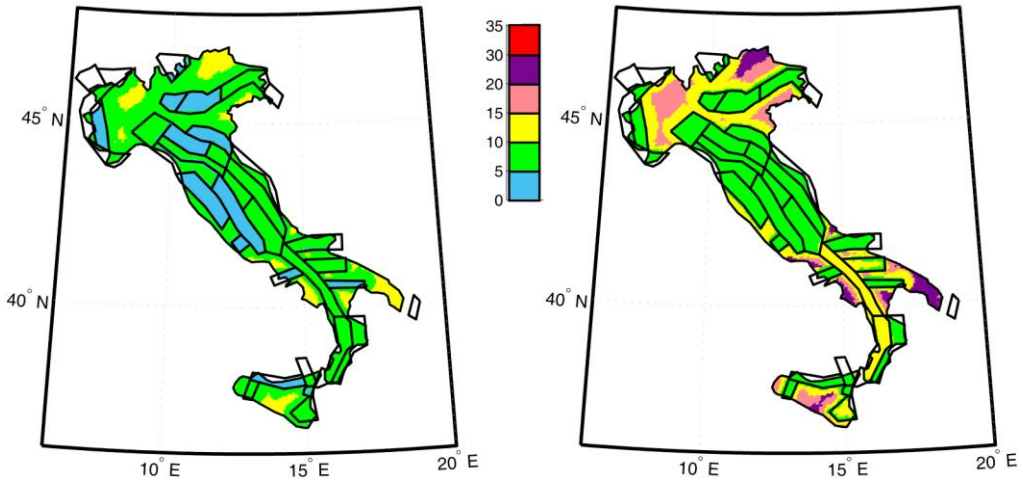

(a) (b)

Figure 2.48. *Conditional hazard maps of I_D for Tr=475yr referring to50th(a) and 90th(b) percentiles*

As mentioned, definition of a range of I_D is one of the additional criteria to address record selection done by REXEL (Galasso et al., 2010).

2.6 Conclusions

Referring for the modeling of seismogenic zones of Meletti et al. (2008), also adopted by INGV and using seismic parameters of each zone provided by Barani et al. (2009), disaggregation analysis was applied to all Italian sites via a Fortran program specifically developed and also used in Convertito et al. (2009). Two different spectral periods equal to 0 (PGA) and 1.0 sec and four different return periods (50, 475, 975 and 2475 yrs) were considered. Maps of

first and second modal values of distance, magnitude and ε are shown as synthetic representation of results but also complete disaggregation distributions for many sites are reported in order to point out some general concepts related to this type of analyses: (i) the first mode corresponds to an earthquake caused by the closer source (or the source the site is enclosed into) and with low-to-moderate magnitude, (ii) the second mode accounts for the influence of the more distant zones usually with larger magnitude, and (iii) moving from PGA to Sa, the number of sites with two design earthquakes increases. Moreover sites enclosed or close to a seismic source zone with high seismicity are characterized by an unimodal disaggregation PDF and, therefore, a single design earthquake is identified although it is however a synthetic representation of a distribution affected by some dispersions. In the most of Italian cases two design earthquakes can be identified and in particular conditions, three design earthquakes have non negligible hazard contribution. In the latter cases, synthetic representation based on first and second modal values of PDF distribution is not enough representative. Dependency of design earthquakes form spectral period and from return period are analyzed theoretically and some examples are shown.

Limits of modal values are discussed when intervals of distance and magnitude influencing the hazard at the site are particularly large or when adopted disaggregation of hazard curves is not enough detailed (it happens in sites with low hazard). In order to validate results, comparisons between INGV data (when available) are shown.

Finally a discussion on the practical application of disaggregation results is provided underlining when characteristics of design earthquakes are expected to be relevant in record selection. Two ways are identified for increasing selection criteria and consequently improving representativeness of selected waveforms: definition of intervals of magnitude and distance (directly suggested by PDF disaggregation distribution) or definition of values of the cyclic response-related measure I_D whose attenuation law depends on M, R and local site conditions.

Disaggregation distribution of all Italian sites presented in this work and

additional criteria for record selection mentioned above have been implemented in the already existing software REXEL specifically developed for the searching of suites of waveforms, compatible on average to various types of code spectral shapes.

References

Ambraseys, N.N., Simpson, K.A. and Bommer, J.J. (1996). Prediction of Horizontal Response Spectra in Europe, Earthquake Engineering and Structural Dynamics 25, 371-400.

Baker, J.W. (2007). Probabilistic structural response assessment using vector-valued intensity measures. Earthquake Engineering and Structural Dynamics. 36:13, 1861-1883.

Baker, J.W. (2011). "The Conditional Mean Spectrum: A tool for ground motion selection," Journal of Structural Engineering, (in press).

Barani, S., Spallarossa, D. and Bazzurro, P. (2009). Disaggregation of probabilistic ground motion hazard in Italy. Bull. Seismol. Soc. Am. 99, 2638-2661.

Bazzurro, P., and C. A. Cornell (1999). Disaggregation of seismic hazard, Bull. Seismol. Soc. Am. 89, 501–520.

Bommer, J. J. (2004). Earthquake actions in seismic codes: Can current approaches meet the needs of PBSD? in Performance Based Seismic Design Concepts and Implementation, PEER Rept. 2004/05, Pacific Earthquake Engineering Research Center, University of California, Berkeley.

Convertito, V., Iervolino, I. and Herrero, A. (2009). Importance of mapping design earthquakes: insights for the southern apennines, Italy. Bull. Seismol. Soc. Am. 99, 2979-2991.

CS.LL.PP. (2008). DM 14 gennaio 2008 Norme Tecniche per le Costruzioni. Gazzetta Ufficiale della repubblica Italiana 29 (in Italian).

Eurocode 8 (2006). Design provisions for earthquake resistance of structures. Part 1.3: General rules. Specific rules for various materials and elements. Eur. Comm. for Standardisation, Brussels, Belgium.

Galasso, C., Chioccarelli, E., Iervolino, I. (2010). Advances in record selection for Italian Seismic code, Proc. Of 29° Convegno nazionale GNGTS, Prato, Italy, October 26-28, 2010.

Gruppo di Lavoro (2004). Redazione della mappa di pericolosità simica prevista dall'Ordinanza PCM 3274 del 20 Marzo 2003. Rapporto conclusivo per il Dipartimento della Protezione Civile, INGV, Milano-Roma, aprile 2004, 65pp. (in Italian)

Iervolino I., Manfredi G. (2008). Review of ground motion record selection strategies for dynamic structural analysis. In Modern Testing Techniques of Mechanical and Structural Systems, Oreste S. Bursi, David J. Wagg (Editors), CISM Courses and Lectures 502, Springer.

Iervolino, I., Galasso, C., Cosenza, E. (2010a). Rexel: computed aided record selection for code-based seismic structural analysis. Bulletin of Earthquake Engineering, 8, 339-362.

Iervolino, I., Giorgio, M., Galasso, C., Manfredi, G. (2010b) Improving seismic action assessment: conditional design maps for secondary intensity measures. Proc. of 14th European Conference on Earthquake Engineering, Ohrid, Republic of Macedonia, August 29 – September 4.

Iervolino, I., Manfredi, G., Cosenza, E. (2006). Ground-motion duration effects on nonlinear seismic response. Earthquake Engineering and Structural Dynamics. 35:1, 21-38.

Joyner, W.B., and Boore, D.M. (1981). Peak horizontal acceleration and velocity from strong-motion records including records from the 1979 Imperial Valley, California, earthquake. Bull. Seismol. Soc.Am. 71, 2011–2038.

Manfredi, G. (2001). Evaluation of seismic energy demand. Earthquake Engineering and Structural Dynamics. 30:4, 485-499.

McGuire, R. 1995. Probabilistic seismic hazard analysis and design earthquakes: Closing the loop. Bulletin of the Seismological Society of America, 85: 1275-1284.

Meletti, C., Galadini, F., Valensise, G., Stucchi, M., Basili, R., Barba, S., Vannucci, G. and Boschi, E. (2008). A seismic source zone model for the seismic hazard assessment of the Italian territory, Tectonophysics 450, 85–108.

Sabetta, F., Pugliese, A. (1996) Estimation of Response Spectra and Simulations of Nonstationary Earthquake ground Motion, Bull. Seism. Soc. Am., 86(2), 337-352.

Stucchi, M., Meletti, C., Montaldo, V., Crowley, H. Calvi, G. M. and Boschi, Enzo. (2010), Seismic hazard assessment (2003-2009) for the Italian building code, Bulletin of Seismological Society of America, (submitted for pubblication).

CHAPTER 3.
NEAR-SOURCE SEISMIC DEMAND AND PULSE-LIKE RECORDS

3.1 Introduction

In the case of an earthquake, ground motion recorded at near-source sites may be subjected to rupture directivity effects which result in a low frequency full cycle velocity pulse at the beginning of the signal. The occurrence of this effect depends on the rupture process and on the geometrical configuration of the fault and the site. More specifically, according to Somerville et al. (1997) the seismic energy radiated from the source arrives almost in single large pulse of motion if: the rupture propagates toward the site, the direction of slip on the fault is aligned with the site, and the propagation velocity of rupture is almost as large as the shear wave velocity. Figure 3.1a sketches rupture directivity effect in the simple case of an unilateral strike-slip fault. As the rupture, which may be seen as a point source moving along the fault, goes away from the epicenter, it radiates energy in seismic waves originated at different instants. Roughly speaking, the wave fronts tend to all arrive at the same time in site 2, this may be seen as *constructive interference* of waves. Conversely, in site 1, with respect to which the rupture moves away, waves radiated in different instants tend also to arrive in different moments. Therefore, in the former case the energy is concentrated in a high amplitude and short duration (impulsive)

motion, while in the latter the energy is spread over a larger amount of time and in an lower amplitude signal (Singh, 1985 and Reiter, 1990).

Because of the radiation pattern, in the case of strike-slip ruptures, directivity pulses are oriented in the strike-normal direction that corresponds to the fault-normal direction (Somerville et al., 1997). In dip-slip earthquakes, the rupture directivity pulse is expected in the direction normal to the fault dip, and should have components in both the vertical and the horizontal strike-normal direction[5] (Somerville, 2005). In the strike-parallel direction minor directivity effects, if any, are expected. Hereinafter, horizontal ground-motion components in strike-normal and strike-parallel directions will be referred to as fault-normal (FN) and fault-parallel (FP), Figure 3.1b.

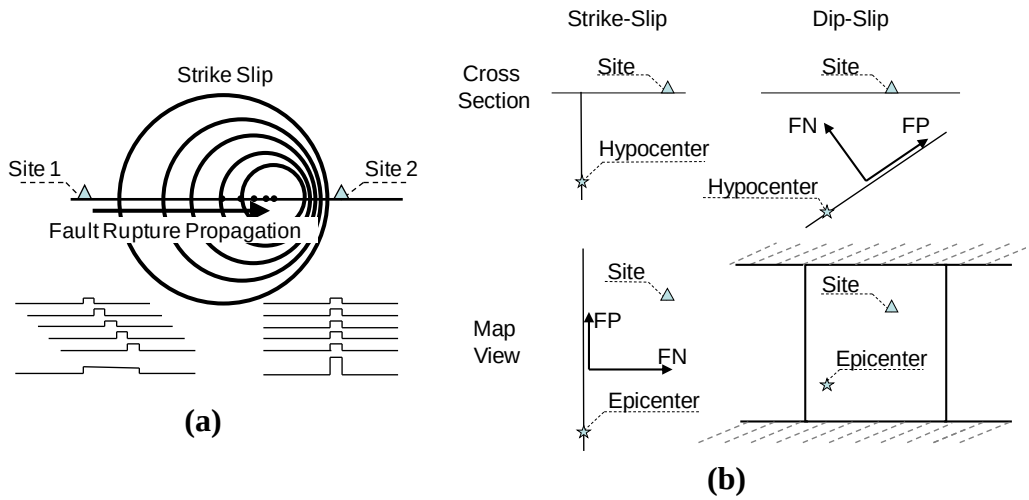

***Figure 3.1**. (a) Directivity of seismic energy: snapshot of wave fronts (adapted from Singh, 1985); (b) directions of effects' observation for strike-slip and dip-slip cases (adapted from Somerville, 2005).*

Because rupture and propagation of waves in actual earthquakes are much more complex than what just discussed, other factors perturb the

[5] It is to recall that in dip-slip earthquake also the *fling step* may appear in the strike-normal direction. It is related to the permanent ground deformation (i.e., residual displacement) and results in a half cycle pulse, differing from directivity which is expected to be a full cycle pulse (Somerville et al., 1997).

conditions to clearly observe velocity pulses and not all near-fault locations experience forward directivity effects in a given event; conversely, directivity may occur at sites apparently not prone to pulse-like ground motion (Bray and Rodriguez-Marek, 2004). On the other hand, pulse-type records are of interest to structural engineering because the seismic action is expected to be peculiar with respect to non-pulse-like records (*ordinary* in the following), that is: (1) the elastic demand of pulse-like signals is generally larger than that of ordinary recordings, particularly concerning the fault-normal direction; (2) the spectral shape is non-standard with an increment of spectral ordinates in the range around the pulse period; (3) because the pulse period is generally a low frequency one (i.e., in the same order of magnitude of that of the most of common structures) the inelastic demand can be particularly high (Tothong and Luco, 2007) and developed in a comparatively short time which may facilitate fragile collapse mechanisms in structures not properly designed. Finally, although this section focuses on low frequency pulse-like records, it is to recall that some researchers (e.g., Boatwright, 2007) also believe directivity may affect peak values of motion as peak ground acceleration (PGA).

In the following the amplification of elastic and inelastic seismic demands for pulse-like fault-normal records and the peculiar spectral shape driven by the pulses are investigated first with respect to fault-parallel and non-pulse-like near-source motions. The dataset is a subset of FN- and FP-rotated records from the next generation attenuation project (NGA) database and analyzed by Baker (2007). The results from this analysis may help the current research undergoing to adjust probabilistic seismic hazard analysis to account for pulse-like records occurrence (Iervolino and Cornell, 2008) and to quantify the structural effects (Tothong and Luco, 2007 and Baker, 2008). In this thesis they are also used as a benchmark to investigate directivity effects in the recent April 6th 2009 L'Aquila earthquake (moment magnitude or, M_w, 6.3) (see Chapter 4).

3.2 Pulse-like Seismic Action

In order to identify the peculiar features of impulsive signals in terms of seismic action on structures, a dataset from the NGA database (http://peer.berkeley.edu/products/nga_project.html) was considered. It determinedly includes records identified as pulses as well as signals in which the pulses were not found, this is required to enlighten the specific characteristics, in terms of structural demand, of pulse-like records. NGA records, in fact, were classified as "pulse-like" and "non-pulse-like" by Baker (2007) via a wavelets-based algorithm, which assigns a score, a real number between 0 and 1, to each record and determines the pulse period (Tp). The larger the score the more likely the record is to show a pulse. Only the fault-normal ground motions having a pulse score equal or larger than 0.85 were, arbitrarily, counted as pulse-type records. Note that pulses may possibly be indentified also in fault-parallel components, but these cases are not counted herein within the group of pulse-like records, although the behavior of FP components is investigated for those ground motions where FN is pulse; moreover, the algorithm does not detect fling as the wavelet functions used have zero residual displacement. In fact, the considered pulse-like signals are the same utilized in (Iervolino and Cornell, 2008): this selection slightly differs from that proposed by Baker (2007) but it is based on the analysis of the same database. It consists of 73 records from 23 events, 12 of which are strike-slip (Table 3.1).

Table 3.1 *Analyzed NGA records.*

Type	Events	Records	Pulse-Like Records
Strike-Slip	12	133	34
Non-Strike-Slip	11	229	39
Total	*23*	*352*	*73*

The events' M_w ranges from 5.2 to 7.5. The number of records from strike-slip events is 133, the records identified as pulses in the given dataset are 34. Other records coming from other faulting mechanisms which are non-

strike-slip are 229, 39 of which are identified as pulses (see Iervolino and Cornell, 2008 for details and for a complete list of pulse-like records). Note that in the following no distinction will be applied to records from different faulting styles, as results of the analyses do not support to keep such a difference.

3.2.1 Elastic demand and spectral shape

The first peculiarity of pulse-like records is related to the elastic seismic demand. To investigate it, the ratio of elastic spectral displacement at various periods (T) in the FN direction, $S_{d,e\ FN}(T)$, with respect to the FP component, $S_{d,e\ FP}(T)$, was computed. It is expected that because the pulse is to be observed mostly in the fault-normal component, the FN over FP ratio is larger for ground motions where the FN is identified as pulse-like with respect to records where FN is non-pulse-like. This is given in terms of average of the natural logarithm, as a function of the T over Tp ratio, in Figure 3.2a. Dashed lines are the averages plus and minus one standard deviation. Although dispersion is very high, as usually happens for ground motion amplitudes, it is quite clear that, if there are pulse-like signals, elastic FN demand is about 50% higher than FP (maximum value of FN over FP spectral displacement ratio is 1.57). Conversely, if there are no pulse-like signals in the fault-normal component, seismic demands in FN and FP directions are comparable. The second feature investigated, and probably the most important, is the peculiar spectral shape of pulse-like signals. In fact, spectra of these records have an increment of acceleration ordinates (or a "bump") in a range of periods around Tp. This is particularly critical as current attenuation relationships are not able to describe it and therefore seismic hazard and demand analyses may be potentially un-conservative. In Table 3.2 the pulse periods found in the dataset are divided in bins and for each bin the number of pulse-like records is shown. In Figure 3.2b the average elastic acceleration spectra of pulse-like records for some of the bins, the most significant for the dynamic behavior of ordinary structures, are given. To compare different ground motions, all spectra were normalized; i.e.,

all ordinates (Sa) were divided by the PGA. It may be observed the non-standard shape of pulse-like records.

Table 3.2 *Number of records for bins of Tp.*

Tp	[0s,1s[	[1s,2s[	[2s,3s[	[3s,4s[	[4s,5s[	[5s,6s[	[6s,12s[
No. of records	18	18	8	10	9	5	5

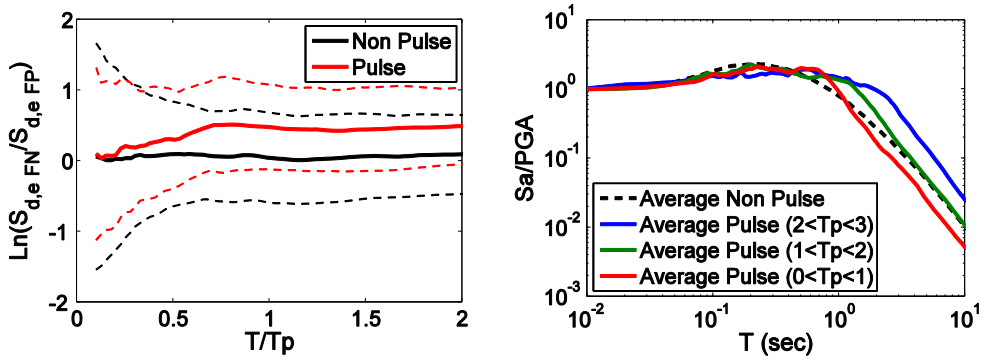

Figure 3.2. *(a) FN/FP elastic displacement ratios; (b) Average elastic acceleration spectra for bins of Tp.*

However, normalization by means of PGA, used in Figure 3.2b, works in the high frequency range only. Therefore, the elastic demand should be better analyzed considering the deviations of the considered ground motion intensity measure (IM) from what computed by an appropriate ground motion prediction equation (GMPE or *attenuation law*); i.e., the ε values in Eq. 1.

$$\varepsilon = \left[\log(IM) - \overline{\log(IM)}\right] \Big/ \sigma_{\log(IM)} \qquad (1)$$

In Eq. 1: IM is the recorded ground motion parameter; $\overline{\log(IM)}$ is the mean of the logarithms of IM obtained from the attenuation relationship; and $\sigma_{\log(IM)}$ is the standard deviation of the logarithms of IM, still from the GMPE. The used GMPE is that from Boore and Atkinson (2008) and Figure 3.3 shows

the ε values[6], for the FN and FP components in the case of pulse-like (a) and non-pulse-like (b) ground motions. Results of ε for pulse-like records before rotation have a bump around T equal to Tp, but it is never higher than 1. FN-rotated records have the same shape but they have maxima close to 2. In the case of ground motions where FN is identified as non-pulse-like, ε does not show a clear trend[7] (Figure 3.3b). Moreover, rotation does not affect the results significantly. Comparison of pulse-like and non-pulse-like records also shows that ε values in the former case are systematically higher than the latter confirming that the pulse-like are generally stronger than non-pulse-like.

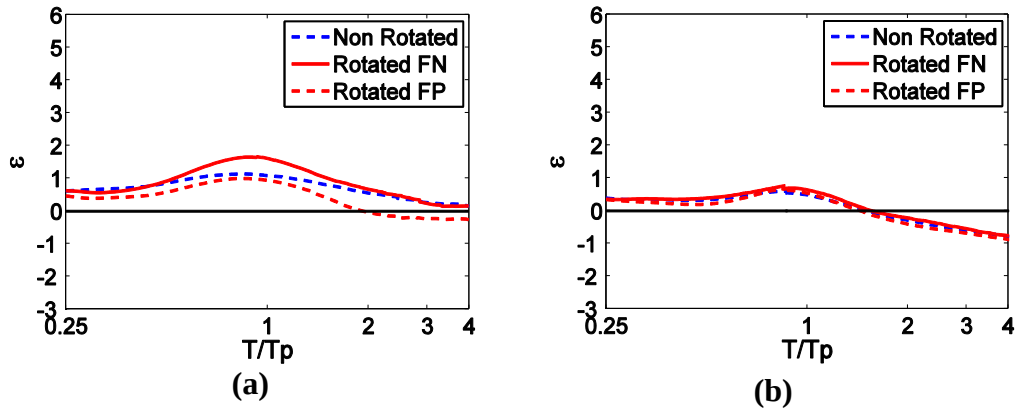

Figure 3.3. *Average ε values for ground motions where FN is pulse-like (a) and non-pulse-like (b).*

[6] The GMPE in Boore and Atkinson (2008) uses GMRotI as the IM (the 50th percentile of the geometric means of spectral accelerations computed for all non-redundant rotation angles of horizontal 2-component ground motion). GMRotI was used herein for the non rotated records; for FN and FP components the elastic spectral acceleration, $S_{a,e}(T)$, was used as the IM while, in principle, the GMPE should be transformed consistently (see Beyer and Bommer (2006) for a discussion). All the parameters required to compute the GMPE were available for the considered records via the NGA flatfile (http://peer.berkeley.edu/assets/NGA_Flatfile.xls).

[7] A small bump trend may be observed also in the non-pulse-like records. This is believed to be related to the fact that these records, for which a pulse period was always identified by Baker (2007), may have a pulse feature of some significance (e.g., from site effects or other factors) which the plot in terms of T/Tp magnifies.

It is to note that quantifying ε for pulse-like records allows to account for the peculiar spectral shape modifying ordinary GMPEs without requiring to fit a specific one. In this direction, Baker (2008) proposed a modification factor for an existing GMPE (calibrated on that of Boore and Atkinson, 2008):

$$\overline{\overline{\ln\left(S_{a,e}(T)\right)}} = \overline{\ln\left(S_{a,e}(T)\right)} + e^{-\left(\ln\left(T/T_p\right)\right)^2} \qquad (2)$$

where $\overline{\overline{\ln\left(S_{a,e}(T)\right)}}$ is the predicted spectral acceleration modified for pulse-like features in ground motion and the last term in the right hand side models the bump[8] of spectral ordinates with a maximum at T equal to Tp. This will be applied in Chapter 4 section 4.3.2 to a GMPE for Italy and to ground motion records of L'Aquila earthquake. In general it may be used to adjust probabilistic seismic hazard analysis to account for near-source effects (Iervolino and Cornell, 2008 and Tothong et al. 2007).

3.2.2 Integral parameters of ground motions

Two integral ground motion intensity measures were also computed for the NGA records to see whether there are significant near-source effects on signals' *duration*: the Arias intensity (A_I), and the significant duration (S_D) (Hancock and Bommer, 2006). Table 3.3 shows the medians and the differences between 25th and 75th percentiles of the empirical distributions (range), both being robust statistical estimators.

[8] Note that this modification of attenuation may be considered as a *narrow band* one (Somerville, 2003); i.e., elastic demand is magnified for selected frequency corresponding to the pulse period. Former models to modify ordinary GMPEs to account for directivity are *broad band*; e.g., that of Somerville et al. (1997).

Table 3.3 *Integral IMs.*

			A_I [cm/sec]		S_D [sec]	
Type		Sample Size	Median	Range	Median	Range
Pulse-Like	FN	73	0.09	0.15	8.42	5.82
	FP	73	0.07	0.13	9.10	5.12
Non-Pulse-Like	FN	289	0.04	0.09	10.93	6.58
	FP	289	0.04	0.08	11.10	6.69

A_I is a measure of energy; i.e., it is function of event magnitude, source-to-site distance and soil conditions, it can be used only to compare the same signals differently rotated. It is expected that, for pulse-like records, the A_I FN/FP ratio is systematically higher than one because FN is more energetic (see section 3.2.1). In fact, ratios of medians are 1.23 (with standard deviation equal to 0.63) and 1.07 (with standard deviation equal to 0.57) for pulse-like and non-pulse-like, respectively.

S_D is the time in which the ground motion releases 90% of its total energy, and it may be used to compare signals from different sites and earthquakes. It is expected that pulse-like signals have a significant duration lower than non-pulse-like. Values in Table 3.3 seem to qualitatively[9] confirm it with median values of 8.42 versus 10.93 for the FN components of pulse-like and non-pulse-like records, respectively. Figure 3.4 shows the histograms of A_I (a) and S_D (b) and their median values (vertical dashed lines).

[9] Statistical tests on integral parameters distributions would be useful to confirm or not these comparisons, but the large sample sizes and asymmetric shape distributions (see Figure 3.4) suggest that the most parametric tests would not be useful, while non-parametric are not as powerful.

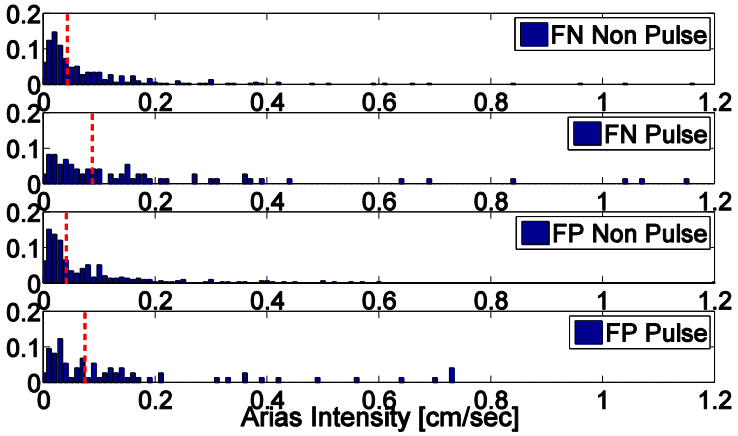

(a)

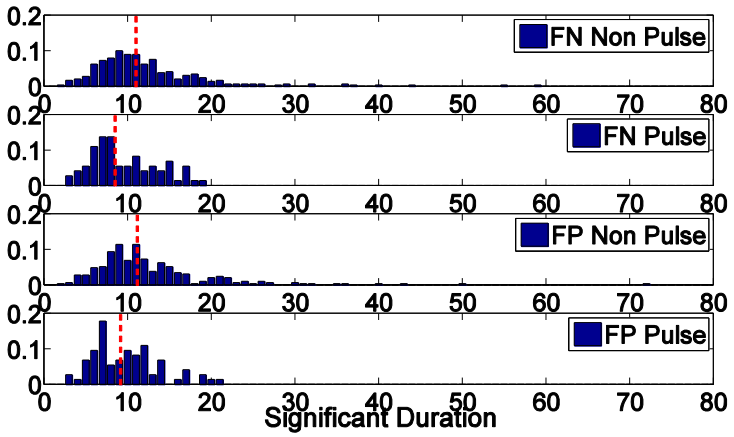

(b)

Figure 3.4. *Arias Intensity (a) and Significant Duration (b) histograms for NGA records.*

3.2.3 Inelastic demand and displacement amplification factor

In order to analyze pulse-like effects on non-linear structures, bilinear single degree of freedom (SDoF) systems, with 3% hardening ratio, 5% damping ratio, and different values of the strength reduction factor (R_s), Eq. 3, were considered.

$$R_s = S_{a,e}(T) \cdot m / F_y \tag{3}$$

In Eq. 3 T is the oscillation period of the SDoF; m is its mass; and F_y is its yielding strength.

From this analysis there is the evidence that, also in the non-linear case, the FN over FP ratio is comparatively larger for those records in which the fault-normal component is identified as pulse-like with respect to ground motions where FN is non-pulse-like (Figure 3.5a, b and c). Ranges of the FN over FP ratio are 1.39÷1.67, 1.20÷1.54 and 1.40÷1.72 for R_s equal to 2, 4 and 6, respectively. Moreover, as a consequence of the peculiar spectral shape observed in Section 3.2.1, unexpected displacement demand may occur in structures having non-linear oscillations in a period range around to that of the pulse. A way to visualize this is a plot of the logarithm of the inelastic ($S_{d,i}$) to elastic ($S_{d,e}$) displacement ratio of the bilinear SDoF systems already described. Figure 3.5d, e and f, report, for the three R_s values, the averages for: FN and FP components of ground-motions where FN is pulse-like (*Pulse - Fault normal* and *Fault Parallel* in the legend), and for non-pulse-like FN components (*Non Pulse - Fault normal* in the legend). These latter records are considered ordinary and, therefore, are used as a benchmark. The FP components of ground-motions where FN is non-pulse-like were not plotted as their curve perfectly overlaps with that of FN (as the ε plots of Figure 3.3b suggest).

Curves for the FN pulse-like records show an increment in the $S_{d,i}/S_{d,e}$ ratio at $T/T_p \approx 0.3 \div 0.5$, indicating a comparatively larger inelastic demand of this kind of near-fault ground motions because the elongated structural period drifts toward the peak at the pulse period Tp (Tothong and Cornell, 2006).

FP components of records where FN is pulse-like show a lower increment with respect to FN, nevertheless it is not perfectly overlapping with that of ordinary records. This is expected to some extent because, as discussed, in the strike-parallel direction directivity effects are lower than in fault-normal direction, but they seem to be not absent (see Bray and Rodriguez-Marek ,2004 for a discussion about nature and seismic demand of FP-rotated near-source records).

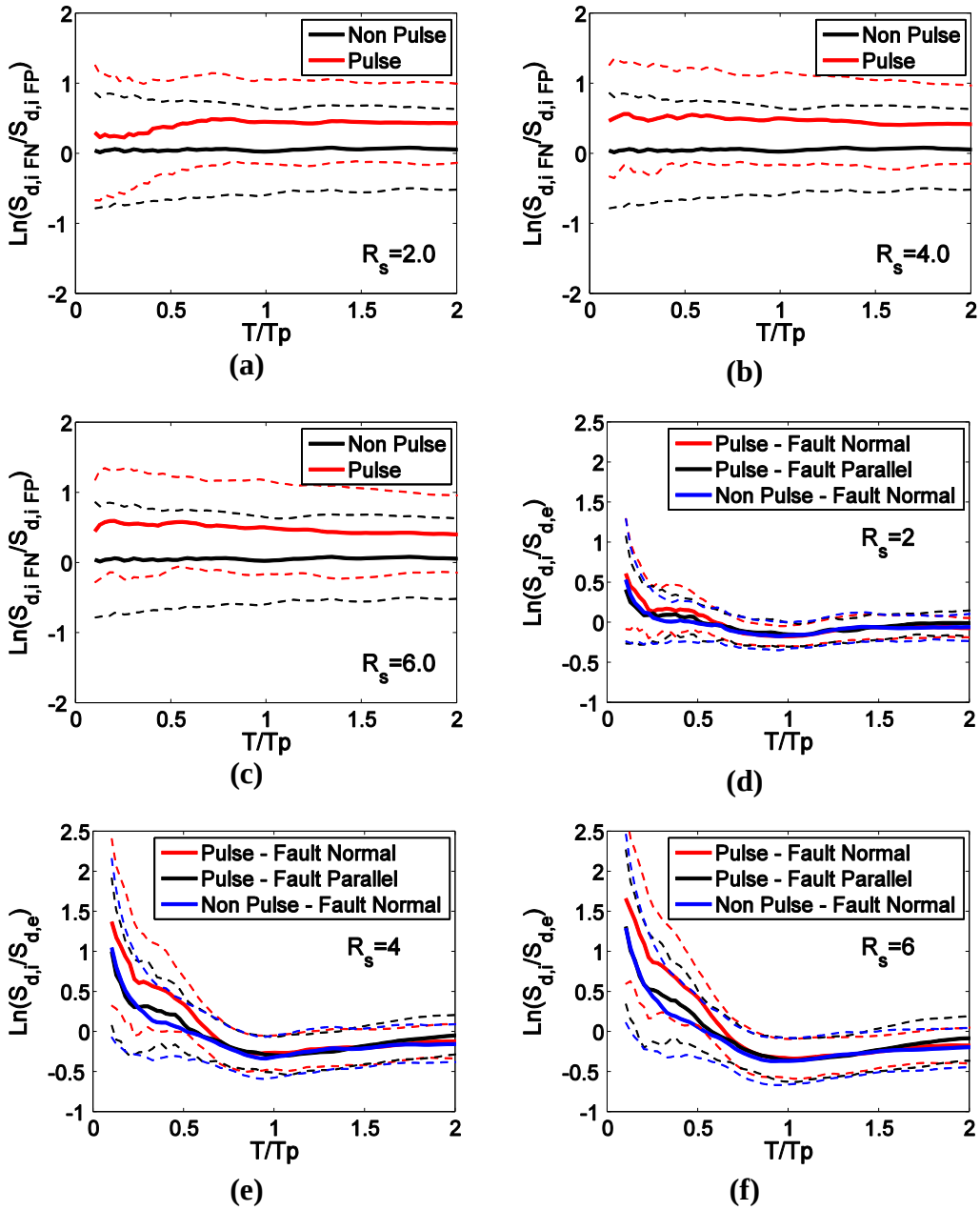

Figure 3.5*. FN over FP inelastic displacement ratios (a, b and c) and inelastic to elastic displacement demand ratios (d, e, and f).*

To quantify what derived from Figure 3.5, Table 3.4 reports the maxima of the increments in the $S_{d,i}/S_{d,e}$ ratio of FN pulse-like with respect to FN non-pulse-like records for the three R_s values. More precisely, Table 3.4 shows T/Tp and $S_{d,i}/S_{d,e}$ median ratios for pulse-like ground-motions in FN and FP directions and $S_{d,i}/S_{d,e}$ ratios for FN non-pulse-like records. In FN direction the increments of the pulse-like with respect to the non-pulse-like are equal to 18%, 53% and 71% for R_s equal to 2, 4 and 6, respectively. Increments of the same for ratio, for FP components of records where FN is pulse-like with respect to non-pulse-like FN ground motions, are equal to 9%, 15% and 21%. As a consequence of these increments, inelastic to elastic ratio is not similar to that of ordinary records; i.e., it may violate the *equal displacement rule* and therefore should be accounted for properly in seismic design and assessment.

Table 3.4 *Values of $S_{d,i}/S_{d,e}$ ratios corresponding to maximum increment for FN pulse-like with respect to FN non-pulse-like.*

	T/Tp	Pulse - FN	Pulse - FP	Non Pulse - FN
$R_s = 2$	0.325	1.196	1.104	1.015
$R_s = 4$	0.350	1.738	1.304	1.133
$R_s = 6$	0.325	2.182	1.543	1.278

3.3 Conclusions

Although the directivity-induced pulses problem is known since many years, a quantification of its significance for structural engineering and recognition of its occurrence in observed earthquakes is not well established yet. In this chapter, some recent tools to investigate pulse-like records were applied in order to analyze the issue as much as possible from a quantitative point of view and in terms of seismic action.

The amplification of elastic and inelastic seismic demands for pulse-like fault-normal records and the peculiar spectral shape driven by pulses were investigated first with respect to fault-parallel and non-pulse-like (ordinary) near-source ground motions. The dataset is a subset of FN- and FP-rotated

records from the next generation attenuation project (NGA) database. Analyses show that pulse-like signals are characterized by fault normal records generally stronger than both fault parallel components and non-pulse-like ground motions. Moreover, fault-normal pulse-like signals are also characterized by a non-standard spectral shape with an increment of spectral ordinates in a range around the pulse period. Comparisons between pulse-like and non-pulse-like records show that inelastic to elastic seismic spectral displacement ratio for pulse-like records can be 20% to 70% higher than that of ordinary motions depending on the non-linearity level. This result can be explained by the peculiar spectral shape of pulse-like records.

References

Baker, J. W. (2007) Quantitative Classification of Near-Fault Ground Motions Using Wavelet Analysis, Bull. Seism. Soc. Am., 97(5), 1486-1501.

Baker, J. W. (2008) Identification of Near-Fault Velocity and Prediction of Resulting Response Spectra, Proceeding of Geotechnical Earthquake Engn. Struct. Dyn. IV, Sacramento, CA. [Available at http://www.stanford.edu/~bakerjw/Documents/Baker%20(2008)%20Pulse%20ID,%20GEESD%20for%20distribution.pdf, last accessed 2009 august the 2nd.]

Beyer, K., Bommer, J. J. (2006) Relationships between Median Values and between Aleatory Variabilities for Different Definitions of the Horizontal Component of Motion, Bull. Seism. Soc. Am., 96(4A), 1512-1522.

Boatwright, J. (2007) The Persistence of Directivity in Small Earthquakes, Bull. Seism. Soc. Am., 97(6), 1850-1861.

Boore, D. M., Atkinson, G. M. (2008) Ground-Motion Prediction Equations for the Average Horizontal Component of PGA, PGV and 5%-Damped PSA at Spectral Period between 0.01s and 10.0 s, Earthquake Spectra, 24(1), 99-138.

Bray, J. D., Rodriguez-Marek, A. (2004) Characterization of Forward-directivity Ground Motions in the Near-fault Region. Soil Dyn. Earthquake Eng., 24(11), 815-828.

Hancock, J., Bommer, J. J. (2006) A State-of-Knowledge Review of the Influence of Strong-Motion Duration on Structural Damage, Earthquake Spectra, 22(3), 827-845.

Iervolino, I., Cornell, C. A. (2008) Probability of Occurrence of Velocity Pulses in Near-Source Ground Motions, Bull. Seism. Soc. Am., 98(5), 2262-2277.

Reiter, L. (1990) Earthquake Hazard Analysis, Issues and Insights, Columbia University Press, NY.

Singh, P. J. (1985) Earthquake Ground Motions: Implications for Designing Structures and Reconciling Structural Damage, Earthquake Spectra 1(2), 239-270.

Somerville, P. G. (2003) Magnitude Scaling of the Near Fault Rupture Directivity Pulse, Physics of the Earth and Planetary Interiors, 137, 201-212.

Somerville, P. G. (2005) Engineering Characterization of Near-Fault Ground Motions, Proceeding of 2005 NZSEE Conference, Wairakei, NZ.

Somerville, P. G., Smith, N. F., Graves, R.W., Abrahamson, N. A. (1997) Modification of Empirical Strong Motion Attenuation Relations to Include the Amplitude and Duration Effect of Rupture Directivity, Seism. Res. Lett., 68(1), 199-122.

Tothong, P., Cornell C. A. (2006) Probabilistic Seismic Demand Analysis Using Advanced Ground Motion Intensity Measures, Attenuation Relationships, and Near Fault Effect, PEER Report 2006/11, Pacific Earthquake Engineering Reserch Center, Berkeley, CA.

Tothong, P., Cornell, C. A., Baker, J. W. (2007) Explicit Directivity-Pulse Inclusion in Probabilistic Seismic Hazard Analysis, Earthquake Spectra, 23(4), 867-891.

Tothong, P., Luco, N. (2007) Probabilistic seismic demand analysis using advanced ground motion intensity measures, Earthquake Eng. Struct. Dyn., 36, 1837–1860.

CHAPTER 4.
DIRECTIVITY EFFECTS: A DISCUSSION FOR L'AQUILA EARTHQUAKE.

4.1 Introduction

In this section pulse the M_w 6.3 April 6 mainshock of the L'Aquila earthquake sequence is studied. First general information and simple analyses of recorded ground motions are reported. Then the attention is focused on possible pulse-like effects in the event. In particular: (i) the information about the source of the earthquake and recording sites within about 30 km in terms of closest distance to fault rupture is reviewed; (ii) near-source records are rotated in terms of FN and FP directions, and the seismic action is analyzed comparing those signals in which velocity pulses are found to those non-pulse-like of the same event and to the NGA results; (iii) a model for the probability of occurrence of velocity pulses, based on the source/site geometry, is applied to the fault in question; (iv) finally, an analysis including the vertical component of ground motions is shown.

4.2 Near Source Features

The L'Aquila earthquake is the third strongest seismic event producing strong motion records in Italy, after the Irpinia (1980, MW 6.9) and Friuli (1976, MW 6.4) earthquakes. This event, together with the 12 strongest aftershocks (MW > 4.0) provided a unique strong motion dataset in Italy, especially due to the amount and intensity of near-fault records. The dataset consists of about 300 digital accelerograms (270 of which belonging to the Accelerometric National Network of the Italian Civil Protection, RAN), with a very good signal-to-noise ratio, recorded by about 70 stations, installed on different site conditions at distance ranging from 0 to 300 km. The national and international relevance of this dataset is enhanced by its contribution to fill gaps in the magnitude-distance distribution of worldwide strong motion records, especially for normal-fault earthquakes (Ameri et al., 2009).

Results of seismological studies have shown that the Abruzzo event was a *normal* faulting earthquake (or *dip-slip*), with a rectangular rupture plane of about 17x14km^2 and located at a depth between 12 km and 0.6 km from the surface. The rupture plan has a strike of 142°, a dip of 50° and a rake of 90° (D. Cheloni[⊥], written communication). Coordinates of the vertices of the rupture plane and of the hypocenter are reported in Table 4.1. These data are not uniquely identified by all seismologists, but the various available estimates are not very different each other. Propagation of the rupture seems to have occurred *up-dip* first, and then in the direction parallel to the strike.

Table 4.1 *Hypocenter and rupture plane coordinates.*

	Fault Plane Vertices				Hypocenter
Longitude	13.424°	13.552°	13.465°	13.336°	13.353°
Latitude	42.405°	42.293°	42.238°	42.351°	42.340°
Depth (km)	0.600	0.600	11.800	11.800	11.800

[⊥] Istituto Nazionale di Geofisica e Vulcanologia (INGV), Centro Nazionale Terremoti (CNT), Rome, Italy.

Figure 4.1 shows the projection of rupture surface with the epicentral location, the code of RAN stations[10], their Eurocode 8 (EC8) (CEN, 2003) site class (Ameri et al., 2009), and some severely damaged towns and villages (Verderame et al., 2009).

The acceleration waveforms were corrected by the authors in terms of linear baseline correction and Butterworth Bandpass filter (low-cut = 0.1 Hz, high-cut 2 = 25 Hz, order = 4). It is to recall that some authors (Akkar and Bommer, 2006) have discussed how a constant cut-off filter may affect the long-period components of the ground motions and therefore it may be conservative for some of the records used in this article; further details on the corrected signals, which are available at http://www.reluis.it/, may be found in (Chioccarelli et al., 2009).

4.3 Preliminary signals's informations

Horizontal components of each record have been analyzed referring to original direction of accelerometers i.e. North-South (N-S) and East-West (E-W). These preliminary analyses are not focused on directivity effects and the aim is to provide additional information about ground motions. Such analyses are reported in Appendix B.

The horizontal components of each record were also rotated from N-S and E-W to fault-normal (FN) and fault-parallel (FP) directions (strike-normal and strike-parallel components; see Chapter 3, Section 3.1). All analyses of horizontal components will be referred to FN- and FP-rotated signals unless otherwise specified.

In this work, only stations with fault distance within about 30 km (13 in number) were considered because this is a generally accepted (although arbitrary) boundary for near-source effects. Table 4.2 shows some peak and

[10] All the analyses discussed in the following do not attempt to account for other near source effects which may cause spatial variability of ground motions; e.g., hanging/foot wall effects (Abrahamson and Somerville, 1996). This is also because most of near source stations lie on the hanging wall.

integral intensity measures of recorded ground motions at the near-source stations; i.e., PGA, Peak Ground Velocity (PGV), Peak Ground Displacement (PGD), A_I, and the Cosenza and Manfredi Index (I_D) (Cosenza et al., 1993), S_D and Bracketed Duration at 5% PGA (B_D) (Hancock and Bommer, 2006).

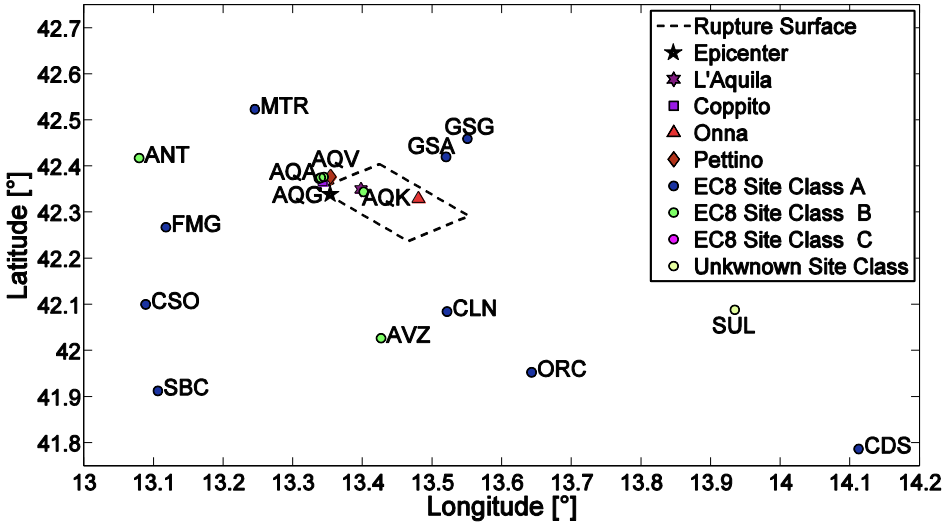

***Figure 4.1**. Map view of rupture surface and RAN accelerometric stations within about 60 km from the fault projection.*

***Table 4.2** Peak and integral IMs of L'Aquila near-source records.*

	Record	PGA [cm/sec^2]	PGV [cm/sec]	PGD[11] [cm]	A_I [cm/sec]	I_D [-]	S_D [sec]	B_D [sec]
1	AQV_FN	725.37	37.63	5.53	228.76	5.24	7.69	25.14
	AQV_FP	474.42	31.41	7.07	253.90	10.64	7.61	66.41
2	AQG_FN	357.16	34.08	8.19	114.47	5.88	8.16	18.23
	AQG_FP	391.79	26.60	5.45	144.91	8.68	8.45	25.17
3	AQA_FN	425.86	28.67	7.11	132.60	6.79	6.91	14.78
	AQA_FP	404.55	19.91	3.32	198.89	15.50	7.72	67.33

[11] Note that PGD is especially sensitive to the low-cut filter, therefore the reliability of listed PGD values is confined to the implemented filtering methodology.

4	AQK_FN	413.57	45.01	13.22	138.10	4.63	10.55	66.06
	AQK_FP	261.99	16.66	5.32	81.96	11.73	15.37	66.51
5	GSA_FN	153.52	10.91	3.35	37.13	13.86	9.38	25.53
	GSA_FP	197.58	6.02	1.37	46.50	24.48	8.02	24.10
6	CLN_FN	99.54	5.48	1.76	3.87	4.43	8.00	20.05
	CLN_FP	63.29	5.82	2.26	3.75	6.37	6.53	19.13
7	AVZ_FN	61.91	13.06	3.40	8.43	6.51	21.56	51.28
	AVZ_FP	63.41	9.89	3.54	9.14	9.10	18.25	49.76
8	MTR_FN	51.04	4.08	0.93	4.02	12.04	14.84	45.93
	MTR_FP	57.19	3.04	0.88	5.17	18.59	11.39	34.84
9	GSG_FN	20.31	3.66	2.14	0.81	6.81	10.65	33.28
	GSG_FP	25.52	2.31	0.71	0.69	7.33	10.97	25.59
10	FMG_FN	21.87	2.12	0.98	1.34	18.12	22.76	60.38
	FMG_FP	24.43	1.90	0.92	0.88	11.87	20.58	41.78
11	ANT_FN	26.66	2.25	0.47	1.67	17.33	21.68	54.48
	ANT_FP	19.19	1.99	0.43	0.96	15.74	22.87	64.52
12	CSO_FN	18.91	2.24	1.00	0.89	13.11	21.38	58.06
	CSO_FP	13.74	1.48	0.43	0.48	14.74	27.23	65.69
13	ORC_FN	72.64	6.88	1.11	4.77	5.97	10.24	30.10
	ORC_FP	31.85	2.86	0.99	1.83	12.60	14.00	50.95

4.3.1 Looking for Pulse-like records

The algorithm developed by Baker (2007) calculates, for each record, a score called *pulse indicator*. Records with score above 0.85 and below 0.15 are classified as pulses and non-pulses respectively, while signals with a score between these limits are considered *ambiguous*. Two further conditions are added in order to exclude pulse-like signals likely to not be related to directivity. The first one is that records with a pulse not occurring at the beginning of the record (i.e., *late* pulses) are not considered to be affected by directivity, the second one refers to PGV that has to be higher than 30cm/sec; this is claimed to exclude records with poor structural interest. In this work,

this latter condition is neglected consistently with (Iervolino and Cornell, 2008).

The procedure to identify pulses has been implemented by J.W. Baker* in some MATHWORKS-MATLAB® scripts and is publicly available at http://www.stanford.edu/~bakerjw/pulse-classification.html (last accessed November 2010). It was used to analyze L'Aquila records; Table 4.3 shows the results of pulse identification for the records of Table 4.2; identified pulse-like records are reported in bold. Thirteen stations were analyzed and six of them have a horizontal component classified as pulse-like: 5 of them in the FN direction and only one in the FP direction, AQV. The latter one has also the FN component classified as ambiguous and the elastic displacement spectra are similar in the two analyzed directions. The choice of neglecting the PGV limit significantly affects only the two results of GSG[12] (PGV equal to 3.66cm/sec) and ORC (PGV equal to 6.88cm/sec).

Table 4.3 *Results of pulse identification for horizontal components.*

Component	Pulse indicator	Late pulse indicator	PGV [cm/sec]	Classified as Pulse	Tp [sec]
AQV_FN	0.70	0.00	37.63	NO	0.53
AQV_FP	**0.85**	**0.00**	**31.41**	**YES**	**1.06**
AQG_FN	**1.00**	**0.00**	**34.08**	**YES**	**1.02**
AQG_FP	0.71	0.00	26.60	NO	1.11
AQA_FN	**0.93**	**0.00**	**28.67**	**YES**	**0.74**
AQA_FP	0.00	0.00	19.91	NO	0.62
AQK_FN	**1.00**	**0.00**	**45.01**	**YES**	**1.99**
AQK_FP	0.00	1.00	16.66	NO	1.26
GSA_FN	**0.72**	**0.00**	**10.91**	**YES**	**3.13**
GSA_FP	0.00	0.00	6.02	NO	1.97
CLN_FN	0.05	1.00	5.48	NO	5.17

* Stanford University, CA, US.

[12] GSG station seems, according to (Ameri et al., 2009), to be in tunnel 200m below the surface. Nevertheless, it was kept in the analyses also because it was found that removing it would not change the conclusions found.

CLN_FP	0.01	1.00	5.82	NO	4.81
AVZ_FN	0.97	1.00	13.06	NO	1.88
AVZ_FP	0.00	1.00	9.89	NO	1.61
MTR_FN	0.01	1.00	4.08	NO	2.60
MTR_FP	0.00	1.00	3.04	NO	2.16
GSG_FN	**0.95**	**0.00**	**3.66**	**YES**	**4.03**
GSG_FP	0.08	1.00	2.31	NO	5.17
FMG_FN	0.00	1.00	2.12	NO	4.03
FMG_FP	0.01	0.00	1.90	NO	4.76
ANT_FN	0.00	0.00	2.25	NO	0.95
ANT_FP	0.00	0.00	1.99	NO	2.76
CSO_FN	0.00	1.00	2.24	NO	4.82
CSO_FP	0.00	1.00	1.48	NO	2.22
ORC_FN	**0.92**	**0.00**	**6.88**	**YES**	**0.83**
ORC_FP	0.00	1.00	2.86	NO	4.47

Figure 4.2 shows an example of the algorithm's output for a pulse-like station (AQK) with recorded velocity, extracted pulses, residual signals and displacement time histories. FN and FP components are reported on the left and right panels, respectively. The former is pulse-like with score 1, and the latter is non-pulse-like with score 0.0. AQK is the stations with the strongest pulse-like signal in FN direction[13]. Plot of algorithm's analyses of all the other records are reported in Appendix A.

Studying ambiguous cases, authors have decided to classify as pulse-like also the FN signal of GSA. Elastic displacements spectra seem to confirm this choice (see the following section). All the other ambiguous cases were considered as non-pulse-like.

[13] It is to report, however, that Paolucci (2009) argues it may derive also from a site effect in combination with the source radiation.

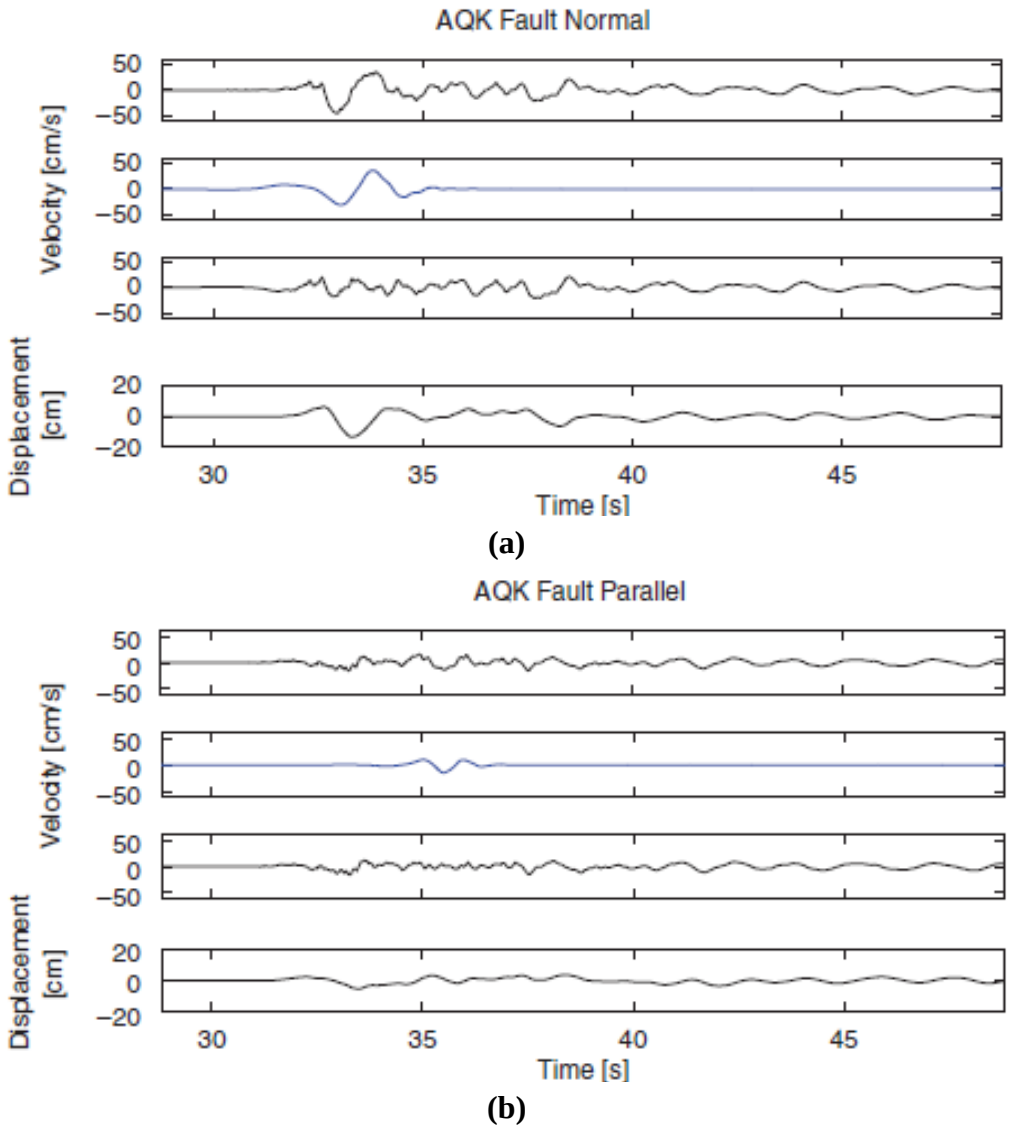

Figure 4.2*. From the top to the bottom: velocity time-history, extracted pulse, residual velocity, and displacement signal for FN (a) and FP (b) component of AQK.*

A model for the prediction of the pulse occurrence, $P[pulse]$, developed for PSHA purposes (Iervolino and Cornell, 2008) on the basis of the parameters indicated by Somerville et al. (1997), was applied to the fault of the earthquake as it may be useful to assess if pulses occurred where the

geometrical source-to-site configuration favors it. The parameters, in the case of dip-slip faults (see Figure 4.3), are: the closest distance to fault rupture (Clstd or R); the fraction of the rupture surface that lies between the hypocenter and the site (d); the angle between the direction of rupture propagation and the direction aligning the hypocenter and the site (φ). The considered model, Eq. 1, was obtained via logistic regression and is applicable for the 5km÷30km, 0km÷20km, 0°÷90° ranges of R, d, and φ, respectively.

$$P\left[\, pulse \middle| R, d, \varphi \right] = \frac{e^{0.553 - 0.055 \cdot R - 0.0267 \cdot d - 0.027 \cdot \varphi}}{1 + e^{0.553 - 0.055 \cdot R - 0.0267 \cdot d - 0.027 \cdot \varphi}} \quad (1)$$

Figure 4.3 shows schematically the geometrical predictors for three different cases of relative rupture-site position in the L'Aquila earthquake. The zones' definition refers to what is depicted in Figure 4.4: in case 0 φ is larger than 90°, while cases 1 and 2 only differ because of the geometrical relationship between the three parameters for predicting probability. Figure 4.4 shows the probability contours according to the model.

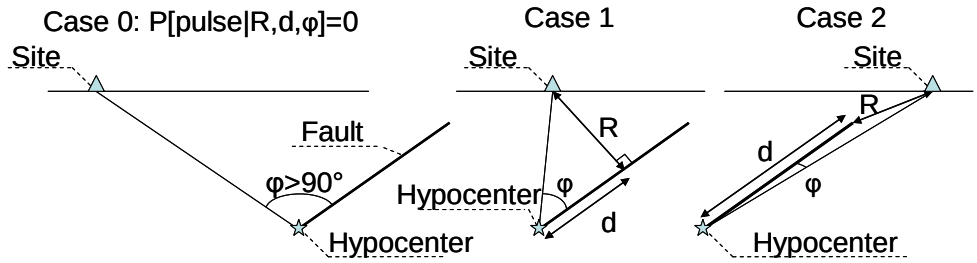

Figure 4.3*. Geometrical predictors for three different cases of relative rupture-site position.*

Table 4.4 shows values of geometrical predictors and pulse occurrence probability for the near-source stations. It is to point out that the occurrence probability is never larger than 0.5; this is because the model was developed generically for non-strike-slip earthquakes, which are often complex and in

which it is not easy to identify rupture directivity effects. Nevertheless, it may be used to highlight sites comparatively more likely to be affected by velocity pulses given the source geometry. From this point of view, results of pulse occurrence probability model are in general agreement (except ORC) with the results of algorithm for pulse-like identification[14].

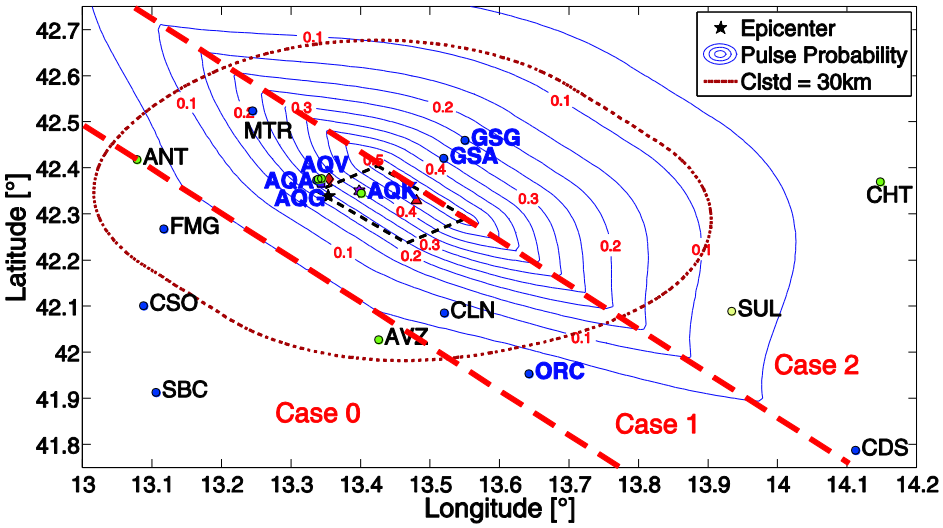

Figure 4.4. Contours of occurrence probability and accelerometric stations with pulse-like signals (blue).

Table 4.4 *Geometrical predictors and pulse occurrence probability for each accelerometric station.*

Station	Long.	Lat.	R (km)	d (km)	φ (deg)	P[pulse]
AQV	13.34°	42.38°	6.0	10.16	29.60	0.30
AQG	13.34°	42.37°	6.6	9.70	33.05	0.2
AQA	13.34°	42.38°	6.41	9.85	31.71	0.28
AQK	13.40°	42.34°	4.80	10.94	23.69	0.34

[14] It is to mention, for completeness, that seismologists (Ameri et al., 2009) identify directivity in the comparatively large PGA values observed along the S-E quadrant of Figure 4.1, although it is still controversial whether this may be because some geological futures favoring the propagation in this direction and whether directivity, as described at the beginning of the paper, may be found simply analyzing PGA.

GSA	13.52°	42.42°	7.14	14.21	14.79	0.35
CLN	13.52°	42.09°	20.77	3.78	74.13	0.06
AVZ	13.43°	42.03°	26.48	0.00	0.00	0.00
MTR	13.24°	42.52°	19.73	12.97	10.67	0.24
GSG	13.55°	42.46°	11.89	14.21	21.31	0.26
FMG	13.12°	42.27°	23.47	0.00	0.00	0.00
ANT	13.08°	42.42°	25.37	1.29	85.47	0.04
CSO	13.09°	42.10°	35.62	0.00	0.00	0.00
ORC	13.64°	41.95°	36.66	2.69	79.80	0.02

4.3.2 Seismic Action

In order to further confirm the identification of pulse-like records and to see whether they are of special interest for structural engineering because carrying non-ordinary seismic demand, a comparison of seismic action was carried out with NGA records (Chapet 3). First of all, the extracted Tp values were compared to the expected pulse period distribution computed via a period versus magnitude regression calculated on the NGA record dataset, although several others are available in literature (Somerville, 2003 and Baker, 2007). Eq. 2, gives the natural logarithm of Tp as a function of M_w with a standard deviation of the residuals equal to 0.59. Figure 4.5 shows a plot of Eq. 2 (solid line is the average, while dashed are plus and minus standard deviation of the residuals) and L'Aquila data.

$$\ln Tp = -6.19 + 1.07 \cdot M_W \qquad (2)$$

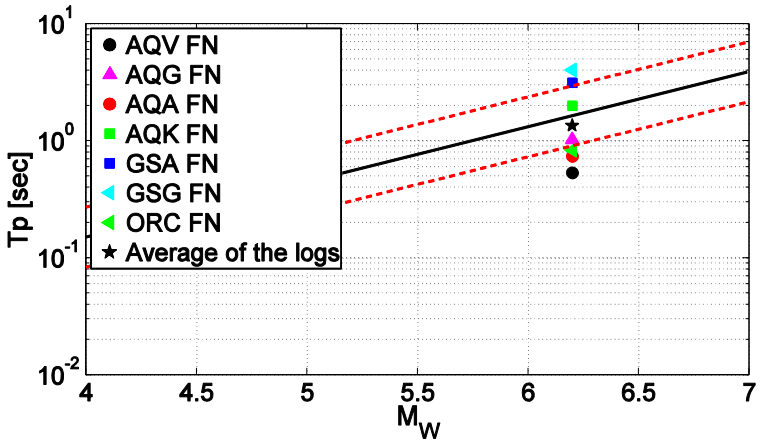

***Figure 4.5**. Comparison between extracted L'Aquila pulse periods and predicted values by regression of NGA data.*

In Figure 4.6, elastic displacement spectra of pulse-like stations are shown as a function of T normalized with respect to Tp. T over Tp ratio takes values between 0.1 and 2.0 and spectra are computed with steps of 0.025 sec. Signals are grouped as FN and FP, then in the first plot (4.6a) there are 6 pulse-like records and one non-pulse-like record (classified as ambiguous)[15].

The two components of AQV signals are very similar to each other; this is an expected result from the scores given by the algorithm. Moreover the figures show that the FN component of GSA is significantly different from FP. This is in good agreement with the choice of the authors about pulse classification of this station.

To quantify how much the FN components are stronger than the corresponding FPs, Figure 4.7 shows the averages of the natural logarithm of elastic and inelastic spectral displacement ratios. Comparing Figure 4.7 with Figure 3.5a, b and c (Chapter 3), it is to note that trends are similar to NGA results. Maximum values of FN over FP ratio are 1.71, 1.70, 2.10 and 1.98 respectively for R_s equal to 1, 2, 4, and 6.

[15] Because L'Aquila downtown FN record (AQK station) is clearly stronger than all others, to ensure robustness of results, all following considerations will be referred to the median values, as it is more robust then mean with respect to outliers.

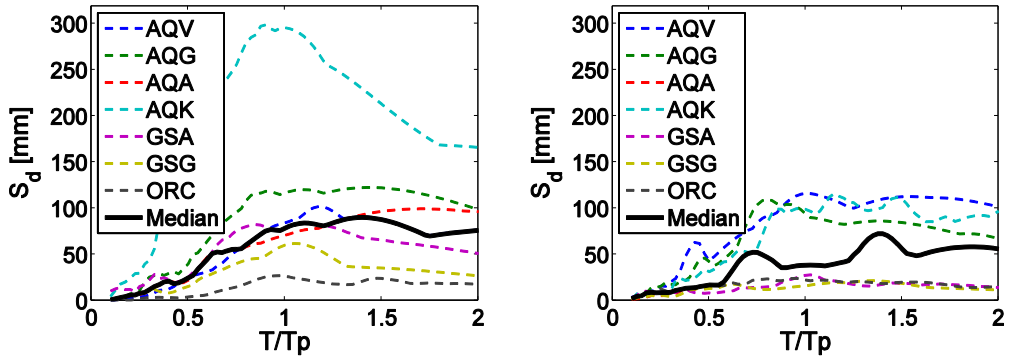

Figure 4.6*.. Elastic displacement spectra of pulse-like stations: (a) FN and (b) FP components.*

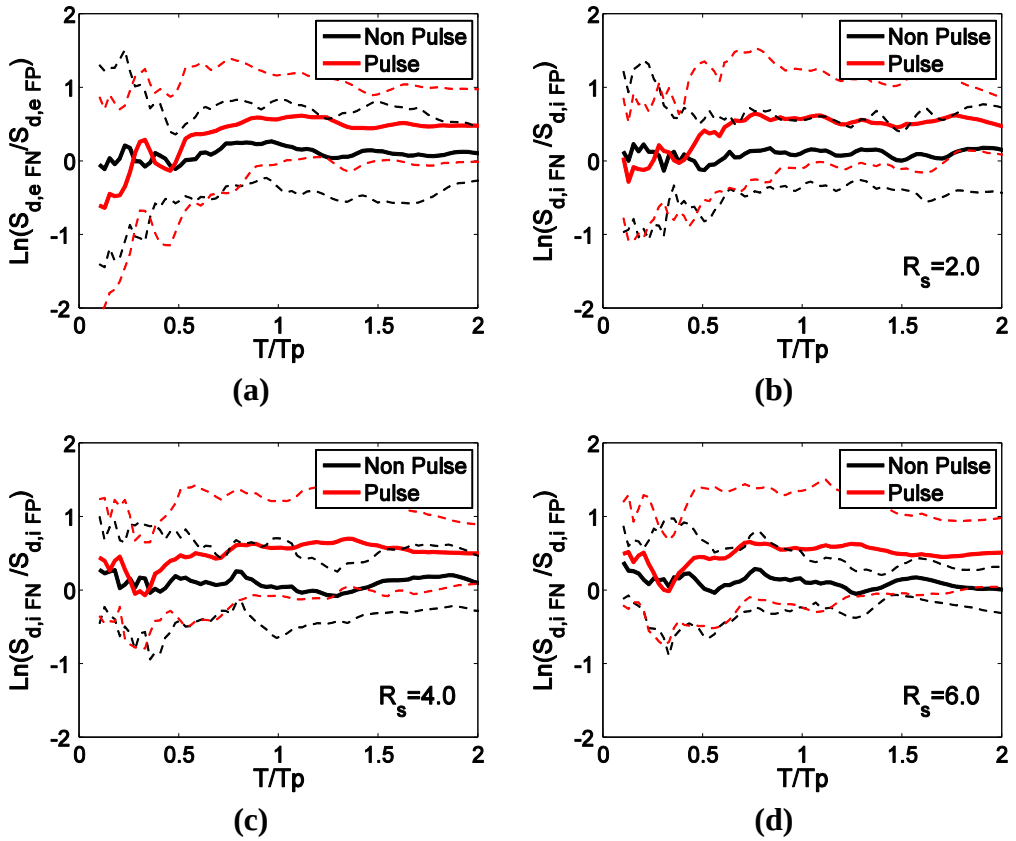

***Figure 4.7**. FN over FP elastic (a) and inelastic (b, c and d) displacement ratio for R_s = 2, 4 and 6.*

Figure 4.8 shows the inelastic to elastic displacement ratios versus the oscillator period divided by Tp. Plots, calculated for three R_s factors, are compared to NGA FN records. Although the small sample size, L'Aquila displacement ratios have shapes very similar to the NGA results for stations without pulse-like effects. Also results for pulse-like stations agree to what expected although also the FP signals seem to be severe.

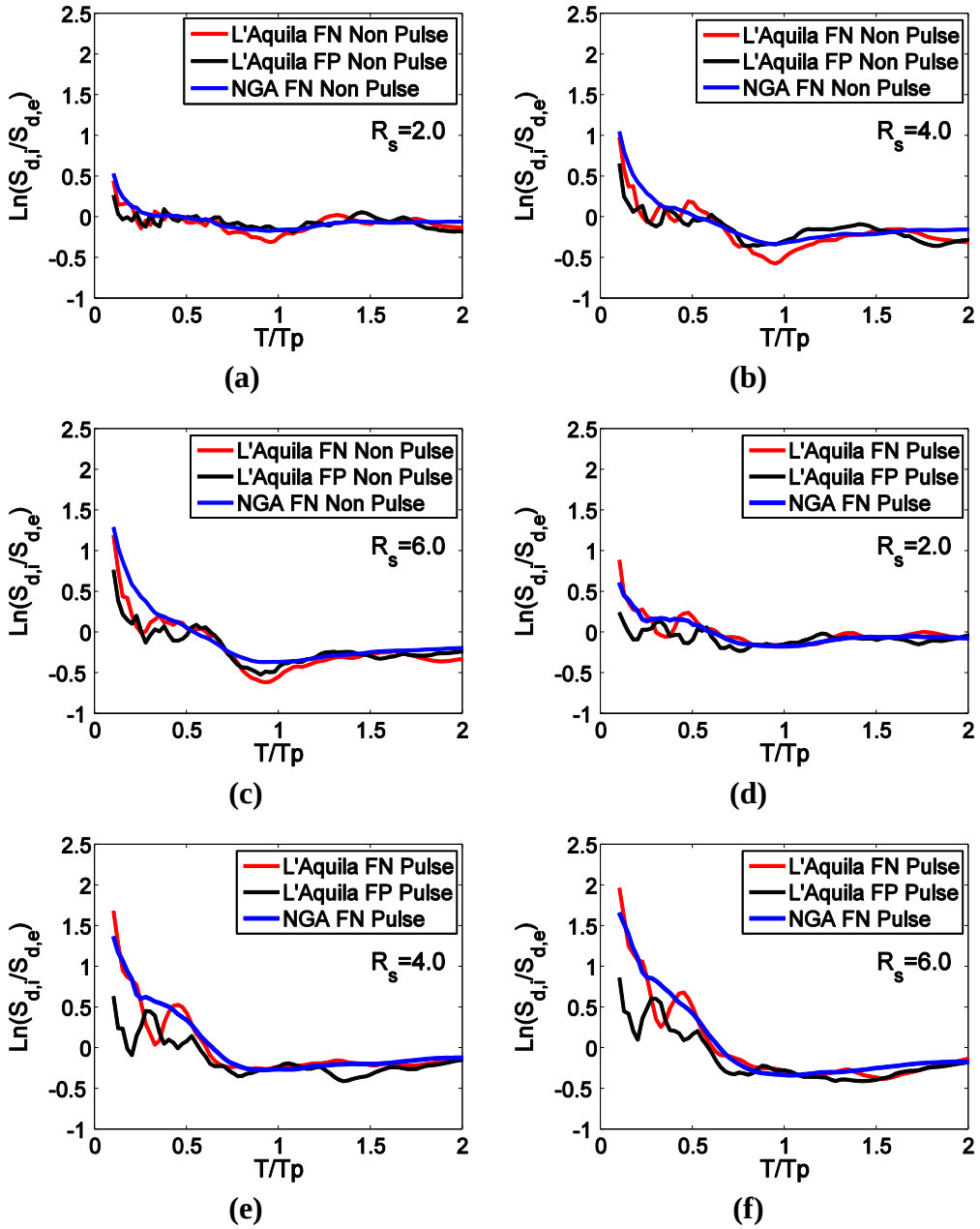

***Figure 4.8**. a, b and c - Inelastic to elastic displacement demand ratio for R_s = 2, 4 and 6 for non-pulse-like stations; d, e and f - Inelastic to elastic displacement demand ratio for R_s = 2, 4 and 6 for pulse-like ground motions.*

As done for the NGA records, ε values were calculated for pulse-like and non-pulse-like L'Aquila FN components with respect to a ground motion prediction equation (GMPE), that is, the Sabetta and Pugliese (1996), which is built on the largest horizontal component of Italian strong-motion data. The GMPE was preliminarily modified to remove the event bias on the mean. To this aim, a factor, $\alpha(T)$ was added to the GMPE[16]:

$$\overline{\log_{10}\left(S_{a,e}(T)\right)} = a + b\cdot M + c\cdot \log_{10}\left(R_{epi}^2 + h^2\right)^{1/2} + e_1\cdot S_1 + e_2\cdot S_2 + \alpha(T) \qquad (3)$$

where $\overline{\log_{10}\left(S_{a,e}(T)\right)}$ is the value of spectral acceleration obtained by the modified attenuation relationship; a, b, c, h, e_1, e_2, are the coefficients of the original attenuation relationship which depend on T and allow to account for magnitude (M), epicentral distance (R_{epi}), and site conditions and are equal to 1 for shallow and deep alluvium sites, respectively, and 0 otherwise; and $\alpha(T)$ is given in Eq. 4 being computed using only of the spectral acceleration values of the FN components of near-source ground motions classified as non-pulse-like (i.e., those supposed to be ordinary).

$$\alpha(T) = \frac{1}{6}\sum_{i=1}^{6}\log_{10}\left(S_{a,e}(T)\right)_i - \left(a + b\cdot M + c\cdot \log_{10}\left(R_{epi}^2 + h^2\right)^{1/2} + e_1\cdot S_1 + e_2\cdot S_2\right)_i \qquad (4)$$

The intra-event standard deviation $\sigma(T)$ (base 10 logarithms) also was estimated as the standard deviation of the residuals of non-pulse-like FN components within 30 km. Numerical values of α and σ are reported in Table 4.5 for each oscillation period T.

[16] In the application of the attenuation relationship (Sabetta and Pugliese, 1996), the surface wave magnitude (M_s) value of the L'Aquila earthquake is assumed to be the same as the M_w value.

Table 4.5 *Values of* $\alpha(T)$ *and* $\sigma(T)$ *for each period*

T (sec)	α	σ
0	-0.4	0.3
0.04	-0.4	0.4
0.07	-0.4	0.4
0.1	-0.4	0.3
0.15	-0.5	0.3
0.2	-0.4	0.3
0.3	-0.5	0.3
0.4	-0.4	0.2
0.5	-0.4	0.2
0.75	-0.4	0.2
1	-0.3	0.2
1.5	-0.3	0.5
2	-0.3	0.3
3.03	-0.3	0.4
4	-0.1	0.4

Figure 4.9a shows average ε values, computed after modification, for FN and FP components of pulse-like ground motions. In the same figure, ε values of average non rotated (N-S and E-W) horizontal components of the stations which have recorded pulses are also reported. As shown for the NGA data, rotated and non rotated ε have the same shape, with the non rotated values in an intermediate position between FN and FP values. It has to be highlighted that ε values of non rotated and FP records were computed with the attenuation law modified with respect to FN components of non-pulse-like ground motions and using the estimated $\sigma(T)$ values. In Figure 4.9b, the ε values of FN components of pulse-like records are given considering the modification for accounting for the peculiar spectral shape of pulse-like records presented in Eq. 2 of Chapter 3; i.e., Equation (5). In the same figure also ε values of FN components of non-pulse-like records are reported (in this latter case ε is computed only with the modification of the GMPE according to Eq. 3).

$$\overline{\overline{\ln\left(S_{a,S\&P}(T)\right)}} = \left(\log_{10}(e)\right)^{-1} \cdot \overline{\log_{10}\left(S_{a,e}(T)\right)} + e^{-\left(\ln\left(T/T_p\right)\right)^2} \quad (5)$$

Because, the Sabetta and Pugliese relationship is not valid for T larger than 4s, the ε values for all records with Tp larger 1 sec cannot be represented entirely in the 0÷4 T/Tp range, this is why the plot in Figure 4.9 has unexpected trend for high T over Tp ratio; i.e., the average plotted corresponds to a single record.

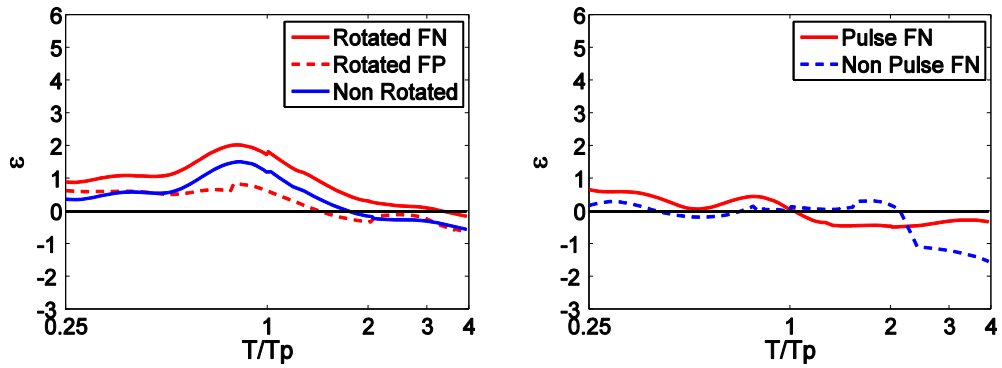

(a) **(b)**

Figure 4.9*.. (a) Average ε values of L'Aquila pulse-like records; (b) Average ε values for FN components of L'Aquila pulse-like and non-pulse-like records with modified attenuation relationship.*

4.4 Un-Rotated Records

In accordance with all models used and suggested by literature, only horizontal FN- and FP-rotated components were analyzed so far. Similar analysis of the un-rotated components seems to confirm that the rupture directivity effects have to be studied in FN and FP components as:

1. In the case of pulse-like signals, FN direction has seismic displacement demand higher than the other two un-rotated components. Conversely,

the FP direction identifies the lowest seismic demand. This is briefly shown in Figure 4.10a where the means of the logarithms of rotated over un-rotated (N-S and E-W) spectral ratios for pulse-like ground motions are given. In the 0 sec to 3.0 sec interval, FN to EW and FN to NS average ratios are respectively equal to 1.12 and 1.32 respectively. Similarly FP to EW and FP to NS have average values of 0.80 and 0.91, respectively. Conversely, if non-pulse-like stations are analyzed, rotation does not affect the results, this is shown by Figure 4.10b. Same average values are reported for non-pulse-like stations, in this case the ratios are equal to 1.17 and 1.10 (FN/EW and FN/NS) or 1.05 and 0.89 (SP/EW and FP/NS). Similar results were observed by means of ε for NGA records in Section 3.2.1;

2. Processing un-rotated signals, pulses were found in both in N-S and E-W directions in an apparently non-systematical way. More specifically, 5 signals in E-W direction and 4 signals in N-S directions were classified as pulses. Components of CLN recording were both classified as pulses.

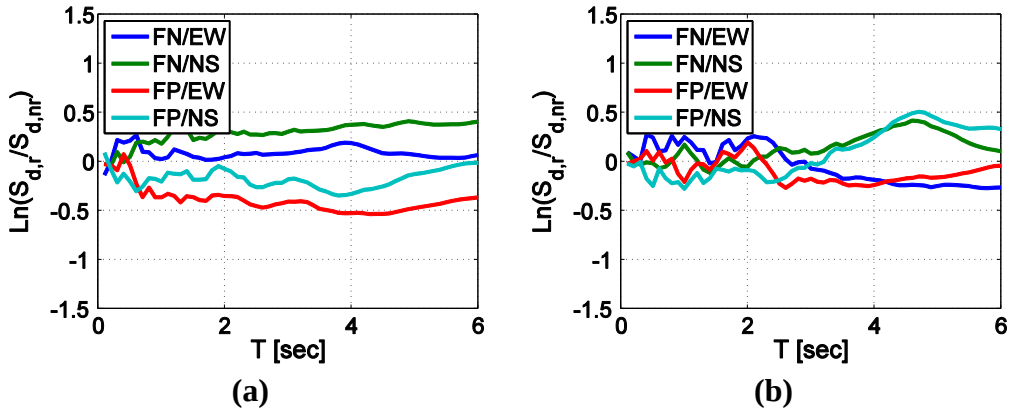

***Figure 4.10**.. Rotated and non rotated elastic spectral displacement ratios for pulse-like (a) and non-pulse-like records (b).*

4.5 Rupture-normal direction and vertical component

Finally, as suggested by (Somerville, 2005), the horizontal strike-normal ground motion component was considered and analyzed as the fault-normal component. Strictly respecting the rupture geometry, the fault-normal direction is not horizontal for dip-slip earthquakes (see Figure 3.1b of previous chapter), while it requires spatial rotation of the records, although authors were not able to find other studies addressing this same issue. Therefore, horizontal strike-normal rotated components were again rotated (including the vertical component) to obtain rigorous rupture-normal (RN) and rupture-parallel (RP) signals. However, analyzing the so-rotated records, Table 4.6, the picture is not as clear as in the case of strike-normal and strike-parallel rotation. In fact, pulse-like signals were identified both in RN and RP directions; i.e., 8 pulse-like signals are identified (reported in bold): 4 in RP and 4 in RN direction.

Table 4.6 Results of signals analyses for rupture-normal and rupture-parallel components.

Component	Pulse indicator	Late pulse indicator	PGV [cm/sec]	Classified as Pulse	Tp [sec]
AQV_RN	0.06	0.00	29.40	NO	0.55
AQV_RP	**1.00**	**0.00**	**26.62**	**YES**	**0.53**
AQG_RN	**1.00**	**0.00**	**31.89**	**YES**	**0.96**
AQG_RP	**0.93**	**0.00**	**16.67**	**YES**	**1.11**
AQA_RN	0.75	0.00	26.10	NO	1.11
AQA_RP	0.03	0.00	15.34	NO	1.74
AQK_RN	**1.00**	**0.00**	**42.33**	**YES**	**1.88**
AQK_RP	0.00	1.00	23.52	NO	1.70
GSA_RN	0.13	0.00	7.89	NO	3.02
GSA_RP	0.65	0.00	8.43	NO	3.28
CLN_RN	0.01	1.00	4.16	NO	5.40
CLN_RP	**1.00**	**0.00**	**6.83**	**YES**	**1.97**
AVZ_RN	0.94	1.00	11.45	NO	1.90
AVZ_RP	0.28	1.00	6.62	NO	1.65
MTR_RN	0.04	1.00	3.76	NO	2.98

MTR_RP	0.00	0.00	3.21	NO	3.06
GSG_RN	**0.99**	**0.00**	**4.13**	**YES**	**3.72**
GSG_RP	**1.00**	**0.00**	**2.85**	**YES**	**3.66**
FMG_RN	0.00	1.00	1.97	NO	3.44
FMG_RP	0.00	1.00	1.94	NO	1.59
ANT_RN	0.00	1.00	1.98	NO	2.32
ANT_RP	0.00	0.00	1.84	NO	0.92
CSO_RN	0.00	1.00	1.79	NO	5.51
CSO_RP	0.97	1.00	2.74	NO	3.97
ORC_RN	**0.98**	**0.00**	**7.01**	**YES**	**0.847**
ORC_RP	0.00	1.00	2.42	NO	4.746

Vertical components were also analyzed alone. Of the thirteen stations considered, the algorithm identifies only one vertical signal as pulse-like (CLN). To complete the study of vertical signals, average ε values were calculated for stations with pulse-like horizontal signals. In other words, also in this case the Sabetta and Pugliese (1996) GMPE was modified to account for the average effect of the earthquake. In analogy with the horizontal case, stations without pulses (in the horizontal direction) were used to compute the vertical modification factor $\alpha(T)$. Results are plotted in Figure 4.11 showing that here is no significant trend and the absence of pulse-like effects seems to be confirmed.

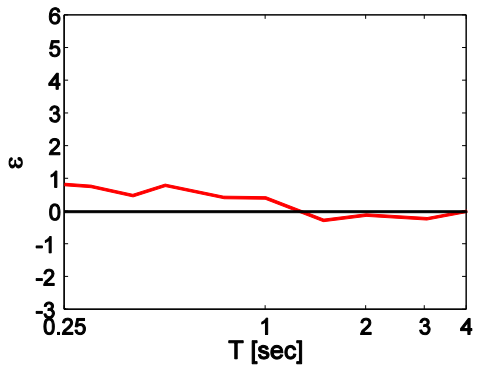

Figure 4.11.. *Average e values of vertical signals components of pulse-like stations.*

4.6 Conclusions

Although the directivity-induced pulses problem is known since many years, a quantification of its significance for structural engineering and recognition of its occurrence in observed earthquakes is not well established yet. In this chapter, some recent tools to investigate pulse-like records were applied in order to investigate near-source effects in the recent April 6th 2009 L'Aquila earthquake. Results of the analyses on the NGA database, presented in the previous chapter, were used here as a benchmark.

Horizontal strike-rotated records from the mainshock were analyzed. Extracted pulses and seismic demand of signals identified as pulse-like agree with the NGA results and seems to suggest that directivity effects occurred and that non-ordinary seismic demand affected near-source structures.

A few side results were also found. In fact, the fault parallel components of pulse-like stations were found to have an inelastic-to-elastic displacement ratio not completely similar to that of ordinary records. Moreover, an analysis which includes the vertical components of motion did not provide clear evidence of directivity effects in the rupture-normal direction.

As a final conclusion, now that attempts to modify probabilistic seismic hazard analysis to account for near-source effects are close to succeed, these results show also that specific modification to inelastic demand in regions close to faults should be taken into account in structural design procedures.

References

Abrahamson, N. A., Somerville, P. G. (1996) Effects of the Hanging Wall and Footwall on Ground Motions Recorded During the Northridge Earthquake, Bull. Seism. Soc. Am., 86(1b), S93-S99.

Akkar, S., Bommer, J. J. (2006) Influence of long-period filter cut-off on elastic spectral displacements. Earthquake Eng. Struct. Dyn., 35(9), 1145–1165.

Ameri, G., Massa, M., Bindi, D., D'Alema, E., Gorini, A., Luzi, L., Marzorati, S., Pacor, F., Paolucci, R., Puglia, R., Smerzini, C. (2009), The 6 April 2009, Mw 6.3, L'Aquila (Central Italy) earthquake: strong-motion observations, Seism. Res. Lett. (in press).

Baker, J. W. (2007) Quantitative Classification of Near-Fault Ground Motions Using Wavelet Analysis, Bull. Seism. Soc. Am., 97(5), 1486-1501.

CEN, European Committee for Standardisation (2003) Eurocode 8: design provisions for earthquake resistance of structures, Part 1.1: general rules, seismic actions and rules for buildings, prEN 1998-1.

Chioccarelli, E., De Luca, F., Iervolino, I. (2009) Preliminary Study of L'Aquila Earthquake Ground Motion Records. [Available at http://www.reluis.it/doc/pdf/Aquila/Peak_Parameters_L_Aquila_Mainshock_V5.2.pdf]

Cosenza, E., Manfredi, G., Ramasco, R. (1993) The Use of Damage Functionls in Earthquake Engineering: A Comparison between Different Methods. Earthquake Eng. Struct. Dyn., 22(10), 855-868.

Hancock, J., Bommer, J. J. (2006) A State-of-Knowledge Review of the Influence of Strong-Motion Duration on Structural Damage, Earthquake Spectra, 22(3), 827-845.

Iervolino, I., Cornell, C. A. (2008) Probability of Occurrence of Velocity Pulses in Near-Source Ground Motions, Bull. Seism. Soc. Am., 98(5), 2262-2277.

Paolucci, R. (2009) Long-Period Earthquake Ground Motion: Recent Advances and Observations from the April 6 2009, Mw 6.3 L'Aquila Earthquake, Italy, Proceeding of Aces Workshop on Performance-Based Earthquake Engineering Corfù, Greece.

Sabetta, F., Pugliese, A. (1996) Estimation of Response Spectra and Simulations of Nonstationary Earthquake ground Motion, Bull. Seism. Soc. Am., 86(2), 337-352.

Somerville, P. G. (2003) Magnitude Scaling of the Near Fault Rupture Directivity Pulse, Physics of the Earth and Planetary Interiors, 137, 201-212.

Somerville, P. G. (2005) Engineering Characterization of Near-Fault Ground Motions, Proceeding of 2005 NZSEE Conference, Wairakei, NZ.

Somerville, P. G., Smith, N. F., Graves, R.W., Abrahamson, N. A. (1997) Modification of Empirical Strong Motion Attenuation Relations to Include the Amplitude and Duration Effect of Rupture Directivity, Seism. Res. Lett., 68(1), 199-122.

Verderame, G. M., Iervolino, I., Ricci, P. (2009) Report on the Damages on Buildings Followings the Seismic Event of 6th of April. [Available at http://www.reluis.it/doc/pdf/Aquila/Rapporto_fotografico_V1.2.pdf]

CHAPTER 5.
PROBABILISTIC SEISMIC HAZARD ANALYSIS FOR NEAR SOURCE SITES

5.1 Introduction

Rupture directivity effects in ground motion consist in the fact that in sites in a particular geometrical configuration with respect to the rupture, the velocity fault-normal signals may show a large pulse which occurs at the beginning of the record and contains the most of energy. A simple case of rupture directivity, in the case of unilateral strike slip fault, is reported in Fig. 5.1, in which the rupture is represented as a point source moving along the fault. If site 2 is reached at the same time by many seismic waves originated in different instants, the signal there recorded may feature a low frequency full cycle velocity pulse. Conversely, in site 1, with respect to which the rupture moves away, waves radiated in different instants tend also to arrive in different moments and the energy is spread over a larger amount of time and in an lower amplitude signal.

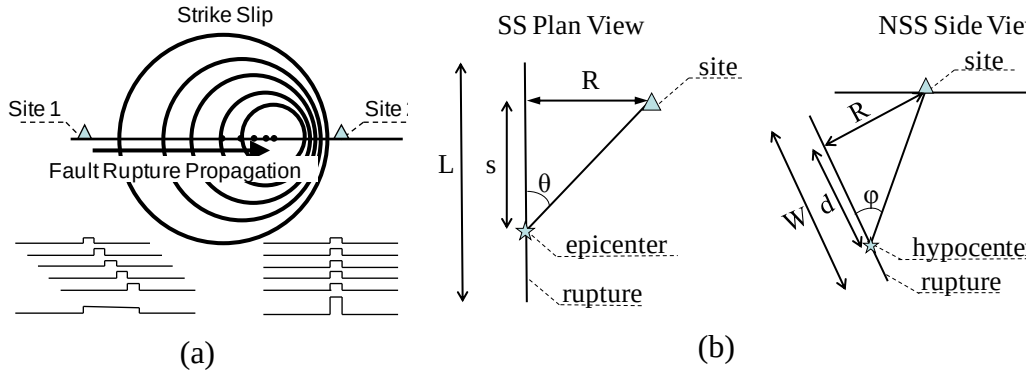

Figure 5.1*. Constructive interference of waves and directivity (a) and schematic view of directivity conditions (b) for strike slip (SS) and non-strike-slip (NSS) faults, adapted from (Somerville et al. ,1997 and Iervolino and Cornell, 2008).*

In Chapter 3, main characteristics of pulse-like signals were shown analyzing the Next Generation Attenuation database (NGA) with the Baker's (2007) procedure to identify pulse-like and non-pulse-like records. Three different aspects have been identified and they are reported briefly here: (1) the elastic demand of pulse-like signals is generally stronger than ordinary signals, particularly in the fault-normal direction; (2) the spectral shape is non-standard, showing an increment of spectral ordinates around the pulse period (Fig. 5.2a); (3) because the pulse period is generally in the low frequency range (i.e., close to that of the most common structures), the inelastic demand may be particularly high on one side, and, on the other side, it may develop in a shorter time compared to the ordinary case (Tothong and Luco, 2007). The latter condition has been demonstrated using an inelastic SDoF system with a strength reduction factor (Rs ratio between maximum elastic and inelastic force) equal to 6 (Fig. 5.2b) and is of crucial importance from an engineering point of view. As mentioned in Chapter 3, the issue is a consequence of the peculiar spectral shape of pulse-like records.

Characteristics of pulse-like records have also been analyzed in the recent L'Aquila earthquake (Chapter 4) and, in this chapter, the issue of accounting for directivity in probabilistic seismic hazard analysis (PSHA) is analyzed and some numerical examples are shown. Additional aim of the

chapter is to make a first proposal of an easy and applicable procedure to account for pulse-like effects in ordinary definition of seismic input.

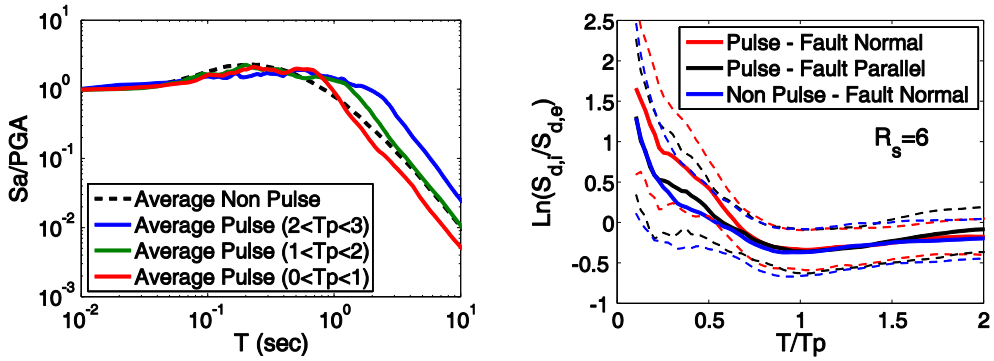

Figure 5.2 *Elastic acceleration spectra (a) and inelastic to elastic displacement ratios (b) for near-source records*

5.2 Near-Source PSHA

Rupture and propagation of waves in actual earthquakes are very complex, and directivity is not always observed. Moreover, directivity may also occur at sites apparently not prone to pulse-like ground motion. On the other hand, for the reasons discussed in the previous section, directivity is of interest for earthquake resistant design. It is clear that is not possible to apply the current earthquake engineering practice to the near source, and procedure have to be reviewed and adjusted consistently. A rational approach to seismic risk analysis requires a probabilistic model of the occurrence of directivity effects in ground motions. The systematic deviation of pulse-like signals with respect to the ordinary imply that, in the probabilistic assessment of structures, a pulse occurrence model is required to incorporate such effects accurately in the PSHA. The phenomena should be reflected in record selection, because the latter should be related with the disaggregation of seismic hazard (Cornell, 2004). This issue has been analyzed by Thotong et al. (2007) and Iervolino and

Cornell (2008). Both papers propose a modification of the hazard integral used in ordinary PSHA including directivity effects but only to date all the necessary probabilistic models are available. So in this chapter, before analyzing the complete expression of the integral, all the included models will be presented in order to provide a final and directly applicable version of the hazard integral.

5.2.1 Background models

New PSHA requires dealing with three tasks which are not faced in traditional hazard analysis: (i) pulse occurrence probability; (ii) pulse period (Tp) prediction; and (iii) pulse amplitude prediction.

Models for the prediction of the pulse occurrence probability, $P[pulse]$, was developed by Iervolino and Cornel (2008) and provide a probability contour in near-source zones. Models depend only on geometrical parameters (the depicted in Fig.5.1b from Somerville et al.,1997) which are slightly different in the case of strike-slip (SS) or non-strike-slip (NSS) faults. The SS equation is reported below and application limits are [5, 30 km], [0, 40km] and [0, 90°] respectively for R, s and θ.

$$P[pulse|R,s,\theta] = \frac{e^{0.859-0.111R+0.0187s-0.044\theta}}{1+e^{0.859-0.111R+0.0187s-0.044\theta}} \quad (1)$$

Because of dependency of the model on geometrical conditions, it is necessary to know position and dimensions of the rupture. These information are provided by Wells and Coppersmith (1994) relationship as event's magnitude functions.

Regarding pulse period, many authors show that Tp (expressed in seconds) has a lognormal distribution and depends only on the event magnitude. Equation reported by Chioccarelli and Iervolino (2010) is reported in here (standard deviation equal to 0.59).

$$\ln Tp = -6.19 + 1.07 \cdot M_W \tag{2}$$

Finally Baker (2008) proposed a modification factor for the existing Boore and Atkinson (2008) ground motion prediction equation (GMPE) to account for the amplitude increment of spectral elastic accelerations if the pulse occurs. A similar one is considered herein:

$$\overline{\ln\left(S_{a,e}(T)\right)} = \ln\left(S_{a,e}(T)\right) + e^{-\left(\ln\left(T/Tp\right)\right)^2} \tag{3}$$

where $\ln\left(S_{a,e}(T)\right)$ is the original GMPE, $\overline{\ln\left(S_{a,e}(T)\right)}$ is the log of the predicted acceleration via the modified GMPE, and the second term $\left(e^{-\left(\ln\left(T/Tp\right)\right)^2}\right)$ models the bump of spectral ordinates with a maximum at T = Tp.

Modification factor has been fitted by Baker on a set of records from the Next Generation Attenuation (NGA) database classified as pulse-like or non-pulse-like. Starting from a set of records slightly different used in Chioccarelli and Iervolino (2010), a preliminary application of this factor is provided here. In particular, pulse-like records, grouped in bins of pulse period Tp (as in Fig. 5.2a), have been compared with spectra computed by Boore and Atikinson GMPE modified with the Baker's factor. Given the seismologic characteristics of each pulse-like record, the median response spectrum from GMPE has been computed and the average of each group of Tp is shown in Fig. 5.3a, b and c. It is worth to note that, conversely to Fig. 5.2, spectra in Fig. 5.3 are dimensional because they are not divided by PGA of each records. In this way it seems that bumps due to directivity affect an higher range of periods than what suggested by Fig. 5.2a and modification of GMPE, although narrow band, influences on a significant portion of the spectra. For the same groups of NGA records, ε values have been calculated using the modified GMPE and average values of each bin of Tp are reported in Fig 5.3d. An analyses of the structural response

is necessary in order to clarify which part of the bump is the cause of the unexpected behavior shown by Fig. 5.2b.

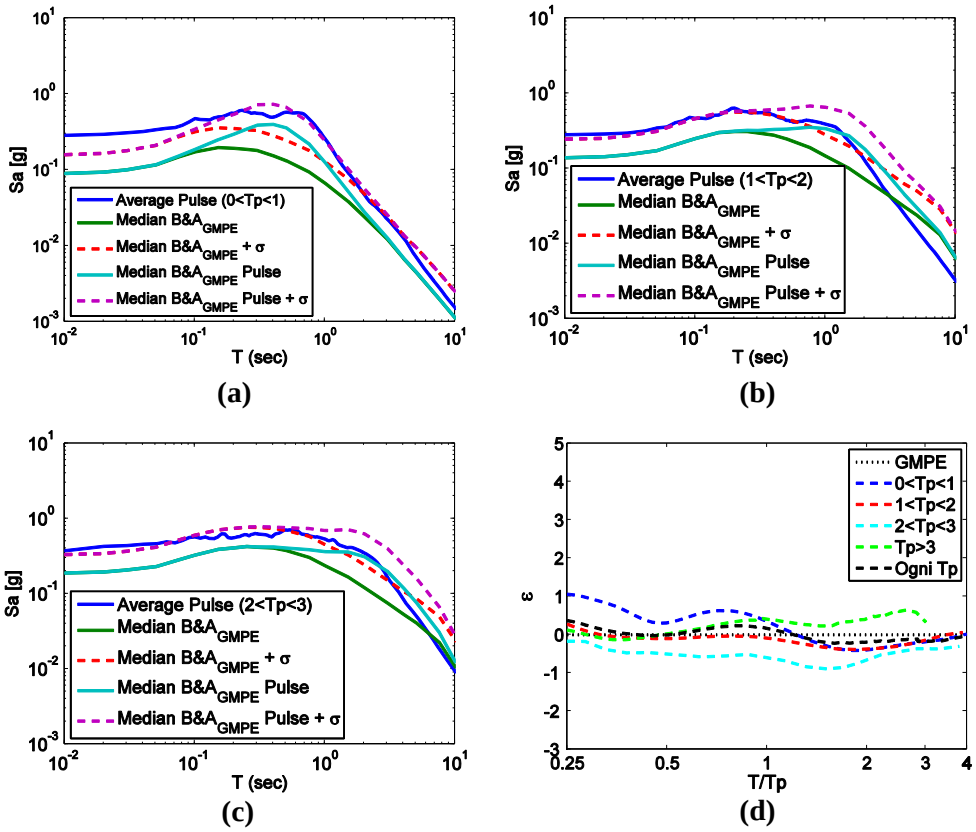

Figure 5.3*. Preliminary application of amplification factor for pulse-like records grouped for Tp between 0 and 1.0 sec(a), 1.0 and 2.0 sec(b) and 2.0 and 3.0 sec(c) and ε computed using the modified GMPE(d)*

Rigorously modification factor cannot be applied to a GMPE different from that one used as fitting but a first application of the factor on Sabetta and Pugliese (1996) GMPE has already been provided analyzing records from L'Aquila earthquakes (Chapter 4). Results suggest that, at least as first approximations, errors are negligible and a combination of Baker's factor and Sabetta and Pugliese attenuation relationship will be presented also in the following.

5.2.1 Hazard integral for near-source conditions

As mentioned, it would be desirable to modify the PSHA to incorporate directivity effects in a hazard analysis. In order to clarify the effort needed and outline the differences for the pulse-like PSHA with the conventional PSHA (Cornell 1968, Reiter 1990), Eq. 4 shows the standard approach for computing the mean annual frequency (MAF, λ_{Sa}) of exceeding a ground motion parameter level, e.g., elastic spectral acceleration (S_a) exceeding an intensity level x:

$$\lambda_{Sa}(x) = \sum_{i=1}^{N.fault} \nu_i \int_{m,r} G_{Sa|M,R}(x|m,r) \cdot f_{M,R}(m,r) \cdot dm \cdot dr \tag{4}$$

where ν_i is the mean annual rate of occurrence of earthquakes on fault *i* above a minimum threshold magnitude. Uppercase denotes random variables, and lowercase indicates realizations of those random variables throughout this chapter. *M* is the magnitude and *R* is the source-to-site distance, $f_{M,R}$ is the joint probability density function (PDF) of *M* and *R* on fault *i* and G_{Sa} is the complementary cumulative distribution function (CCDF) of the lognormal random variable *Sa* computed using a defined GMPE.

The near-source hazard is a linear combination of two hazard curve weighted by the pulse occurrence probability (Iervolino and Cornell, 2008). The hazard contribution given the occurrence or the absence of the pulse are reported, in Eq. 5, as $\lambda_{Sa,Pulse}$ and $\lambda_{Sa,NoPulse}$.

$$\lambda_{Sa}(x) = \lambda_{Sa,Pulse}(x) + \lambda_{Sa,NoPulse}(x) \tag{5}$$

These two terms are expanded in Eq. 6 and 7 starting from the expressions available in literature and considering, for this particular case, strike-slip rupture

[1] and individual fault. These two hypothesis will be respected in all the following examples.

$$\lambda_{Sa,Pulse}(x) = \nu \cdot \int_m \int_l \int_p \int_{t_p} \int_e P\left[Pulse|l,p,e\right] \cdot G_{Sa,\mathrm{mod}|Pulse,M,L,P,T_p}\left(x|m,l,p,t_p\right) \times \\ \times f_{T_p|M} \cdot f_{L,E|M,P} \cdot f_{M,P} \cdot dt_p \cdot dl \cdot dp \cdot dm \cdot de \quad (6)$$

$$\lambda_{Sa,NoPulse}(x) = \nu \cdot \int_m \int_l \int_p \int_e \left(1 - P\left[Pulse|l,p,e\right]\right) \cdot G_{Sa|M,L,P}\left(x|m,l,p\right) \times \cdot \\ \times f_{L,E|M,P} \cdot f_{M,P} \cdot dl \cdot dp \cdot dm \cdot de \quad (7)$$

L and P represent the rupture length and its position on the fault, respectively; E is the epicenter location on the fault (usually assumed uniformly distributed); G_{Sa} is the original ground motion attenuation prediction equation; $G_{Sa,\mathrm{mod}}$ is the attenuation relationship modified to account for pulse-like spectral shape. Eq 6 and 7 show the variables used in a practical solution procedure. Knowing them, all the other geometrical parameters used for the pulse occurrence prediction model (R, s and θ) and for the GMPE (R_{jb}) can be deterministically calculated because the relative rupture-site position is defined. It is to note that, because used GMPE is function of R_{jb}, G_{Sa} and $G_{Sa,\mathrm{mod}}$ are independent from the epicenter position on the rupture.

In order to better explain the relationship between the ordinary and the near-source hazard integral, starting from Eq. 4, Eq. 9 can be obtained applying the total probability theorem :

$$\lambda_{Sa}(x) = P\left(IM > IM_0\right) = \nu \cdot \left(1 - F\left(IM_0|Pulse\right)\right) \cdot P\left(Pulse\right) + \\ + \nu \cdot \left(1 - F\left(IM_0|NoPulse\right)\right) \cdot P\left(NoPulse\right) \quad (9)$$

[1] This hypothesis allows to refer only to a plan view and the rupture is represented as a simple line (see Figure 5.1b). Hypocentral position and rupture area do not influence the problem; significant geometrical parameters are rupture length and epicenter position.

Relationship between Eq. 5 and 9 is apparent assuming $\lambda_{Sa,Pulse} = \nu \cdot \left(1 - F\left(IM_0 \middle| Pulse\right)\right) \cdot P\left(Pulse\right)$ and $\lambda_{Sa,NoPulse} = \nu \cdot \left(1 - F\left(IM_0 \middle| NoPulse\right)\right) \cdot P\left(NoPulse\right)$. Total probability theorem can be applied again conditioning to all the variable of the problem (Eq. 10).

$$\begin{aligned} \frac{\lambda_{Sa}(x)}{\nu} &= \int_{tp}\int_{m}\int_{l}\int_{p}\int_{e}\left[1 - F\left(IM_0 \middle| Pulse, t_p, m, l, p, e\right)\right]\times \\ &\times f\left(Pulse, t_p, m, l, p, e\right)\cdot dt_p \cdot dm \cdot dl \cdot dp \cdot de + \\ &+ \int_{m}\int_{l}\int_{p}\int_{e}\left[1 - F\left(IM_0 \middle| NoPulse, m, l, p, e\right)\right]\times \\ &\times f\left(NoPulse, m, l, p, e\right)\cdot dl \cdot dm \cdot dp \cdot de \end{aligned} \tag{10}$$

Recalling that $f(x,y) = f\left(x \middle| y\right)\cdot f\left(y\right)$, Eq. 10 can be modified as reported in Eq. 11:

$$\begin{aligned} \frac{\lambda_{Sa}(x)}{\nu} &= \int_{tp}\int_{m}\int_{l}\int_{p}\int_{e}\left[1 - F\left(IM_0 \middle| Pulse, t_p, m, l, p, e\right)\right]\times \\ &\times P\left(Pulse \middle| t_p, m, l, p, e\right)\cdot f\left(t_p \middle| m, l, p, e\right)\cdot f\left(p, e \middle| m, l\right)\cdot f\left(l \middle| m\right)\cdot f\left(m\right)\times \\ &\times dt_p \cdot dl \cdot dp \cdot dm \cdot de + \\ &+ \int_{m}\int_{l}\int_{p}\int_{e}\left[1 - F\left(IM_0 \middle| NoPulse, m, l, p, e\right)\right]\cdot P\left(NoPulse \middle| m, l, p, e\right)\times \\ &\times f\left(p, e \middle| m, l\right)\cdot f\left(l \middle| m\right)\cdot f\left(m\right)\cdot dl \cdot dp \cdot dm \cdot de \end{aligned} \tag{11}$$

Finally, recalling expressions of the analytical models reported above and considering some geometric conditions, real stochastic dependency can be indentified and redundant dependencies can be removed. More specifically:

- pulse probability is function of geometric parameters and is independent from magnitude and pulse period $P\left(Pulse\middle|t_p,m,l,p,e\right)=P\left(Pulse\middle|l,p,e\right)$;
- pulse period distribution is function of magnitude only $f\left(t_p\middle|m,l,p,e\right)=f\left(t_p\middle|m\right)$;
- distribution of rupture position and epicenter's position on the rupture is function of the rupture length (which is function of event magnitude by Wells and Coppersmith relationship, 1994) $f\left(p,e\middle|m,l\right)=f\left(p,e\middle|l\right)$. See also Section 5.3 for further details.

Thus Equation 11 becomes:

$$\begin{aligned}\frac{\lambda_{Sa}(x)}{\nu}&=\int_{tp}\int_{m}\int_{l}\int_{p}\int_{e}\left[1-F\left(IM_0\middle|Pulse,t_p,m,l,p,e\right)\right]\times\\&\times P\left(Pulse\middle|l,p,e\right)\cdot f\left(t_p\middle|m\right)\cdot f\left(p,e\middle|l\right)\cdot f\left(l\middle|m\right)\cdot f\left(m\right)\times\\&\times dt_p\cdot dl\cdot dp\cdot dm\cdot de+\\&+\int_{m}\int_{l}\int_{p}\int_{e}\left[1-F\left(IM_0\middle|NoPulse,m,l,p,e\right)\right]\cdot P\left(NoPulse\middle|l,p,e\right)\times\\&\times f\left(p,e\middle|l\right)\cdot f\left(l\middle|m\right)\cdot f\left(m\right)\cdot dl\cdot dp\cdot dm\cdot de\end{aligned}\qquad(12)$$

Moreover $1-F\left(IM_0\middle|Pulse,t_p,m,l,p,e\right)$ is the modified GMPE, and $1-F\left(IM_0\middle|NoPulse,m,l,p,e\right)$ is the ordinary GMPE; pulse occurrence and no pulse occurrence are obviously mutually exclusive events so $P\left(NoPulse\right)=1-P\left(Pulse\right)$. Considering these additional conditions, Eq. 12 is exactly equivalent to Eq. 6 and 7.

5.2.1 Disaggregation analysis for near-source conditions

In addition to the hazard analysis, another common calculation in PSHA is disaggregation (McGuire 1995, Bazzurro and Cornell 1999). Typically, this calculation is used to compute the distribution of magnitudes, distances, and epsilon values contributing to occurrence or exceedance of some ground motion intensity level. Ordinary disaggregation procedure has already been presented and applied in Chapter 2, so in this section, disaggregation equations are modified in accordance with the expressions of near-source PSHA presented above. Comparing with traditional case, additional aim is to provide the probability that a ground motion intensity level is caused by a pulse-like ground motion, and to provide the distribution of pulse periods associated with those ground motions. This disaggregations are important to structural engineers because they provide a rational basis for selecting representative ground motions (near-fault and non–near-source) to be used in dynamic analyses of a structure (Thotong et al., 2007).

Analytical expression for ordinary case presented in Chapter 2 is reported here (application of Bayes theorem):

$$f\left(m,r,\varepsilon\middle|IM>IM_0\right)=\frac{\sum_{i=1}^{N_{fault}}\nu_i I\left[IM>IM_0\middle|m,r,\varepsilon\right]\cdot f\left(m,r,\varepsilon\right)}{\lambda_{IM_0}} \tag{13}$$

Referring to the same hypotheses of the previous section (single fault and strike-slip rupture), a first way to analytically represent disaggregation results is:

$$f\left(m,l,p,e,\varepsilon\middle|IM>IM_0\right)=\frac{\nu\cdot P\left[IM>IM_0\middle|m,l,p,e,\varepsilon\right]\cdot f\left(m,l,p,e,\varepsilon\right)}{\lambda_{IM_0}} \tag{14}$$

in which $P\left[IM>IM_0\middle|m,l,p,e,\varepsilon\right]$ is the ground motion prediction equation given magnitude and all the geometrical variables of the problem and ε.

Appling the total probability theorem referring to pulse or no pulse occurrence and considering real statistical dependencies, Eq. 14 becomes:

$$f\left(m,l,p,e,\varepsilon\middle|IM>IM_0\right)= \\ \frac{\nu\cdot P\left[IM>IM_0\middle|Pulse,m,l,p,e,\varepsilon\right]\cdot P\left(Pulse\middle|l,p,e\right)\cdot f\left(m,l,p,e,\varepsilon\right)}{\lambda_{IM_0}}+ \\ +\frac{\nu\cdot I\left[IM>IM_0\middle|NoPulse,m,l,p,e,\varepsilon\right]\cdot P\left(NoPulse\middle|l,p,e\right)\cdot f\left(m,l,p,e,\varepsilon\right)}{\lambda_{IM_0}} \tag{15}$$

in which I is an indicator function that equals 1 if IM is larger than IM_0 and zero otherwise. Eq. 15 means that, chosen the threshold of IM (obtained from the hazard analysis and identified as IM_0), e.g. elastic spectral acceleration for a fixed vibration period ($Sa(T_0)$), disaggregation results is a joint probability function of six variables and it can be obtained performing two disaggregation analyses respectively in the hypothesis of pulse occurrence and no pulse occurrence. Final result is the sum of two partial results weighted by the pulse occurrence probability and its complementary. It is worth to note that in order to compute first term of Eq. 15, total probability theorem has to be applied again introducing the new conditional variable Tp and obtaining Eq. 16.

$$f\left(m,l,p,e,\varepsilon\middle|IM>IM_0\right)= \\ \frac{\nu\cdot\int_{t_p} I\left[IM>IM_0\middle|Pulse,t_p,m,l,p,e,\varepsilon\right]\cdot P\left(Pulse\middle|l,p,e\right)\cdot f\left(t_p,m,l,p,e,\varepsilon\right)\cdot dt_p}{\lambda_{IM_0}}+ \\ +\frac{\nu\cdot I\left[IM>IM_0\middle|NoPulse,m,l,p,e,\varepsilon\right]\cdot P\left(NoPulse\middle|l,p,e\right)\cdot f\left(m,l,p,e,\varepsilon\right)}{\lambda_{IM_0}} \tag{16}$$

Considering only the case of pulse occurrence, joint disaggregation distribution of magnitude M and pulse period Tp can be obtained[2].

$$f\left(m,t_p\middle|IM>IM_0,Pulse\right)=\frac{\nu\cdot P\left(IM>IM_0\middle|m,t_p,Pulse\right)\cdot f\left(m,t_p\middle|Pulse\right)}{\lambda_{IM_0|Pulse}} \quad (17)$$

For numerical computation of Eq. 17, total probability theorem has to be applied again.

The rate of exceedance of IM_0 by non-pulse-like ground motions $\left(\lambda_{Sa,NoPulse}\right)$ or by pulse-like ground motions $\left(\lambda_{Sa,Pulse}\right)$ can also be calculated. These terms are complementary and analytical expression of the latter is reported in Eq. 18:

$$f\left(Pulse\middle|IM>IM_0\right)=\frac{\nu\cdot f\left(IM>IM_0\middle|Pulse\right)\cdot f\left(Pulse\right)}{\lambda_{IM_0}} \quad (18)$$

In the following some numerical applications of PSHA and disaggregation in near-source conditions are presented and compared with ordinary results.

5.3 Illustrative applications: geometrical condition and numerical algorithm

In order to study directivity influence on ground motion intensity measures, some PSHA and disaggregation analyses have been conducted.

[2] Disaggregation on M and Tp can also be applied to the unconditioned hazard value $f\left(m,t_p\middle|IM>IM_0\right)$ but because distribution of Tp is obtained in the hypothesis of pulse occurrence, the contribution of non-pulse term is automatically zero $f\left(m,t_p\middle|NoPulse\right)=0$. So $f\left(m,t_p\middle|IM>IM_0\right)=f\left(m,t_p\middle|IM>IM_0,Pulse\right)$.

Different magnitude distributions and fault dimensions have been considered in each examples but general geometric configuration has been kept constant. As already said a single fault characterized by strike-slip ruptures is considered. Moreover all the analyses are referred to a site aligned with the fault $(\theta = 0)$. This condition maximizes pulse occurrence as reported by Somerville et al. (1997) and Iervolino and Cornell (2008). The site is far five kilometers from the upper vertex of the fault (Fig. 5.4).

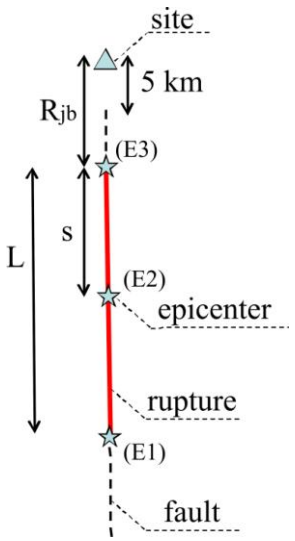

Figure 5.4. *Typical case for numerical applications; plan view.*

Referring to Fig. 5.4, some other issues have to be clarified. In each example, dimension and position of the fault are fixed (dotted line) but the rupture length (L) and rupture location (P) on the fault are variable: the first is lognormally distributed with the event magnitude (Wells and Coppersmith,1994) and the second is limited by the fault dimension and the rupture length itself. More specifically, for a given dimension, rupture can be located in all the possible positions with a uniform probability distribution but constrained by the condition of not exceeding the fault extremes. Joiner and Boore distance (R_{jb}) of the site from the fault is univocally defined once the rupture position is known. Theoretically also epicenter can be situated in all

the points of the rupture, but in order to reduce the numerical effort of the analyses, only three possible positions have been assumed: more specifically epicenter can be in one of the two rupture extremes or in the middle of the rupture. In Fig. 5.4, these positions are identified as E1, E2 and E3. Once epicenter location is defined, geometrical parameter s is known.

In all the analyses, chosen IM is the elastic spectral acceleration for all the spectral ordinates provided by the used GMPE (Sabetta and Pugliese, 1996). It means that in the considered site, the result of PSHA is the response spectrum defined in 15 points between 0sec (peak ground motion acceleration, PGA) and 4.0sec. Algorithm implemented for the numerical solution of the hazard integral consists in a series of iterative cycles "*for*" and can be synthesized in the following steps:

1) Iteration on the spectra period (T);
2) Iteration on the values of acceleration: PSHA in fact provides exceedance probability of a fixed values of IM (elastic acceleration in this case). Varying the acceleration value, it is possible to built the hazard curve for a defined spectral ordinate. Once the hazard curve is known, acceleration corresponding to a fixed exceedance probability can be identified. Repeating this process for all the spectral ordinates, a response spectrum with the same exceedance probability of all the ordinates is build. This type of spectrum is called uniform hazard spectrum (UHS) because all the spectral ordinates are characterized by the same exceedance probability and they are statistically independent. Independence of spectral ordinates is a fundamental characteristic of these procedure and the main consequence is that the shape of the computed spectrum is unrealistic for a single ground motion but it is the envelope of very different events. This issue is well known in the case of ordinary analyses but it may assume a relevant significance in near-source conditions;
3) Iteration on the magnitude (M): in some of the examples magnitude will be fixed in order to focus on the other variables of the problem.

Anyway, for the more general case, a statistical function for the definition of magnitude occurrence has to be chosen. In the last example magnitude occurrence will be defined using the Gutenberg-Richter recurrence law (Gutenberg and Richter, 1944).

4) Iteration on the rupture length (L). Rupture legth is lognormally distributed as function of the event magniude (Wells and Coppersmith, 1994). In the implementation, considered logarithms of length are included in the interval of mean plus or minus three standard deviations.
5) Iteration on the rupture position (P);
6) Iteration on the epicenter position (E): uniform probability distribution is assumed for both rupture and epicenter positions. Geometrical constrains analyzed above are considered in the implementation;
7) Computation of geometrical parameters for definition of pulse occurrence probability (R, s, θ) and for application of GMPE (R_{jb});
8) Computation of pulse occurrence probability;
9) Computation of exceedance probability of IM with the hypothesis of no pulse occurrence;
10) Iteration on Tp values: this cycle is referred to pulse-like component of the hazard only. Tp values utilized are comprised in the interval of mean plus or minus three standard deviations;
11) Computation of exceedance probability of IM with the hypothesis of pulse occurrence.

The same algorithm is represented in Fig. 5.5 for a fixed values of spectral period and IM_0.

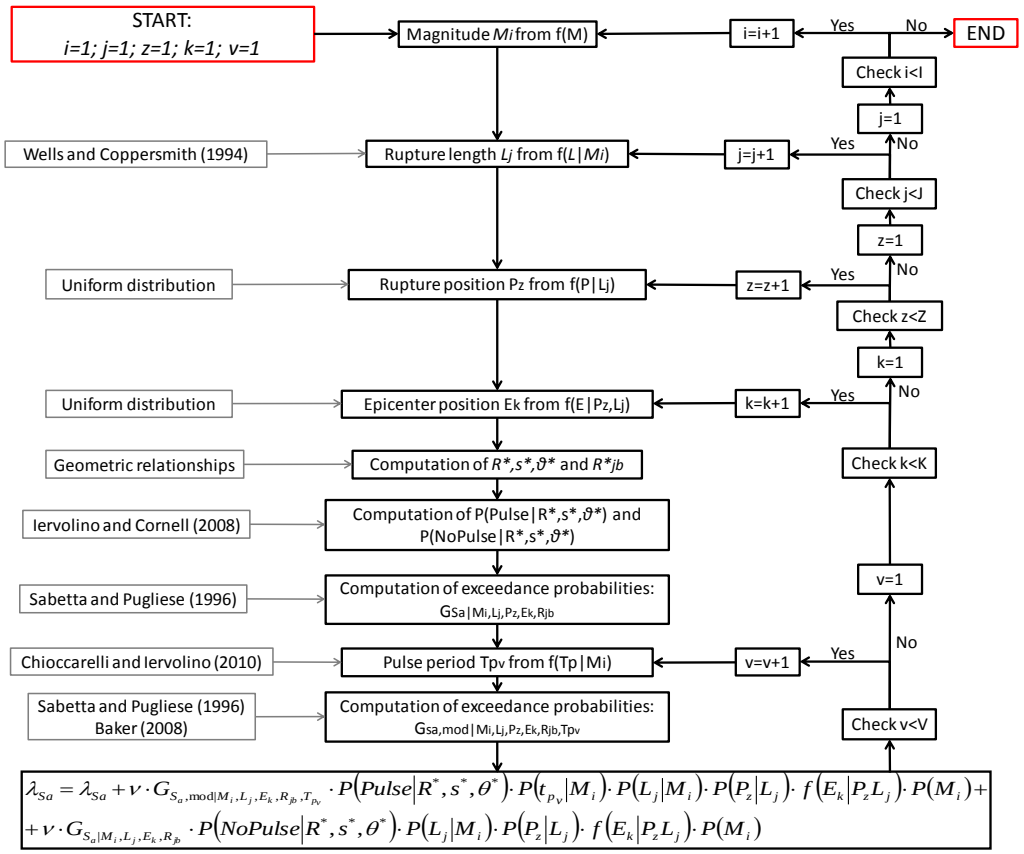

***Figure 5.5**. Flow chart for numerical solution of the hazard integral in near-source condition.*

In the algorithm in order to reduce computation effort, a preliminary analysis is performed determining a rough approximation of the hazard curve, then the same curve is recomputed with a better discretization only in the interval of acceleration close to the chosen values of exceedance probability.

Some numerical applications are presented. First two cases are characterized by a fixed values of moment magnitude (equal to 5 and 6 respectively) and limited dimension of faults. Moreover for each magnitude values, pulse period is computed accounting for standard deviation of relationship or assuming a deterministic values equal to the median of distribution. These case are performed for underlining general trends of

analyses in near-source conditions. Other two cases are presented: one with a fixed magnitude value equal to 7 and one with a discrete probability distribution defined for magnitude equal to 5, 6 and 7. In the latter two cases an higher and more realistic dimension of the fault is used.

In all the examples Sabetta and Pugliese (1996) attenuation relationship is used with fault distance (R_{jb}), being the same kind of distance used in the pulse occurrence probability model. The annual rate of earthquake occurrence on the fault is equal to 0.05 and all the analyses are referred to a return period equal to 475 years or, in other words, computed intensity measures have an exceedance probability in 50 years equal to 10% (assuming a poissonian earthquake events distribution).

5.3.1 Case 1: Magnitude equal to 5

Using a constant magnitude value, it is possible to show distribution of pulse period and rupture length[3] utilized in the numerical solution of hazard integral. (Fig. 5.6).

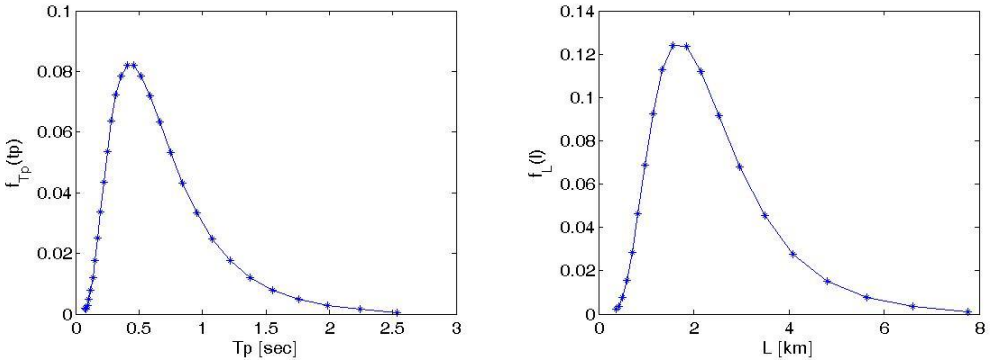

(a) **(b)**

Figure 5.6*. Lognormal distribution of pulse period (a) and rupture length (b), for M=5*

[3] Pulse period and rupture length distributions are discretized respectively 30 and 20 points.

In this first case, fault length is 20 km so the distance between the site and lower extreme of the fault is 25 km. Recalling application intervals of pulse occurrence probability model (R<30km), it can be derived that, in the considered site, pulse like effects will be negligible (because a zero occurrence probability is considered in the procedure) only if the epicenter is in the upper extreme of the rupture in fact, in this case, the rupture propagation do not proceed toward the site: this condition is verified once every three simulated scenario because epicenter has only three possible position on the rupture. (see previous section). Computed response spectra using ordinary PSHA (Eq. 4) and modified analyses in order to account for pulse-like effects (Eq. 5, 6 and 7) are reported in Fig 5.7a. In the same plot, UHS computed neglecting statistical dispersion of Tp is reported. It is clear that, for this simple case, dispersion of Tp distribution does not modified significantly the spectrum shape. Ratio between two spectra is shown in Fig. 5.7b.

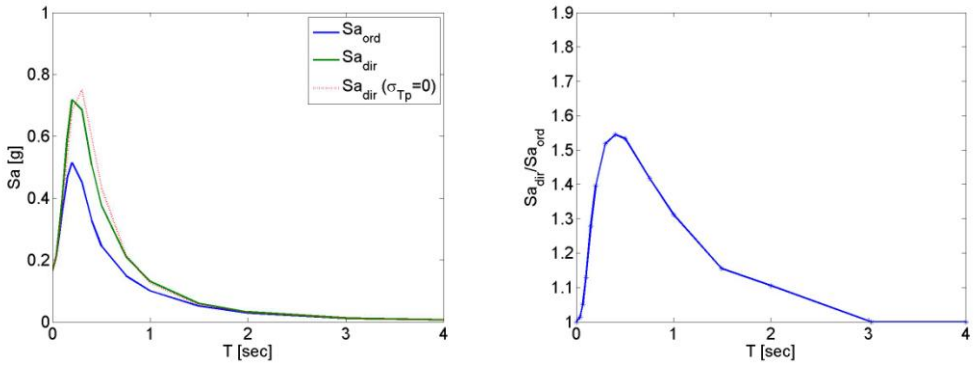

(a) (b)

Figure 5.7. *Response spectra for ordinary and NS PSHA (a), and difference of spectra (b)*

Maximum difference between response spectra is for vibration period (T) equal to 0.5 sec which is the median value computed using Eq. 2 with magnitude equal to 5. Disaggregation analyses of pulse period have been performed starting from the response spectra in near source conditions

(accounting for pulse-like effects) and considering T equal to 0.5, 1.0 and 2.0 sec. Results are reported in Fig 5.8.

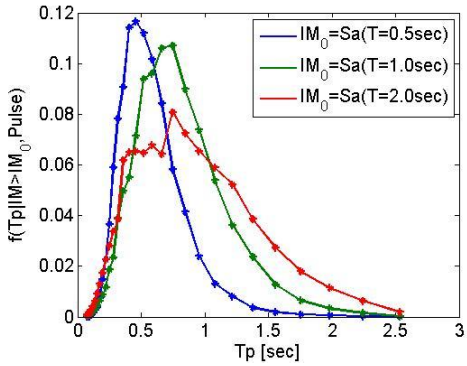

Figure 5.8. *Marginal Tp distributions from disaggregation analyses*.

Because only one magnitude values has been used, disaggregation of Tp is a distribution always unimodal and with a similar shape but mode changes position depending on the vibration period considered in disaggregation. Disaggregations of pulse occurrence are reported in Table 5.1 for the same three vibration periods.

Table 5.1 *Hazard contribution of pulse-like component for different vibration period.*

T [sec]	$P\left(Pulse\middle\|Sa(T)>Sa_0(T)\right)$
0.5	84.3%
1.0	68.8%
2.0	50.2%

Particularly interesting is result shown for T=2.0 sec. In fact, looking at Fig 5.7a, it is evident that ordinary and modified PSHA provide analogous results for this period but hazard contribution of the pulse-like component is not negligible. The result may be counterintuitive but it can be explained remembering that $f\left(Pulse\middle|IM>IM_0\right)$ does not provide any information about pulse period Tp. So, referring to numerical result for T=2.0sec, even if in the

50% of cases, the exceedence of $Sa(2.0)$ is due to pulse-like records, the modal pulse period these records is lower than 1.0 sec (Fig. 5.8) and it has minor influence on the considered spectral ordinate. As consequence, disaggregation of pulse period and of the hazard contribution of pulse-like records are information that cannot be considered independently.

5.3.2 Case 2: Magnitude equal to 6

Assuming all the event with magnitude equal to 6, distribution of pulse period and rupture length[4] are reported in Fig. 5.9.

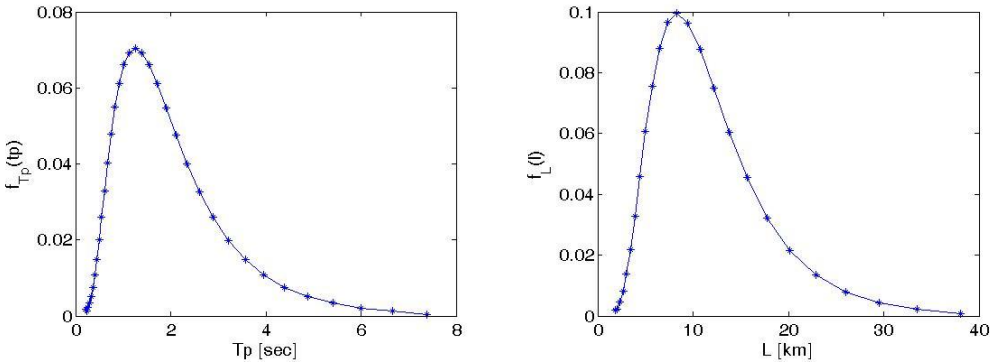

(a) **(b)**

Figure 5.9*. Lognormal distribution of pulse period (a) and rupture length (b), for M=6.*

Because the maximum rupture length obtained from Wells and Coppersmith (1994) relationship is about 38 km, in this first case, fault length is equal to 40 km. Computed response spectra using ordinary PSHA and modified analyses (with and without variability of Tp) are reported in Fig. 5.10a. Ratio between two spectra is shown in Fig. 5.10b.

[4] Pulse period and rupture length distributions are discretized respectively 35 and 25 points.

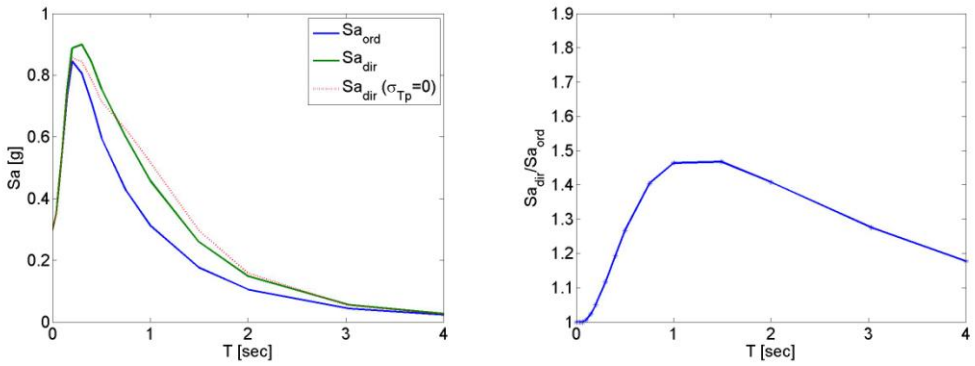

(a) **(b)**

Figure 5.10. *Response spectra for ordinary and NS PSHA (a), and difference of spectra (b)*

Disaggregation analyses of pulse period have been performed starting from the response spectra in near source conditions (accounting for pulse-like effects) and considering T equal to 0.5, 1.0 and 2.0 sec results are reported in Fig. 5.11.

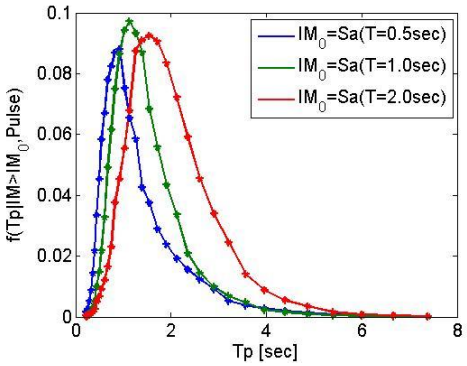

Figure 5.11. *Marginal Tp distributions*

As in the previous case, all disaggregation distribution are unimodal and the period of disaggregation influences the position of the mode. Disaggregation of pulse occurrence probability are reported in Table 5.2 for the same three vibration periods.

Table 5.2 *Hazard contribution of pulse-like component for different vibration period.*

T [sec]	$P(Pulse \mid Sa(T) > Sa_0(T))$
0.5	68.5%
1.0	78.7%
2.0	76.3%

Disaggregation for T=1.0 sec causes the maximum hazard contribution because median Tp values for M=6 is about 1.3 sec.

5.3.1 Case 3: Magnitude equal to 7

Median plus three standard deviation of rupture length[5] distribution for M=7 is equal to 190 km and median values is about 50 km. As consequence fault length has been chosen equal to 200 km. Comparison between results from ordinary and near source analyses are reported in Fig 5.12.

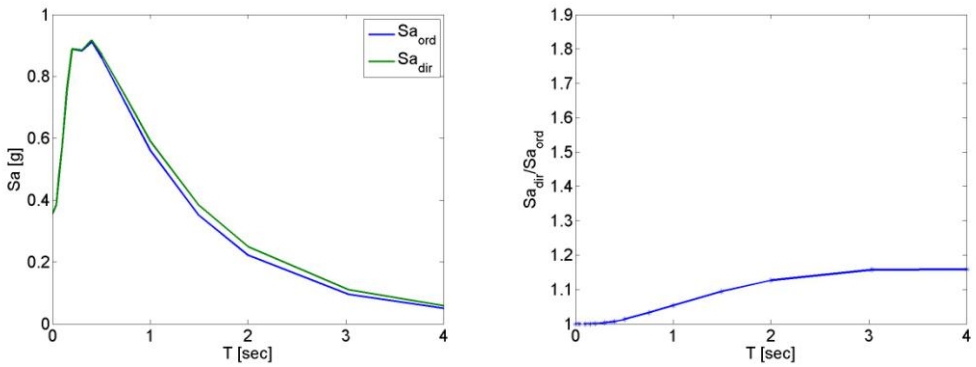

(a) **(b)**

Figure 5.12. *Marginal Response spectra for ordinary and NS PSHA (a), and difference of spectra (b)*

As expected impulsive effects are less evident that the other cases because, due to the fault length dimension, many earthquakes happen far from

[5] Pulse period and rupture length distributions are discretized respectively 40 and 30 points.

the considered site and they do not produce directivity effects (analytically this condition is reflected from the pulse occurrence probability equal to zero for distances higher than 30 km). This issue is particularly important because seismic faults have usually similar or higher dimensions and, for a single considered site, the occurrence of strong pulse-like effects may be mitigated by the occurrence of many events with no directivity characteristics and, in order to evaluate consequence of pulse-like ground motion analyses of single scenario may be necessary.

5.3.1 Case 4: PSHA with a probabilistic distribution of magnitude

On the same fault of case 3, this last case has been performed using a distribution of magnitude. In particular, in order to reduce computational effort, a discrete distribution of magnitude probability has been chosen starting from a Gutenberg-Richter magnitude occurrence relationship with minimum and maximum magnitude equal to 4.5 and 7.5 respectivly and with a negative slope of the model (b value) equal to 1. Occurrence probability for magnitude equal to 5, 6 and 7 have been utilized for numerical solution. Comparison between continue and dicrete magnitude distributions adimensionalized by the occurrence probability of M=5 ($P(5)$ or $f(5)dm$ for dicrete and continue respectively) is reported in Fig. 5.13.

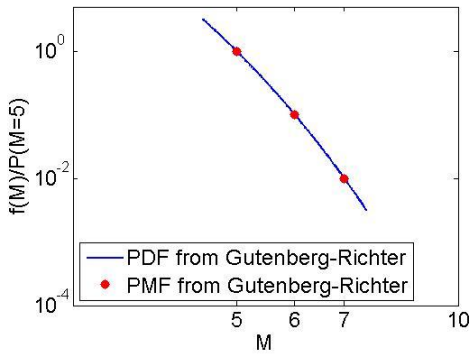

Figure 5.13. *Magnitude occurrence model*

Computed response spectra are reported in Fig 5.14.

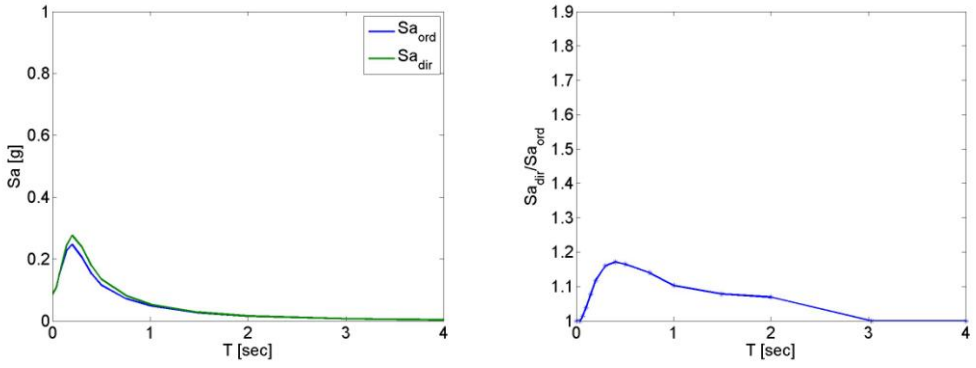

(a) (b)

Figure 5.14. *Response spectra for ordinary and NS PSHA (a), and difference of spectra (b)*

Similarly to the previous case, fault dimension determines a reduction of directivity effects observed above with smaller fault as confirmed by hazard contribution of pulse-like records reported in Table 5.3 that provides numbers significantly lower than the previous cases. An average increment of about 10% of ordinary spectral ordinates is obtained with a maximum increment for vibration period equal to about 0.5sec because events with magnitude 5 (so pulse period of about 0.5 sec) have the higher occurrence probability. So, in the general case of small magnitude events more frequent, being the distribution of pulse period function of the event magnitude, short periods are more affected by pulse-like effects.

Disaggregation of pulse occurrence probability are reported in Table 5.3 for the three vibration periods.

Table 5.3 *Hazard contribution of pulse-like component for different vibration period.*

T [sec]	$P(Pulse \mid Sa(T) > Sa_0(T))$
0.5	41.5%
1.0	33.5%
2.0	27.3%

5.4 Conclusions

In this chapter a short synthesis of the main characteristics of pulse-like ground motions is presented with particular attention to the structural response. From an engineering point of view in fact the main problem is the peculiar spectral shape of the signals which may causes unexpected inelastic displacement demands (depending on the fundamental period of the structure).

All the models available in literature that allow to account for pulse-like effects in PSHA are presented and, starting from already proposed formulation of the hazard integral, analytical expression of PSHA in near-source condition are provided. Application of the models is extended also to disaggregation analysis and some numerical examples have been implemented.

Examples' results show that with small dimension of the fault, pulse-like effects have an high probability of occurrence and as consequence increment of the ordinary hazard may be higher than 50% for some spectral periods. Conversely increasing fault dimensions, even if the maximum event magnitude increases, importance of pulse-like signals decreases being probability of pulse occurrence strongly attenuated with distance. Moreover, because distribution of pulse period is a function of the event magnitude, usually short period are more affected by pulse-like effect being small or moderate magnitude event more frequent.

Analyses of disaggregation results show that disaggregation of pulse period and disaggregation of the occurrence of pulse-like effects are information that cannot be considered independently: i.e. for a given spectral period (fundamental period of the analyzed structure) the rate of exceedance of

the spectral ordinate by pulse-like ground motions may be high even if the disaggregation of pulse period identifies a Tp enough different from the structural period for non influencing significantly the structural response. Conversely even if the Tp from disaggregation is in a dangerous ratio with the structural period, disaggregation of pulse occurrence may suggests that, in the site no pulse-like signals happen.

Numerical examples proposed identify also some critical aspects of this procedure. A part for the increasing of computational effort caused by the introduction of new variable in the classical expression of the hazard integral, an important aspect is connected to the shape of computed spectra. In fact as mentioned, the peculiar spectral shape of pulse-like signals is the cause of the unexpected structural response but, result of PSHA is an envelope of many different spectra. As consequence applying these analyses to general cases with a continue distribution of event magnitude, bump due to pulses may be spread on a large interval of period causing only a small general increment of hazard.

References

Baker, J. W. (2007) Quantitative Classification of Near-Fault Ground Motions Using Wavelet Analysis, Bull. Seism. Soc. Am., 97(5), 1486-1501.

Baker, J. W. (2008) Identification of Near-Fault Velocity and Prediction of Resulting Response Spectra, Proceeding of Geotechnical Earthquake Engn. Struct. Dyn. IV, Sacramento, CA. [Available at http://www.stanford.edu/~bakerjw/Documents/Baker%20(2008)%20Pulse%20ID,%20GEESD%20for%20distribution.pdf, last accessed 2009 august the 2nd].

Bazzurro, P., and Cornell, C. A., 1999. Disaggregation of seismic hazard, Bull. Seismol. Soc. Am. 89, 501–520.

Boore, D. M., Atkinson, G. M. (2008) Ground-Motion Prediction Equations for the Average Horizontal Component of PGA, PGV and 5%-Damped PSA at Spectral Period between 0.01s and 10.0 s, Earthquake Spectra, 24(1), 99-138.

Chioccarelli E., Iervolino I. (2010). Near-Source Seismic Demand and Pulse-Like Records: a Discussion for L'Aquila Earthquake. Earthquake Engineering and Structural Dynamics. 39(9):1039–1062.

Cornell, C. A. (2004). Hazard, ground motion and probabilistic assessment for PBSD, in Performance Based Seismic Design Concepts and Implementation, PEER Report 2004/05, Pacific Earthquake Engineering Research Center, Berkeley, California, 39-52.

Cornell, C. A., 1968. Engineering seismic risk analysis, Bull. Seismol. Soc. Am. 58, 1583–1606.

Gutenberg, B. and C. F. Richter (1944). Frequency of earthquakes in California. Bull. Seism. Soc. Am., 34:185-188

Iervolino, I., Cornell, C. A. (2008) Probability of Occurrence of Velocity Pulses in Near-Source Ground Motions, Bull. Seism. Soc. Am., 98(5), 2262-2277.

McGuire, R. K., 1995. Probabilistic seismic hazard analysis and design earthquakes: Closing the loop, Bull. Seismol. Soc. Am. 85, 1275–1284.

Reiter, L., 1990. Earthquake Hazard Analysis: Issues and Insights, Columbia University Press, New York.

Sabetta, F., Pugliese, A. (1996) Estimation of Response Spectra and Simulations of Nonstationary Earthquake ground Motion, Bull. Seism. Soc. Am., 86(2), 337-352.

Somerville, P. G., Smith, N. F., Graves, R.W., Abrahamson, N. A. (1997) Modification of Empirical Strong Motion Attenuation Relations to Include the Amplitude and Duration Effect of Rupture Directivity, Seism. Res. Lett., 68(1), 199-122.

Thotong, P., Cornell, C. A., and Baker, J. W. (2007). Explicit directivity-pulse inclusion in probabilistic seismic hazard analysis, earthquake Spectra 23, 867-891.

Tothong, P., Luco, N. (2007) Probabilistic Seismic Demand Analysis Using Advanced Ground Motion Intensity Measures, Earthquake Eng. Struct. Dyn., 36, 1837–1860.

Wells, D. L. and Coppersmith, K. J. (1994) New Empirical Relaships among Magnitude, Rupture Length, Rupture Width, Rupture Area, and Surface Displacement, Bull. Seism. Soc. Am., 87(4), 974-1002.

CHAPTER 6.
CONCLUSIONS

In this thesis the problem of identification of design earthquakes and seismic demand for performance based earthquake engineering (PBEE) is studied referring to far-field and near-source conditions.

In Chapter 2, a disaggregation analysis of seismic hazard was applied to all Italian sites via a Fortran program specifically developed. Two different spectral periods equal to 0 (PGA) and 1.0 sec and four different return periods (50, 475, 975 and 2475 yrs) were considered. The four dimension probability density function (PDF) representing the hazard contribution of each value of distance, magnitude and ε was computed and results were presented synthetically by the identification of first and second modal values of each PDF distribution; modes has been referred to as design earthquakes. Some general concepts related to this type of analyses were pointed out: (i) the first mode corresponds to an earthquake caused by the closer source (or the source the site is enclosed into) and with low-to-moderate magnitude, (ii) the second mode accounts for the influence of the more distant zones usually with larger magnitude, and (iii) moving from PGA to Sa, the number of sites with two design earthquakes increases. Moreover, showing also completed disaggregation distributions for many specific sites, other issues were deepened: although most of the Italian sites are influences by two designs earthquakes (bimodal disaggregation distribution), site with one or three design

earthquakes can be identified and in every case results can be explained analyzing seismogenetic model and attenuation trends of seismic waves; similarly dependency of design earthquakes form spectral period and from return period was analyzed and explained theoretically and some examples were shown. Limits of modal values and accordance with available INGV data were discussed. Finally practical applications of identification of design earthquakes were proposed recalling also a freely distributed software for record selection (REXEL) in which results presented have been implemented improving record input selection for earthquake engineering applications in a hazard consistent manner yet easily viable for practitioners.

In Chapter 3 the directivity-induced pulses problem was studied being particularly important for structural engineering but not yet completely known or considered in terms of design input. Study was based on a subset of fault normal (FN) and fault parallel (FP) rotated records from the next generation attenuation project (NGA) database. Analyses showed that pulse-like signals are characterized by fault normal records generally stronger than both fault parallel components and non-pulse-like ground motions. Moreover, fault-normal pulse-like signals are also characterized by a non-standard spectral shape with an increment of spectral ordinates in a range around the pulse period. Comparisons between pulse-like and non-pulse-like records show that inelastic to elastic seismic spectral displacement ratio for pulse-like records can be 20% to 70% higher than that of ordinary motions depending on the non-linearity level. This result can be explained by the peculiar spectral shape of pulse-like records.

In Chapter 4 near-source effects were investigated in the recent April 6th 2009 L'Aquila earthquake and results from NGA database were used here as a benchmark. Analyses of horizontal strike-rotated records from the mainshock seem to suggest that directivity effects occurred and that non-ordinary seismic demand affected near-source structures in fact extracted pulses and seismic demand of signals identified as pulse-like agree with the NGA data. Moreover also the fault parallel components of pulse-like stations were found to have an

inelastic-to-elastic displacement ratio not completely similar to that of ordinary records.

Finally because importance of pulse-like effects on the structural response is demonstrated and necessity to account for such effects first in probabilistic seismic hazard analysis (PSHA) and then in record selection is apparent, in Chapter 5 all the models available in literature that allow to account for pulse-like effects in PSHA were presented and, starting from already proposed formulation of the hazard integral, analytical expression of PSHA in near-source condition was provided. Application of the models was extended also to disaggregation analysis and some numerical examples were implemented.

Examples' results showed that with small dimension of the fault, pulse-like effects have an high probability of occurrence and as consequence increment of the ordinary hazard may be relevant but conversely, increasing fault dimensions, even if seismic strength of the source may increase, the role in the hazard definition of pulse-like signals decreases being pulse-like effects strongly attenuated with distance. Moreover varying the possible magnitude of the potential earthquake, pulse effects on the uniform hazard spectrum (UHS) computed by PSHA are spread on a large interval of period (independency of spectral ordinates of UHS magnifies this problem). So increment of the hazard is limited and spectral shape may result similar to the ordinary one. Adapting disaggregation analysis to PSHA in near source condition, possibility of disaggregate pulse period probability and occurrence of pulse like effects were discussed. These two information may be particularly important if pulse effects are considered in record selection but, using proposed examples, it was demonstrated that they cannot be considered independently.

APPENDIX A
PLOTS FOR L'AQUILA NEAR SOURCE STATIONS.

Analyses of fault normal and fault parallel rotated records of all the INGV stations activated from L'Aquila earthquake are reported below. In each figure three plots are shown: velocity time-histories of original signal (up), extracted pulse (center) and residual signal (down). Moreover computed pulse period (Tp) and score associated to the original signal for pulse-like classification are reported.

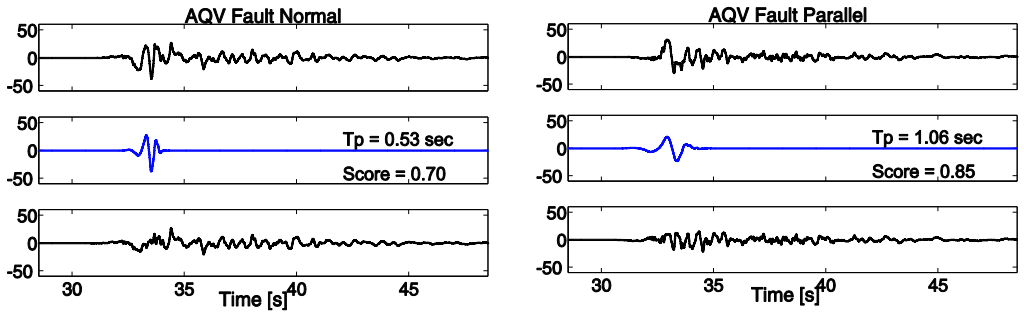

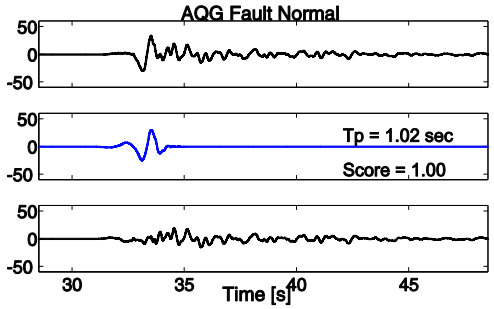
AQG Fault Normal
Tp = 1.02 sec
Score = 1.00
Time [s]

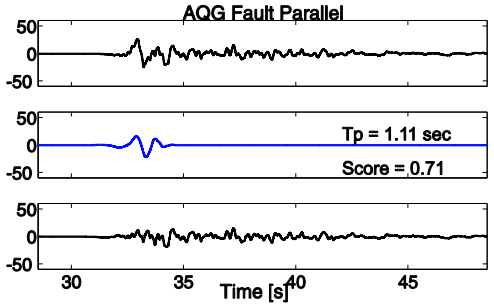
AQG Fault Parallel
Tp = 1.11 sec
Score = 0.71
Time [s]

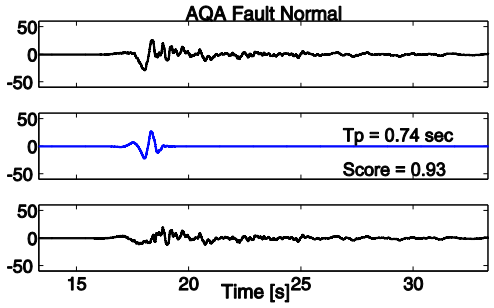
AQA Fault Normal
Tp = 0.74 sec
Score = 0.93
Time [s]

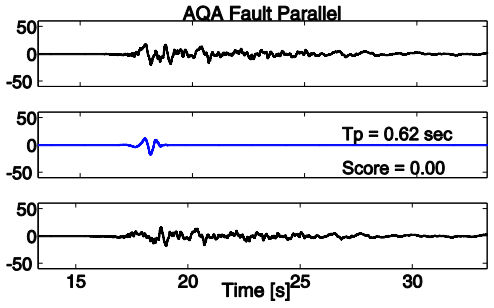
AQA Fault Parallel
Tp = 0.62 sec
Score = 0.00
Time [s]

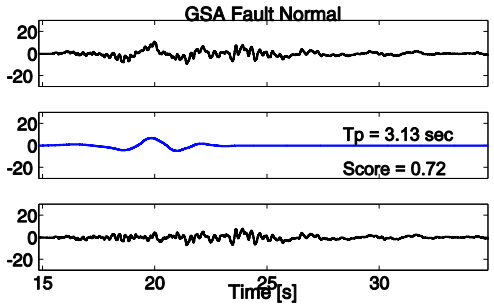
GSA Fault Normal
Tp = 3.13 sec
Score = 0.72
Time [s]

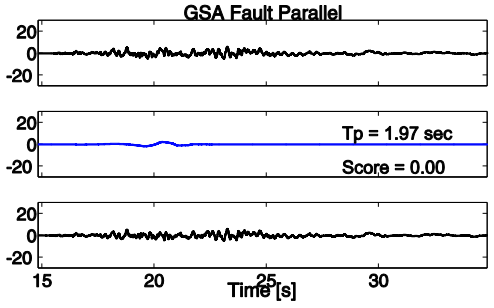
GSA Fault Parallel
Tp = 1.97 sec
Score = 0.00
Time [s]

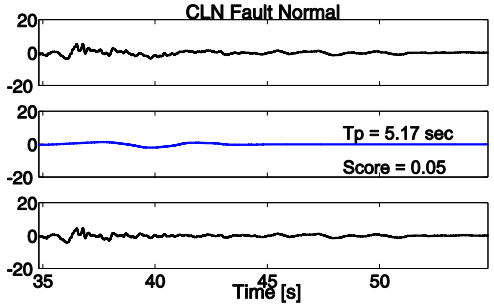
CLN Fault Normal
Tp = 5.17 sec
Score = 0.05
Time [s]

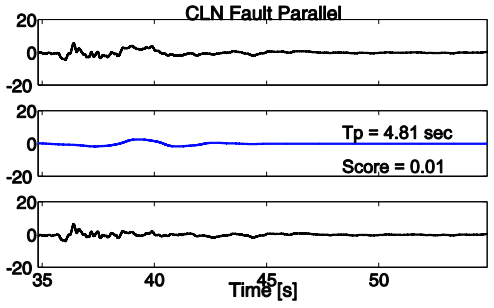
CLN Fault Parallel
Tp = 4.81 sec
Score = 0.01
Time [s]

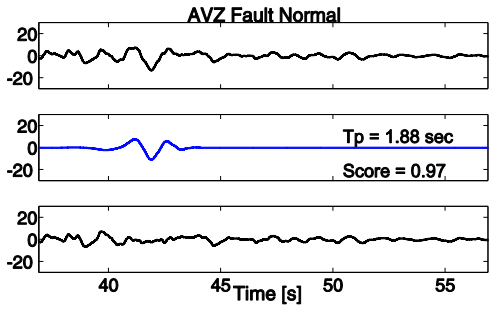
AVZ Fault Normal
Tp = 1.88 sec
Score = 0.97
Time [s]

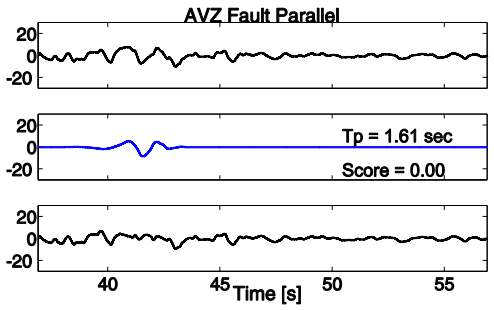
AVZ Fault Parallel
Tp = 1.61 sec
Score = 0.00
Time [s]

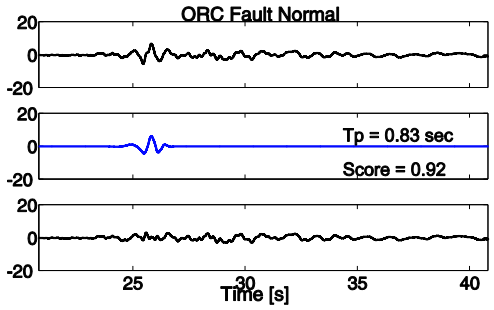
ORC Fault Normal
Tp = 0.83 sec
Score = 0.92
Time [s]

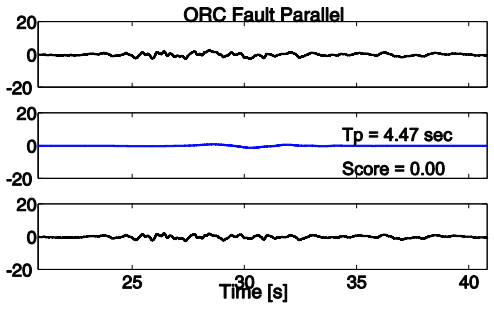
ORC Fault Parallel
Tp = 4.47 sec
Score = 0.00
Time [s]

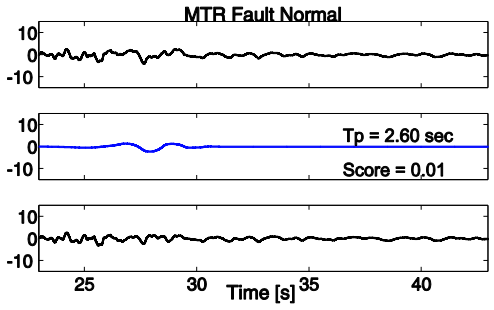
MTR Fault Normal
Tp = 2.60 sec
Score = 0.01
Time [s]

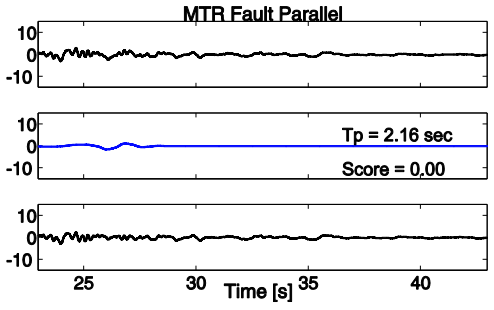
MTR Fault Parallel
Tp = 2.16 sec
Score = 0.00
Time [s]

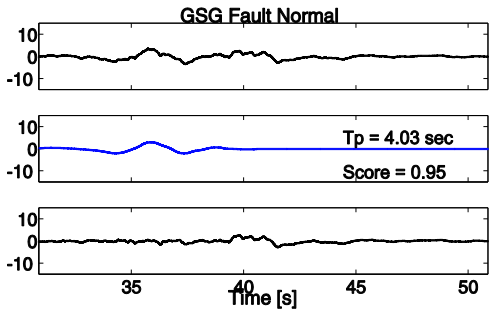
GSG Fault Normal
Tp = 4.03 sec
Score = 0.95
Time [s]

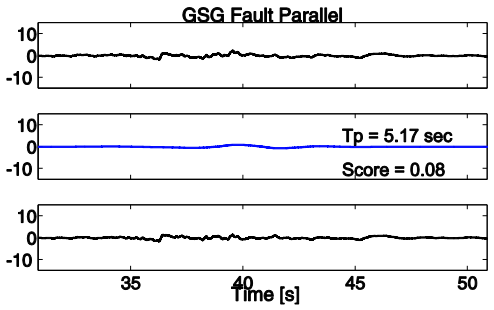
GSG Fault Parallel
Tp = 5.17 sec
Score = 0.08
Time [s]

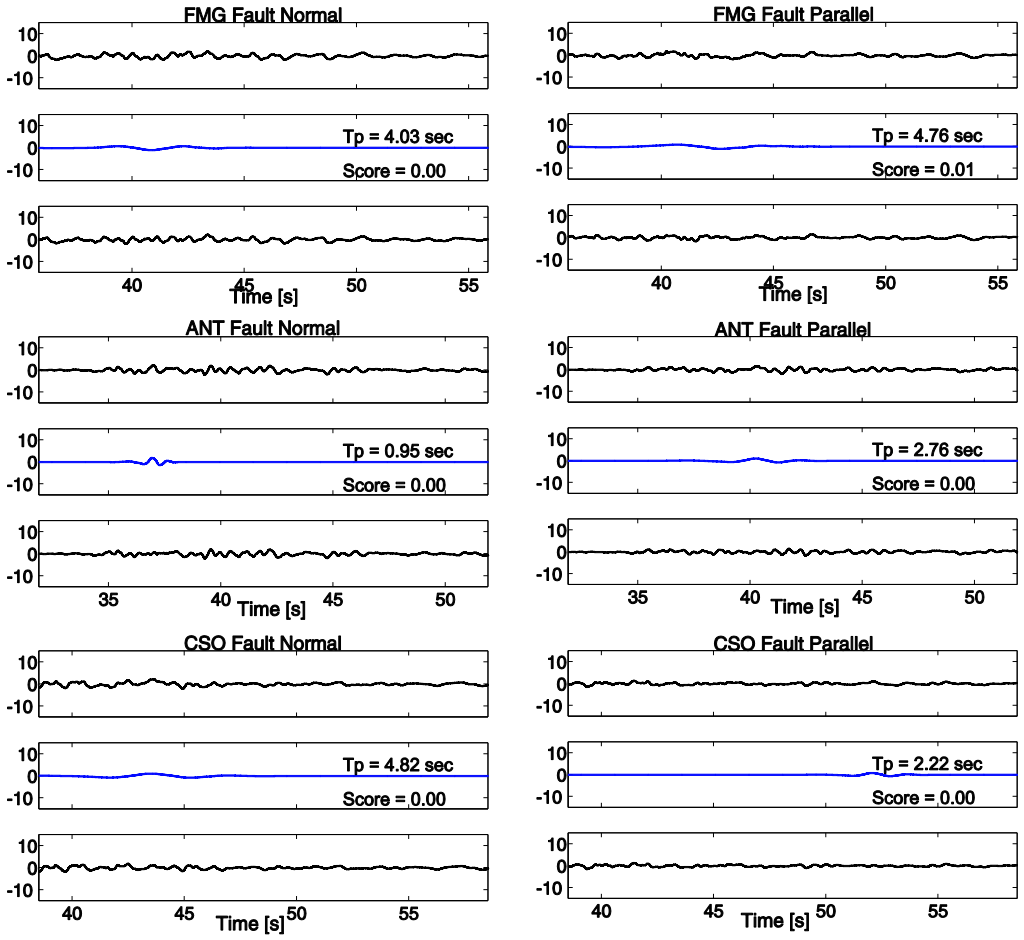
FMG Fault Normal
Tp = 4.03 sec
Score = 0.00
FMG Fault Parallel
Tp = 4.76 sec
Score = 0.01
ANT Fault Normal
Tp = 0.95 sec
Score = 0.00
ANT Fault Parallel
Tp = 2.76 sec
Score = 0.00
CSO Fault Normal
Tp = 4.82 sec
Score = 0.00
CSO Fault Parallel
Tp = 2.22 sec
Score = 0.00
Time [s]

APPENDIX B
ANALYSIS OF UN-ROTATED RECORDS FROM L'AQUILA EARTHQUAKE

Accelerometric National Network (RAN) has made available the records of the recent earthquake with epicenter in the Abruzzo (date 6/04/09 1.32AM – UTC).

Signals, corrected with a linear baseline correction and with a Buttereworth bandpass filter (Freq1=0.1, Freq2=25, Order 4), have been processed to get preliminary information about characteristic parameters of the records. Peak values, integral parameters and two different measures of duration have been computed for each component registered by the 57 accelerometric stations. Corrected records and details of correction are available on the Reluis website (http://www.reluis.it).

Peak parameters

In order to analyze peak values, data have been processed and compared to the Sabetta and Pugliese (1996) ground motion prediction equation (GMPE) in term of peak ground acceleration (PGA), peak ground velocity (PGV) and spectral acceleration (Sa) for stiff soil. Comparisons have been made adopting magnitude equal to 5.8 and 6.2; these are M_L and M_w of studied earthquake,

respectively. Because each accelerometric station produced two records of the same signal in two horizontal directions perpendicular to each other (East-West and North-South), the horizontal record chosen is that characterized by the higher PGA. This solution will be used also for the other results unless explicitly indicated. As a function of epicentral distance and for fixed spectral ordinate, the average attenuation law (and its standard deviation) is compared with the points corresponding to the values recorded at the various stations. Moreover PGA is compared with GMPE as function of Joiner and Boore distance of the site from the fault (identified as fault distance). Results are reported in the following plots:

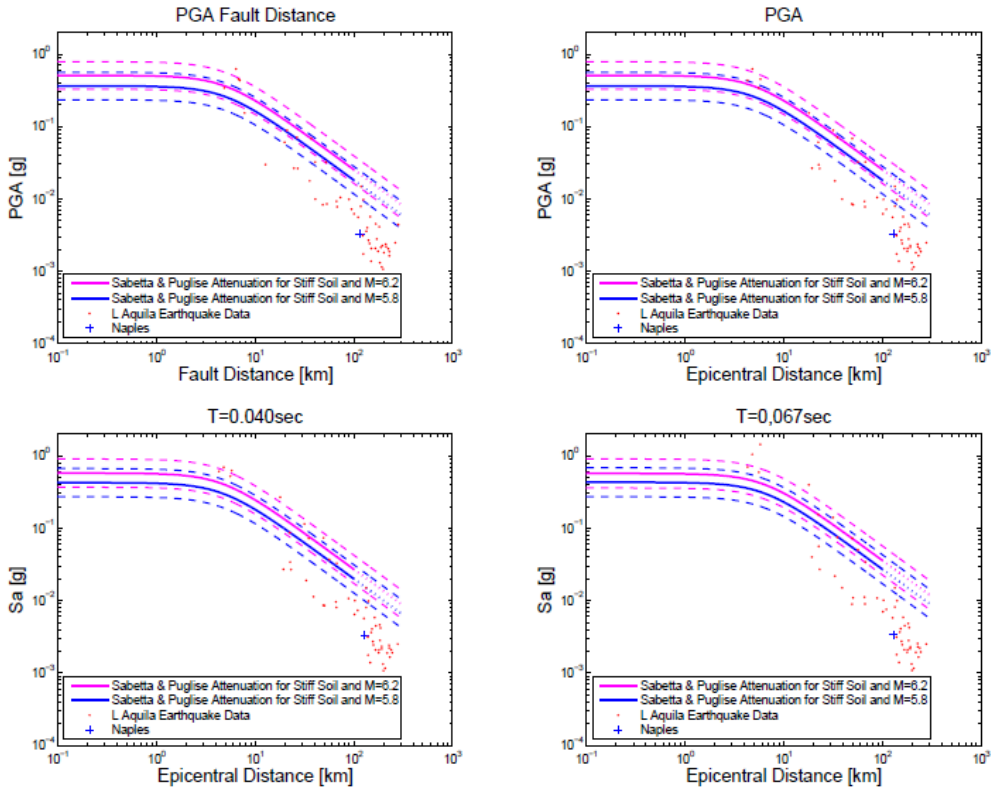

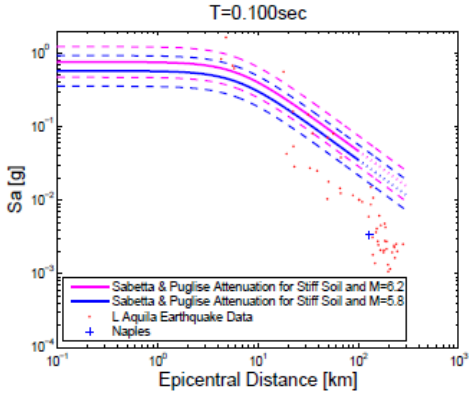
T=0.100sec
Sa [g]
Epicentral Distance [km]
Sabetta & Puglise Attenuation for Stiff Soil and M=6.2
Sabetta & Puglise Attenuation for Stiff Soil and M=5.8
L Aquila Earthquake Data
Naples

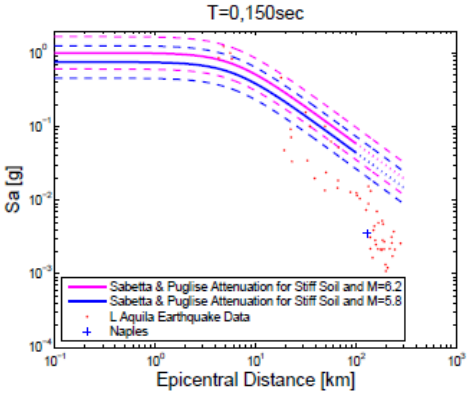
T=0,150sec
Sa [g]
Epicentral Distance [km]
Sabetta & Puglise Attenuation for Stiff Soil and M=6.2
Sabetta & Puglise Attenuation for Stiff Soil and M=5.8
L Aquila Earthquake Data
Naples

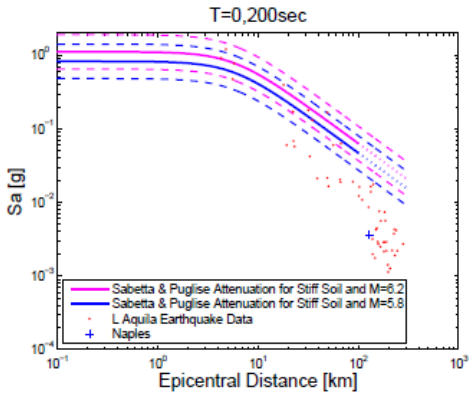
T=0,200sec
Sa [g]
Epicentral Distance [km]
Sabetta & Puglise Attenuation for Stiff Soil and M=6.2
Sabetta & Puglise Attenuation for Stiff Soil and M=5.8
L Aquila Earthquake Data
Naples

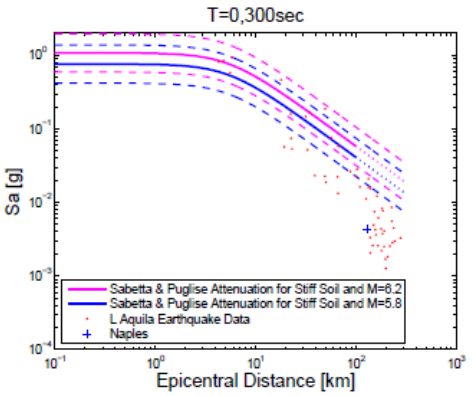
T=0,300sec
Sa [g]
Epicentral Distance [km]
Sabetta & Puglise Attenuation for Stiff Soil and M=6.2
Sabetta & Puglise Attenuation for Stiff Soil and M=5.8
L Aquila Earthquake Data
Naples

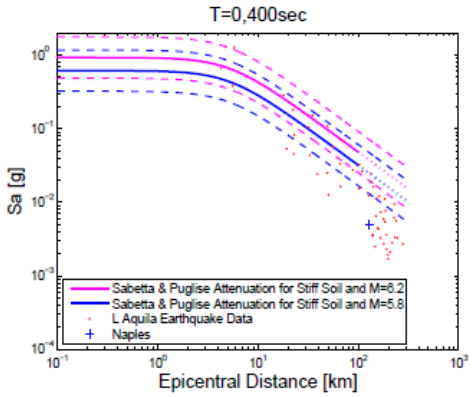
T=0,400sec
Sa [g]
Epicentral Distance [km]
Sabetta & Puglise Attenuation for Stiff Soil and M=6.2
Sabetta & Puglise Attenuation for Stiff Soil and M=5.8
L Aquila Earthquake Data
Naples

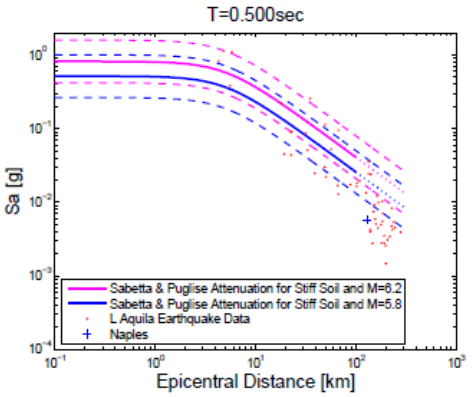
T=0.500sec
Sa [g]
Epicentral Distance [km]
Sabetta & Puglise Attenuation for Stiff Soil and M=6.2
Sabetta & Puglise Attenuation for Stiff Soil and M=5.8
L Aquila Earthquake Data
Naples

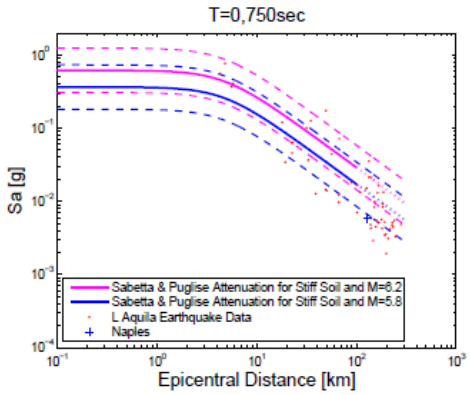
T=0,750sec
Sa [g]
Epicentral Distance [km]
Sabetta & Puglise Attenuation for Stiff Soil and M=6.2
Sabetta & Puglise Attenuation for Stiff Soil and M=5.8
L Aquila Earthquake Data
Naples

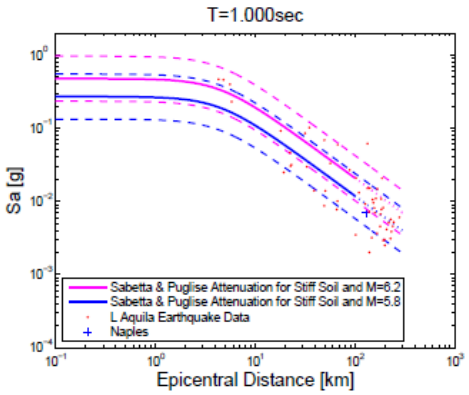
T=1.000sec
Sa [g]
Epicentral Distance [km]
Sabetta & Puglise Attenuation for Stiff Soil and M=6.2
Sabetta & Puglise Attenuation for Stiff Soil and M=5.8
L Aquila Earthquake Data
Naples

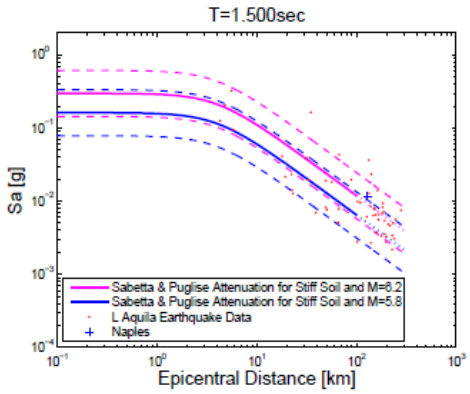
T=1.500sec
Sa [g]
Epicentral Distance [km]
Sabetta & Puglise Attenuation for Stiff Soil and M=6.2
Sabetta & Puglise Attenuation for Stiff Soil and M=5.8
L Aquila Earthquake Data
Naples

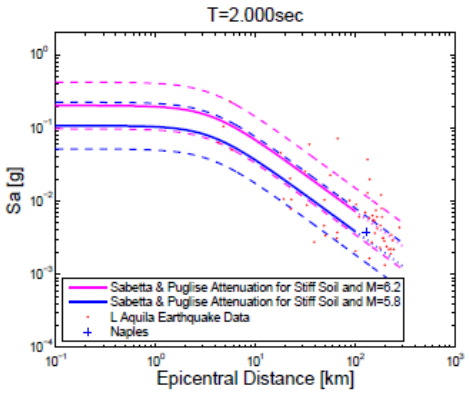
T=2.000sec
Sa [g]
Epicentral Distance [km]
Sabetta & Puglise Attenuation for Stiff Soil and M=6.2
Sabetta & Puglise Attenuation for Stiff Soil and M=5.8
L Aquila Earthquake Data
Naples

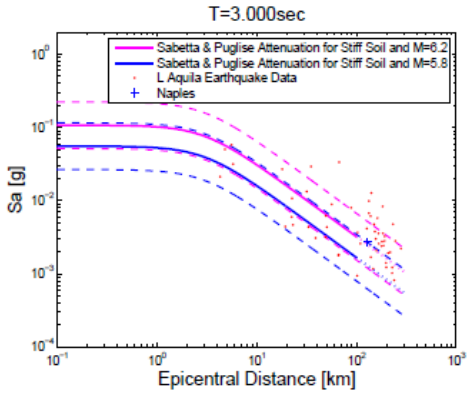
T=3.000sec
Sa [g]
Epicentral Distance [km]
Sabetta & Puglise Attenuation for Stiff Soil and M=6.2
Sabetta & Puglise Attenuation for Stiff Soil and M=5.8
L Aquila Earthquake Data
Naples

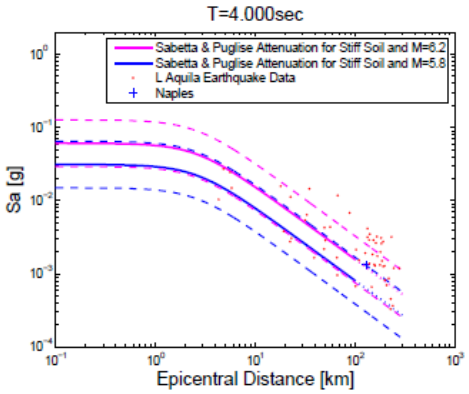
T=4.000sec
Sa [g]
Epicentral Distance [km]
Sabetta & Puglise Attenuation for Stiff Soil and M=6.2
Sabetta & Puglise Attenuation for Stiff Soil and M=5.8
L Aquila Earthquake Data
Naples

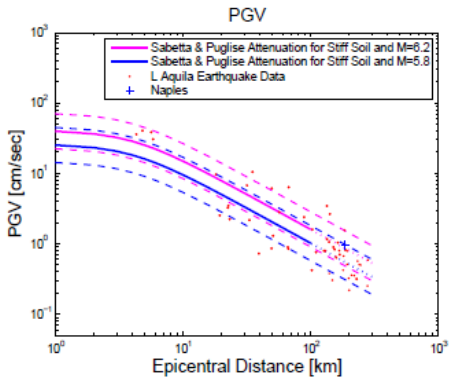

Same analyses have been conducted for vertical components. Results are reported below.

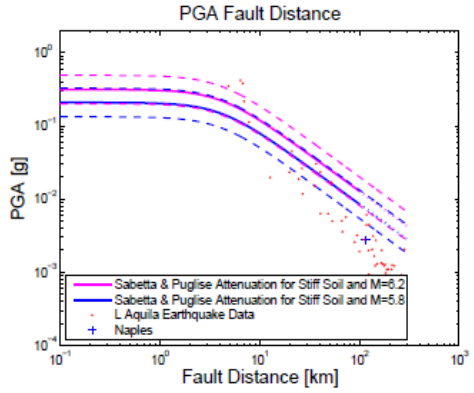

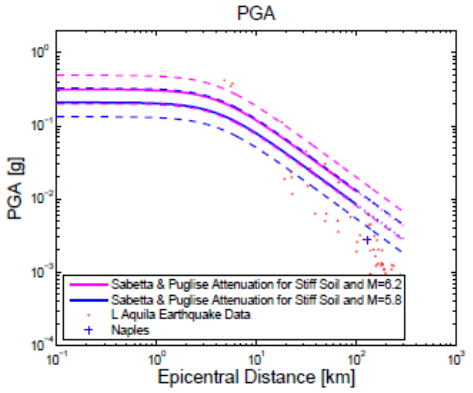

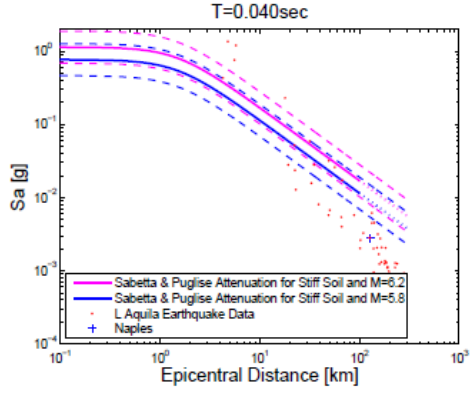

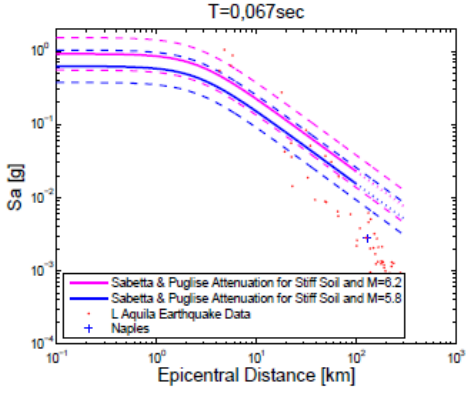

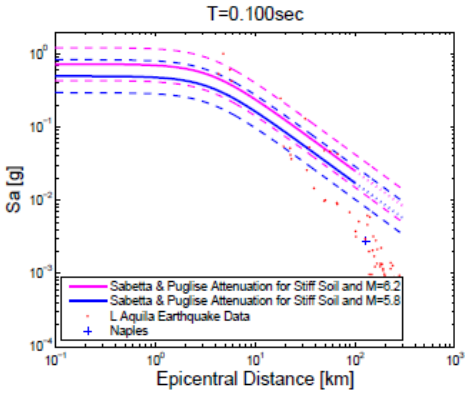
T=0.100sec
Sa [g]
Epicentral Distance [km]
Sabetta & Puglise Attenuation for Stiff Soil and M=6.2
Sabetta & Puglise Attenuation for Stiff Soil and M=5.8
L Aquila Earthquake Data
Naples

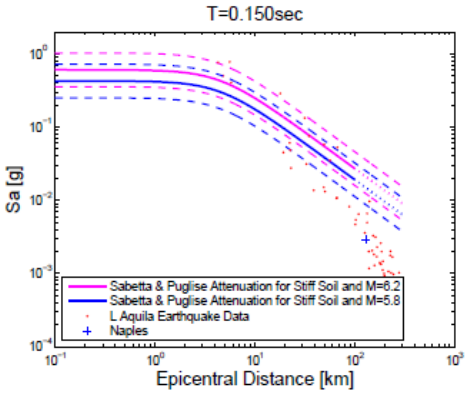
T=0.150sec
Sa [g]
Epicentral Distance [km]
Sabetta & Puglise Attenuation for Stiff Soil and M=6.2
Sabetta & Puglise Attenuation for Stiff Soil and M=5.8
L Aquila Earthquake Data
Naples

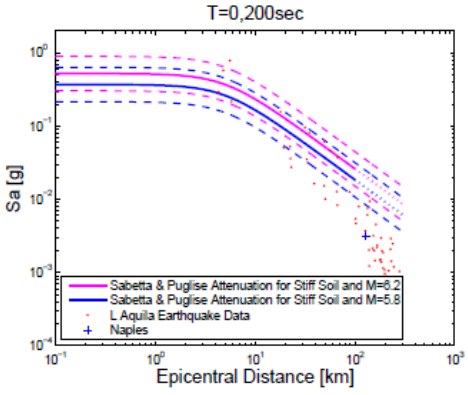
T=0,200sec
Sa [g]
Epicentral Distance [km]
Sabetta & Puglise Attenuation for Stiff Soil and M=6.2
Sabetta & Puglise Attenuation for Stiff Soil and M=5.8
L Aquila Earthquake Data
Naples

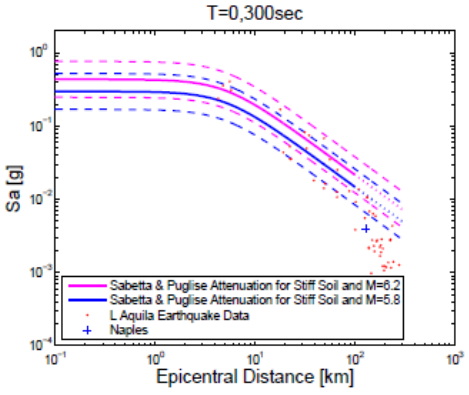
T=0,300sec
Sa [g]
Epicentral Distance [km]
Sabetta & Puglise Attenuation for Stiff Soil and M=6.2
Sabetta & Puglise Attenuation for Stiff Soil and M=5.8
L Aquila Earthquake Data
Naples

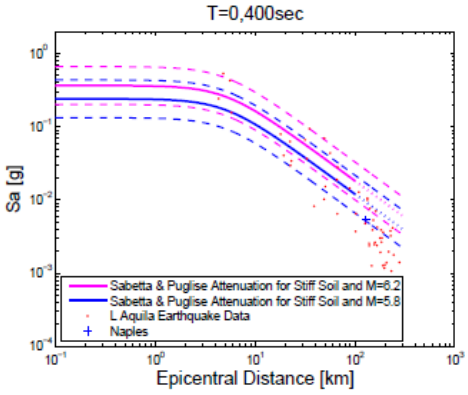
T=0,400sec
Sa [g]
Epicentral Distance [km]
Sabetta & Puglise Attenuation for Stiff Soil and M=6.2
Sabetta & Puglise Attenuation for Stiff Soil and M=5.8
L Aquila Earthquake Data
Naples

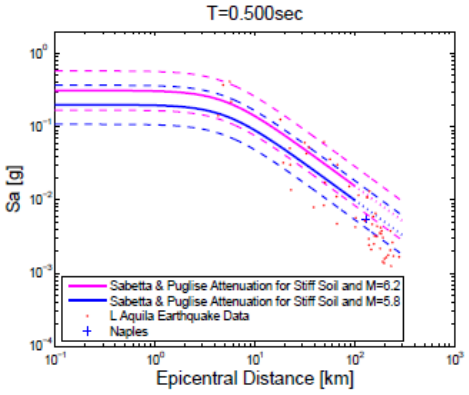
T=0.500sec
Sa [g]
Epicentral Distance [km]
Sabetta & Puglise Attenuation for Stiff Soil and M=6.2
Sabetta & Puglise Attenuation for Stiff Soil and M=5.8
L Aquila Earthquake Data
Naples

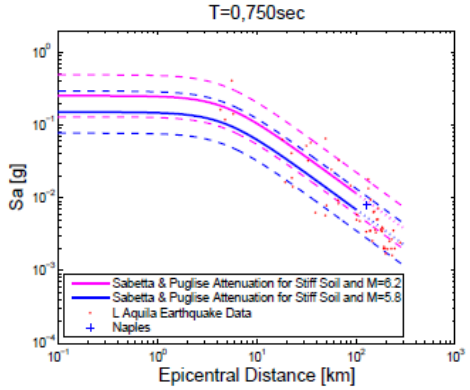
T=0,750sec
Sa [g]
Epicentral Distance [km]
Sabetta & Puglise Attenuation for Stiff Soil and M=6.2
Sabetta & Puglise Attenuation for Stiff Soil and M=5.8
L Aquila Earthquake Data
Naples

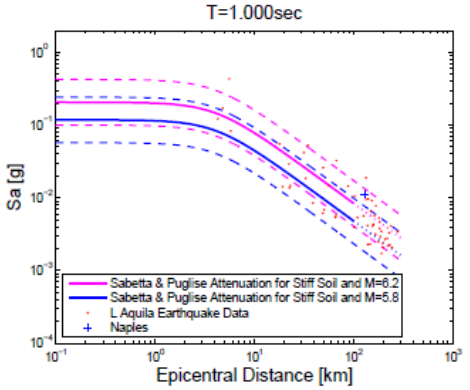
T=1.000sec
Sa [g]
Epicentral Distance [km]
Sabetta & Puglise Attenuation for Stiff Soil and M=6.2
Sabetta & Puglise Attenuation for Stiff Soil and M=5.8
L Aquila Earthquake Data
Naples

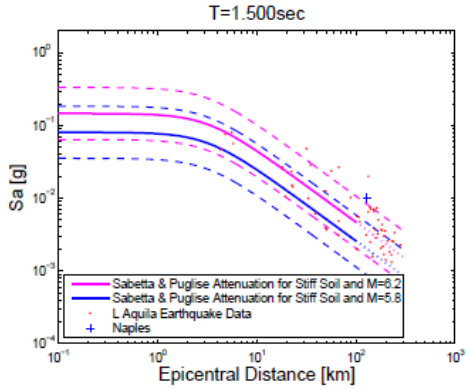
T=1.500sec
Sa [g]
Epicentral Distance [km]
Sabetta & Puglise Attenuation for Stiff Soil and M=6.2
Sabetta & Puglise Attenuation for Stiff Soil and M=5.8
L Aquila Earthquake Data
Naples

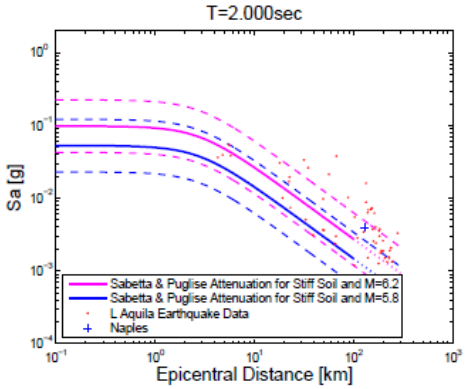
T=2.000sec
Sa [g]
Epicentral Distance [km]
Sabetta & Puglise Attenuation for Stiff Soil and M=6.2
Sabetta & Puglise Attenuation for Stiff Soil and M=5.8
L Aquila Earthquake Data
Naples

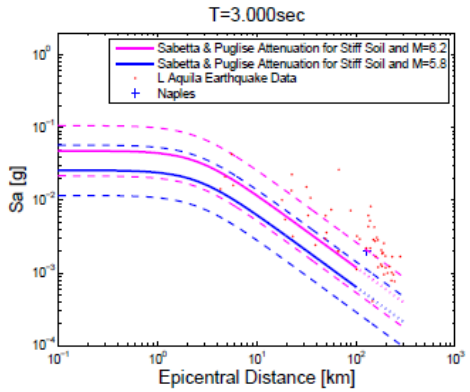
T=3.000sec
Sa [g]
Epicentral Distance [km]
Sabetta & Puglise Attenuation for Stiff Soil and M=6.2
Sabetta & Puglise Attenuation for Stiff Soil and M=5.8
L Aquila Earthquake Data
Naples

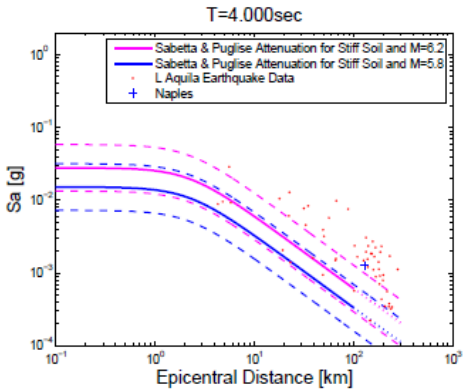
T=4.000sec
Sa [g]
Epicentral Distance [km]
Sabetta & Puglise Attenuation for Stiff Soil and M=6.2
Sabetta & Puglise Attenuation for Stiff Soil and M=5.8
L Aquila Earthquake Data
Naples

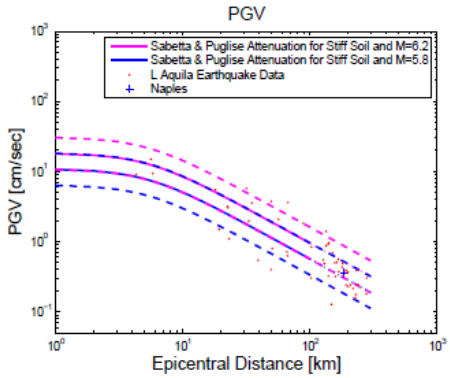

Recorded signals were also grouped in bins of 10 km of epicentral distance and the average spectrum of each bin is compared with the average spectrum obtained from the attenuation law for a distance equal to the average distance of group of records.

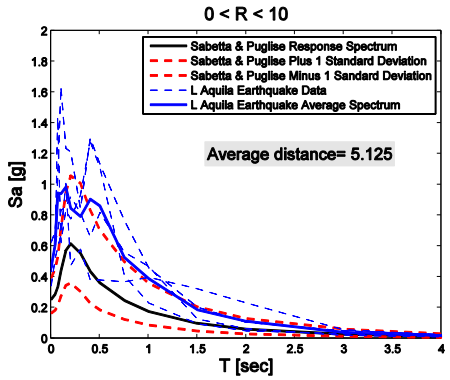

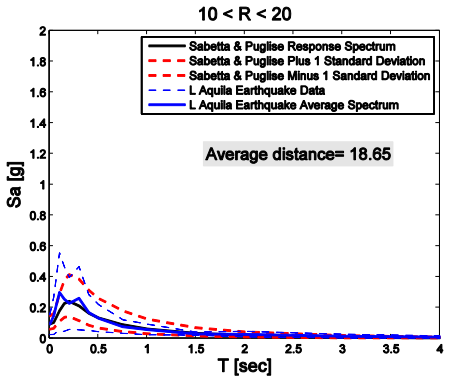

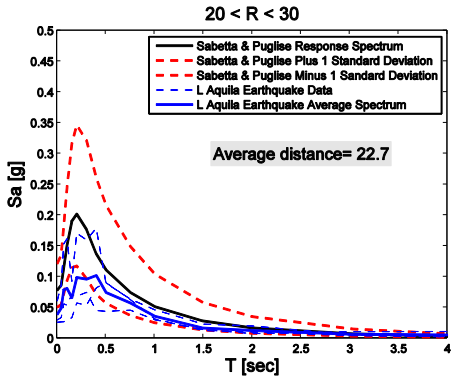
20 < R < 30
Sabetta & Puglise Response Spectrum
Sabetta & Puglise Plus 1 Standard Deviation
Sabetta & Puglise Minus 1 Sandard Deviation
L Aquila Earthquake Data
L Aquila Earthquake Average Spectrum
Average distance= 22.7
Sa [g]
T [sec]

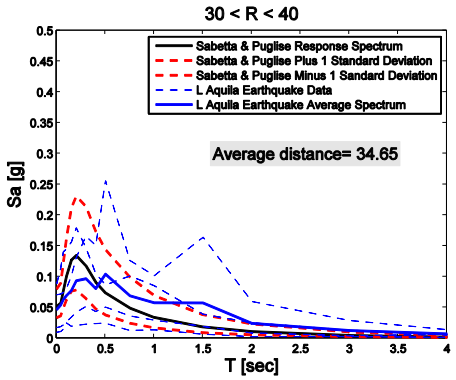
30 < R < 40
Sabetta & Puglise Response Spectrum
Sabetta & Puglise Plus 1 Standard Deviation
Sabetta & Puglise Minus 1 Sandard Deviation
L Aquila Earthquake Data
L Aquila Earthquake Average Spectrum
Average distance= 34.65
Sa [g]
T [sec]

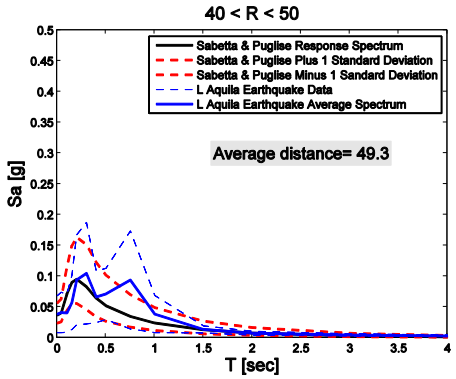
40 < R < 50
Sabetta & Puglise Response Spectrum
Sabetta & Puglise Plus 1 Standard Deviation
Sabetta & Puglise Minus 1 Sandard Deviation
L Aquila Earthquake Data
L Aquila Earthquake Average Spectrum
Average distance= 49.3
Sa [g]
T [sec]

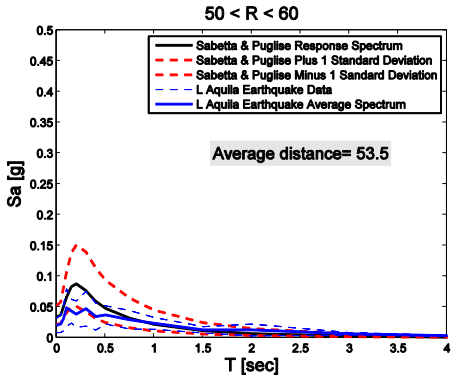
50 < R < 60
Sabetta & Puglise Response Spectrum
Sabetta & Puglise Plus 1 Standard Deviation
Sabetta & Puglise Minus 1 Sandard Deviation
L Aquila Earthquake Data
L Aquila Earthquake Average Spectrum
Average distance= 53.5
Sa [g]
T [sec]

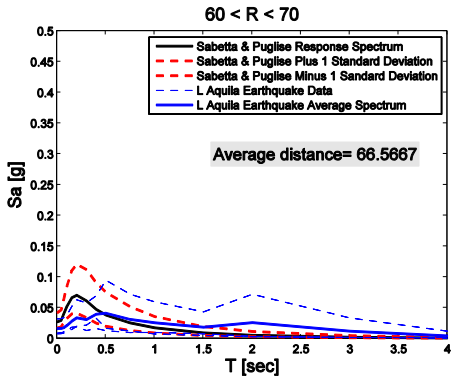
60 < R < 70
Sabetta & Puglise Response Spectrum
Sabetta & Puglise Plus 1 Standard Deviation
Sabetta & Puglise Minus 1 Sandard Deviation
L Aquila Earthquake Data
L Aquila Earthquake Average Spectrum
Average distance= 66.5667
Sa [g]
T [sec]

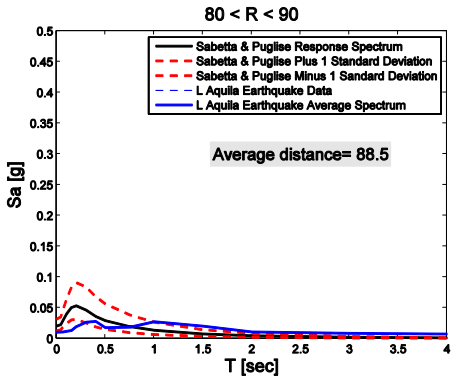
80 < R < 90
Sabetta & Puglise Response Spectrum
Sabetta & Puglise Plus 1 Standard Deviation
Sabetta & Puglise Minus 1 Sandard Deviation
L Aquila Earthquake Data
L Aquila Earthquake Average Spectrum
Average distance= 88.5
Sa [g]
T [sec]

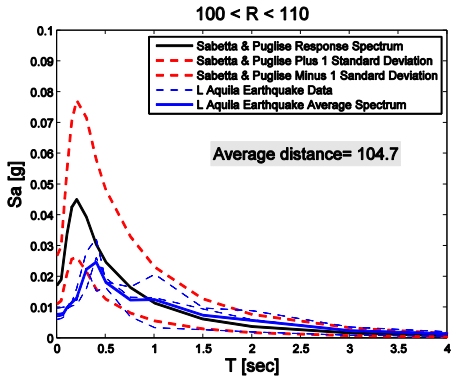
100 < R < 110
Sabetta & Puglise Response Spectrum
Sabetta & Puglise Plus 1 Standard Deviation
Sabetta & Puglise Minus 1 Sandard Deviation
L Aquila Earthquake Data
L Aquila Earthquake Average Spectrum
Average distance= 104.7
Sa [g]
T [sec]

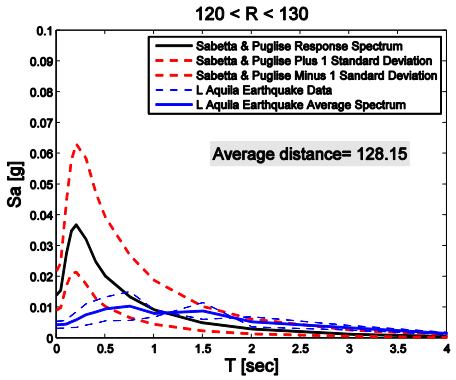
120 < R < 130
Sabetta & Puglise Response Spectrum
Sabetta & Puglise Plus 1 Standard Deviation
Sabetta & Puglise Minus 1 Sandard Deviation
L Aquila Earthquake Data
L Aquila Earthquake Average Spectrum
Average distance= 128.15
Sa [g]
T [sec]

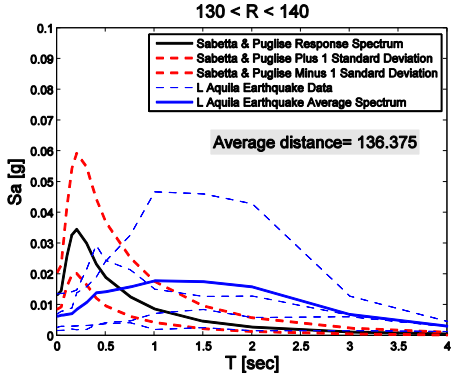
130 < R < 140
Sabetta & Puglise Response Spectrum
Sabetta & Puglise Plus 1 Standard Deviation
Sabetta & Puglise Minus 1 Sandard Deviation
L Aquila Earthquake Data
L Aquila Earthquake Average Spectrum
Average distance= 136.375
Sa [g]
T [sec]

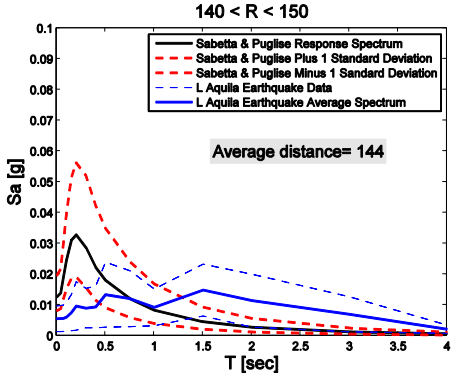
140 < R < 150
Sabetta & Puglise Response Spectrum
Sabetta & Puglise Plus 1 Standard Deviation
Sabetta & Puglise Minus 1 Sandard Deviation
L Aquila Earthquake Data
L Aquila Earthquake Average Spectrum
Average distance= 144
Sa [g]
T [sec]

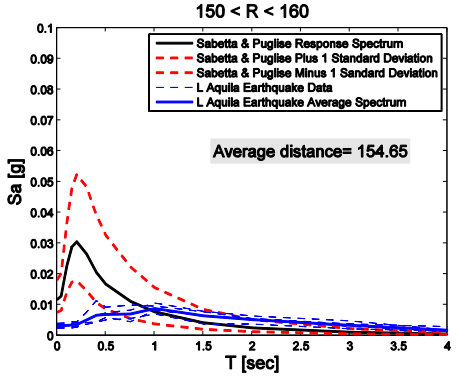
150 < R < 160
Sabetta & Puglise Response Spectrum
Sabetta & Puglise Plus 1 Standard Deviation
Sabetta & Puglise Minus 1 Sandard Deviation
L Aquila Earthquake Data
L Aquila Earthquake Average Spectrum
Average distance= 154.65
Sa [g]
T [sec]

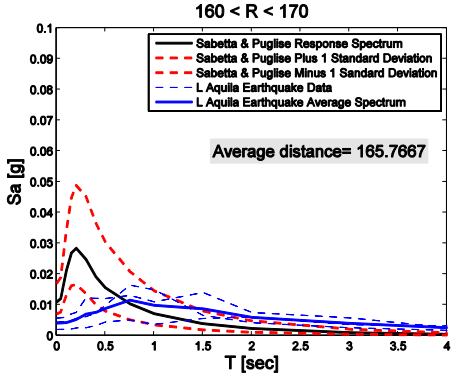
160 < R < 170
Sabetta & Puglise Response Spectrum
Sabetta & Puglise Plus 1 Standard Deviation
Sabetta & Puglise Minus 1 Sandard Deviation
L Aquila Earthquake Data
L Aquila Earthquake Average Spectrum
Average distance= 165.7667
Sa [g]
T [sec]

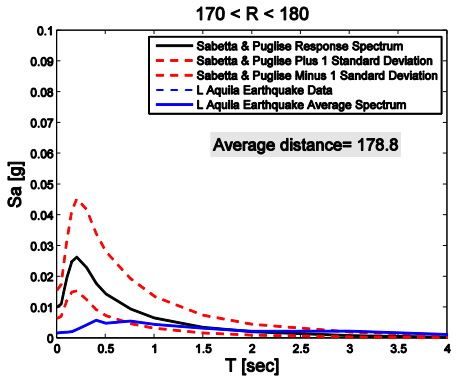
170 < R < 180
Sabetta & Puglise Response Spectrum
Sabetta & Puglise Plus 1 Standard Deviation
Sabetta & Puglise Minus 1 Sandard Deviation
L Aquila Earthquake Data
L Aquila Earthquake Average Spectrum
Average distance= 178.8
Sa [g]
T [sec]

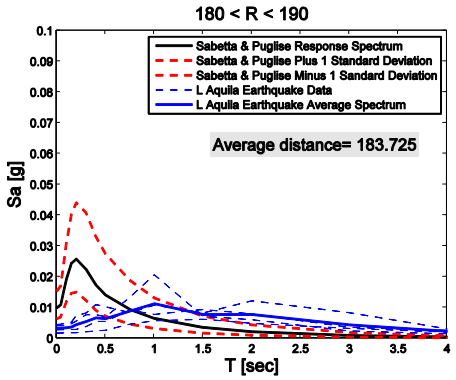
180 < R < 190
Sabetta & Puglise Response Spectrum
Sabetta & Puglise Plus 1 Standard Deviation
Sabetta & Puglise Minus 1 Sandard Deviation
L Aquila Earthquake Data
L Aquila Earthquake Average Spectrum
Average distance= 183.725
Sa [g]
T [sec]

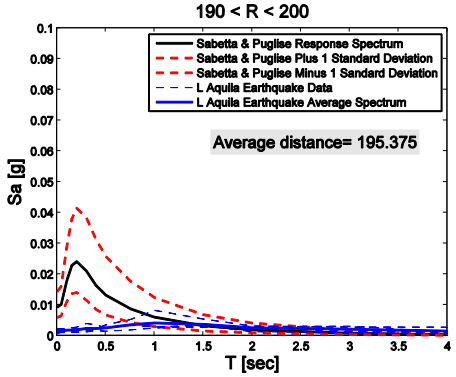
190 < R < 200
Sabetta & Puglise Response Spectrum
Sabetta & Puglise Plus 1 Standard Deviation
Sabetta & Puglise Minus 1 Sandard Deviation
L Aquila Earthquake Data
L Aquila Earthquake Average Spectrum
Average distance= 195.375
Sa [g]
T [sec]

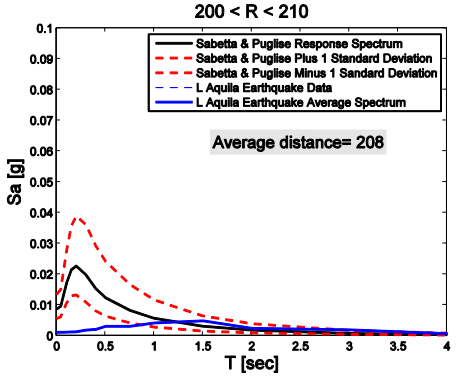
200 < R < 210
Sabetta & Puglise Response Spectrum
Sabetta & Puglise Plus 1 Standard Deviation
Sabetta & Puglise Minus 1 Sandard Deviation
L Aquila Earthquake Data
L Aquila Earthquake Average Spectrum
Average distance= 208
Sa [g]
T [sec]

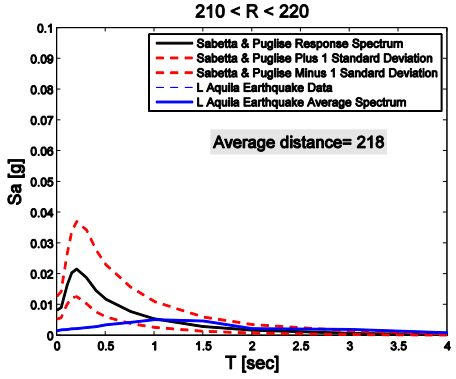
210 < R < 220
Sabetta & Puglise Response Spectrum
Sabetta & Puglise Plus 1 Standard Deviation
Sabetta & Puglise Minus 1 Sandard Deviation
L Aquila Earthquake Data
L Aquila Earthquake Average Spectrum
Average distance= 218
Sa [g]
T [sec]

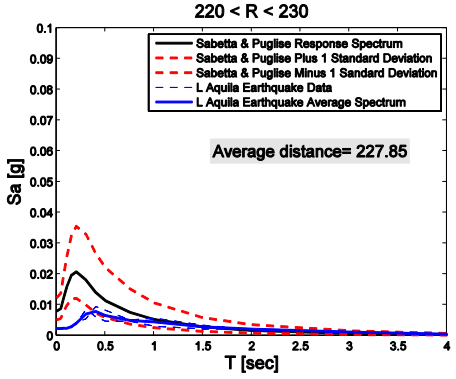
220 < R < 230
Sabetta & Puglise Response Spectrum
Sabetta & Puglise Plus 1 Standard Deviation
Sabetta & Puglise Minus 1 Sandard Deviation
L Aquila Earthquake Data
L Aquila Earthquake Average Spectrum
Average distance= 227.85
Sa [g]
T [sec]

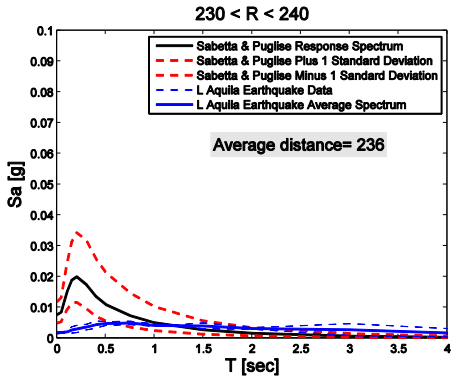

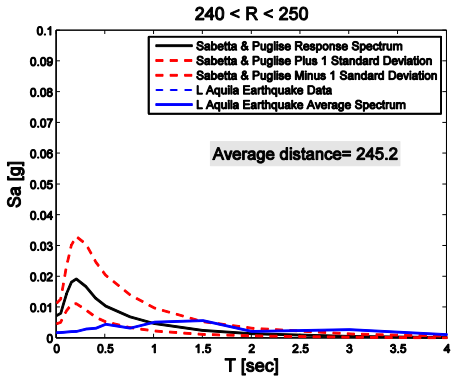

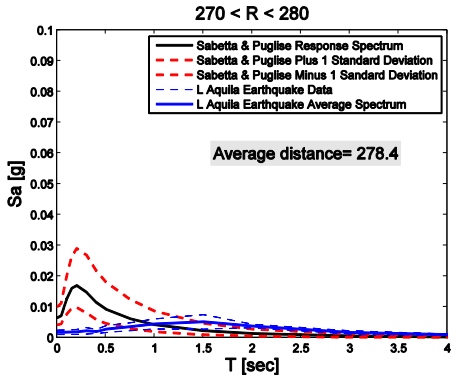

Same analyses have been conducted for vertical components. Results are reported below.

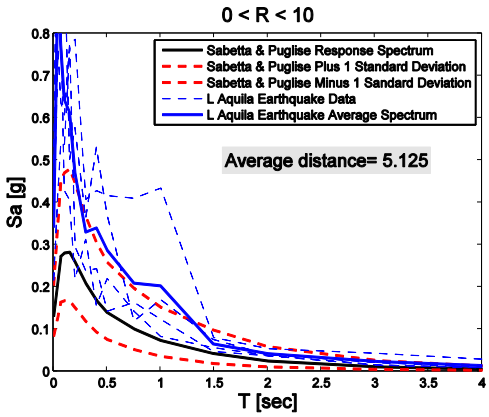

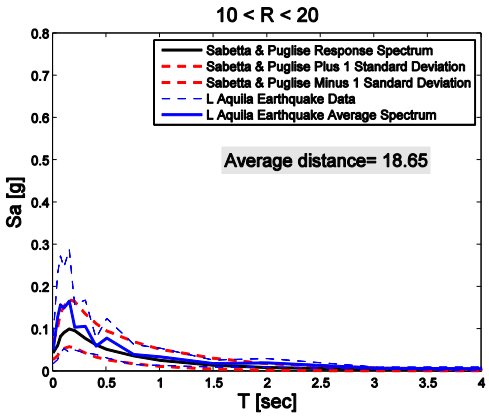

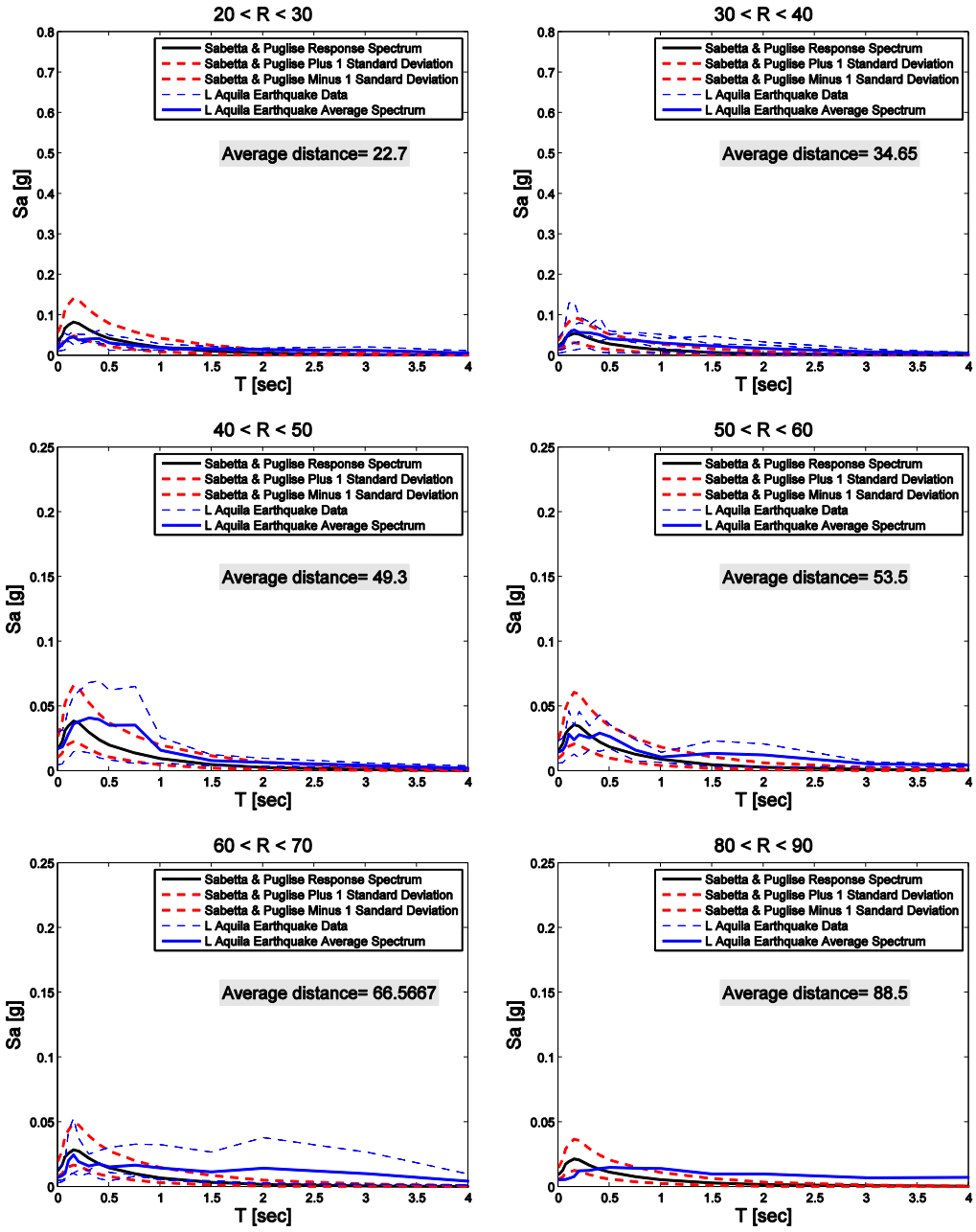
20 < R < 30
Sabetta & Puglise Response Spectrum
Sabetta & Puglise Plus 1 Standard Deviation
Sabetta & Puglise Minus 1 Sandard Deviation
L Aquila Earthquake Data
L Aquila Earthquake Average Spectrum
Average distance= 22.7
Sa [g]
T [sec]
30 < R < 40
Average distance= 34.65
40 < R < 50
Average distance= 49.3
50 < R < 60
Average distance= 53.5
60 < R < 70
Average distance= 66.5667
80 < R < 90
Average distance= 88.5

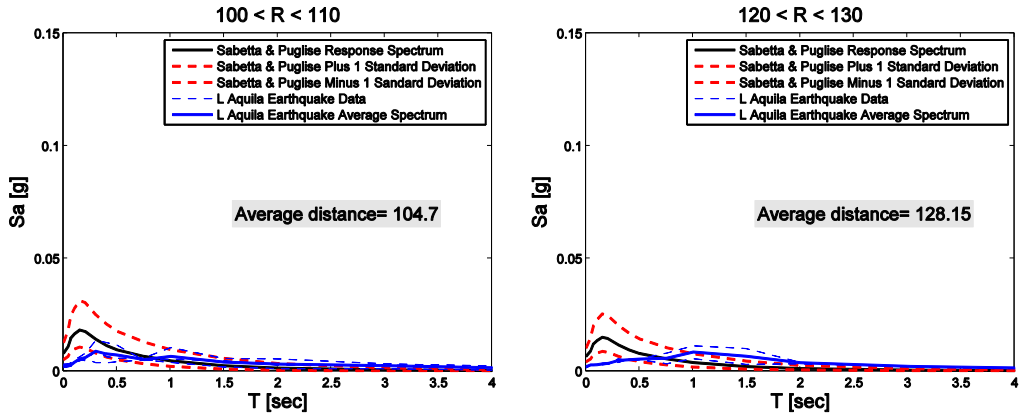
100 < R < 110
Sabetta & Puglise Response Spectrum
Sabetta & Puglise Plus 1 Standard Deviation
Sabetta & Puglise Minus 1 Sandard Deviation
L Aquila Earthquake Data
L Aquila Earthquake Average Spectrum
Average distance= 104.7
Sa [g]
T [sec]

120 < R < 130
Sabetta & Puglise Response Spectrum
Sabetta & Puglise Plus 1 Standard Deviation
Sabetta & Puglise Minus 1 Sandard Deviation
L Aquila Earthquake Data
L Aquila Earthquake Average Spectrum
Average distance= 128.15
Sa [g]
T [sec]

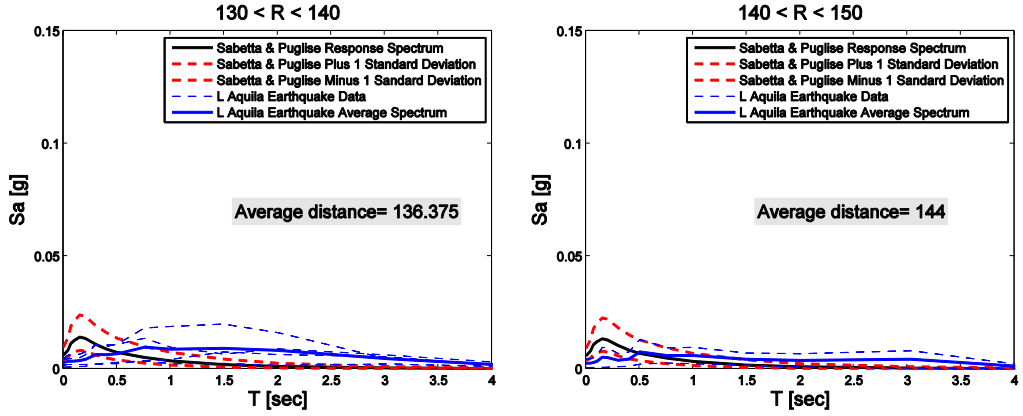
130 < R < 140
Sabetta & Puglise Response Spectrum
Sabetta & Puglise Plus 1 Standard Deviation
Sabetta & Puglise Minus 1 Sandard Deviation
L Aquila Earthquake Data
L Aquila Earthquake Average Spectrum
Average distance= 136.375
Sa [g]
T [sec]

140 < R < 150
Sabetta & Puglise Response Spectrum
Sabetta & Puglise Plus 1 Standard Deviation
Sabetta & Puglise Minus 1 Sandard Deviation
L Aquila Earthquake Data
L Aquila Earthquake Average Spectrum
Average distance= 144
Sa [g]
T [sec]

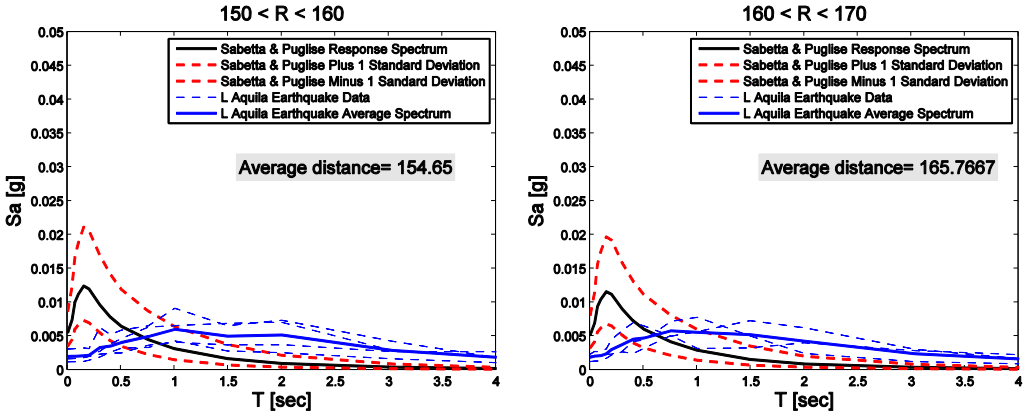
150 < R < 160
Sabetta & Puglise Response Spectrum
Sabetta & Puglise Plus 1 Standard Deviation
Sabetta & Puglise Minus 1 Sandard Deviation
L Aquila Earthquake Data
L Aquila Earthquake Average Spectrum
Average distance= 154.65
Sa [g]
T [sec]

160 < R < 170
Sabetta & Puglise Response Spectrum
Sabetta & Puglise Plus 1 Standard Deviation
Sabetta & Puglise Minus 1 Sandard Deviation
L Aquila Earthquake Data
L Aquila Earthquake Average Spectrum
Average distance= 165.7667
Sa [g]
T [sec]

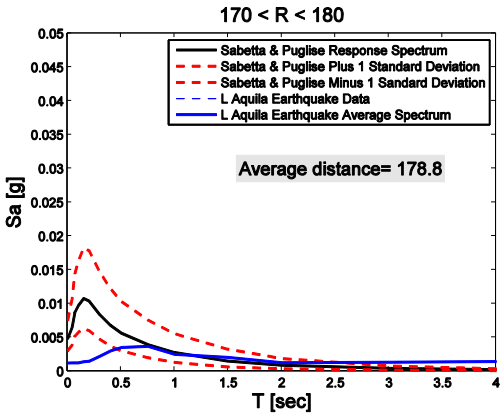
170 < R < 180
Sabetta & Puglise Response Spectrum
Sabetta & Puglise Plus 1 Standard Deviation
Sabetta & Puglise Minus 1 Sandard Deviation
L Aquila Earthquake Data
L Aquila Earthquake Average Spectrum
Average distance= 178.8
Sa [g]
T [sec]

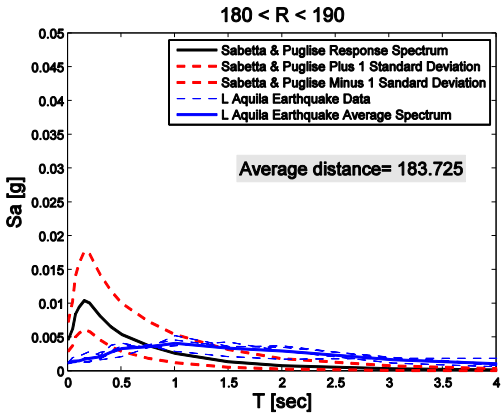
180 < R < 190
Sabetta & Puglise Response Spectrum
Sabetta & Puglise Plus 1 Standard Deviation
Sabetta & Puglise Minus 1 Sandard Deviation
L Aquila Earthquake Data
L Aquila Earthquake Average Spectrum
Average distance= 183.725
Sa [g]
T [sec]

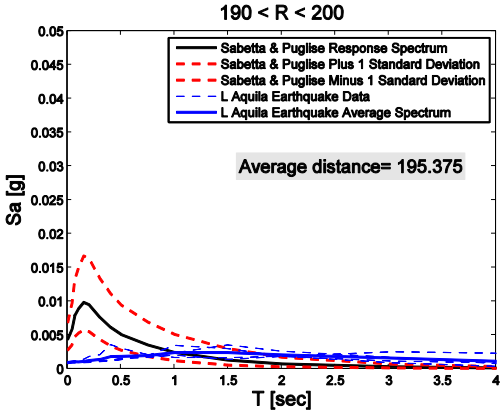
190 < R < 200
Sabetta & Puglise Response Spectrum
Sabetta & Puglise Plus 1 Standard Deviation
Sabetta & Puglise Minus 1 Sandard Deviation
L Aquila Earthquake Data
L Aquila Earthquake Average Spectrum
Average distance= 195.375
Sa [g]
T [sec]

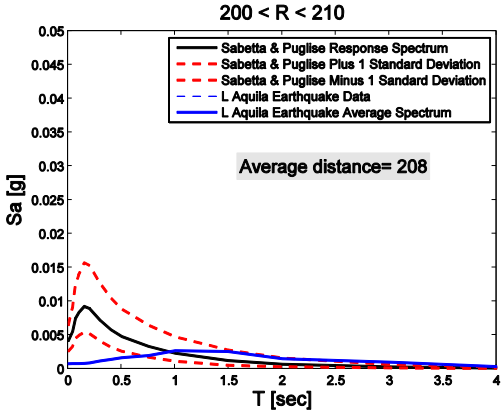
200 < R < 210
Sabetta & Puglise Response Spectrum
Sabetta & Puglise Plus 1 Standard Deviation
Sabetta & Puglise Minus 1 Sandard Deviation
L Aquila Earthquake Data
L Aquila Earthquake Average Spectrum
Average distance= 208
Sa [g]
T [sec]

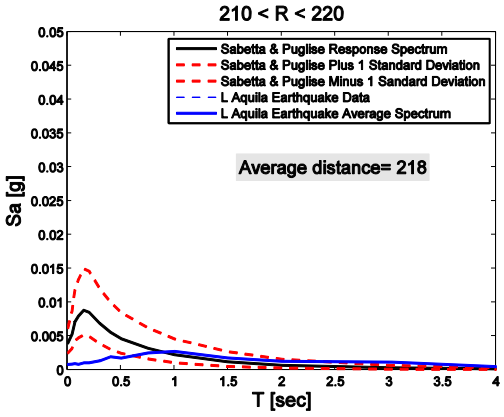
210 < R < 220
Sabetta & Puglise Response Spectrum
Sabetta & Puglise Plus 1 Standard Deviation
Sabetta & Puglise Minus 1 Sandard Deviation
L Aquila Earthquake Data
L Aquila Earthquake Average Spectrum
Average distance= 218
Sa [g]
T [sec]

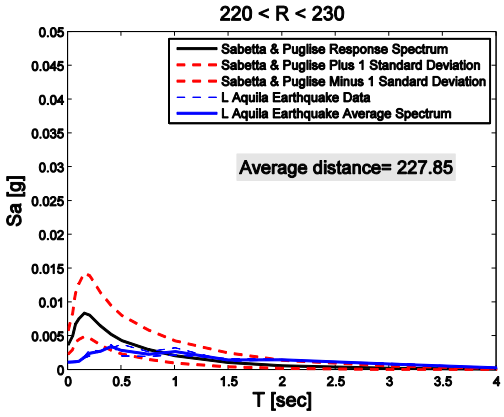
220 < R < 230
Sabetta & Puglise Response Spectrum
Sabetta & Puglise Plus 1 Standard Deviation
Sabetta & Puglise Minus 1 Sandard Deviation
L Aquila Earthquake Data
L Aquila Earthquake Average Spectrum
Average distance= 227.85
Sa [g]
T [sec]

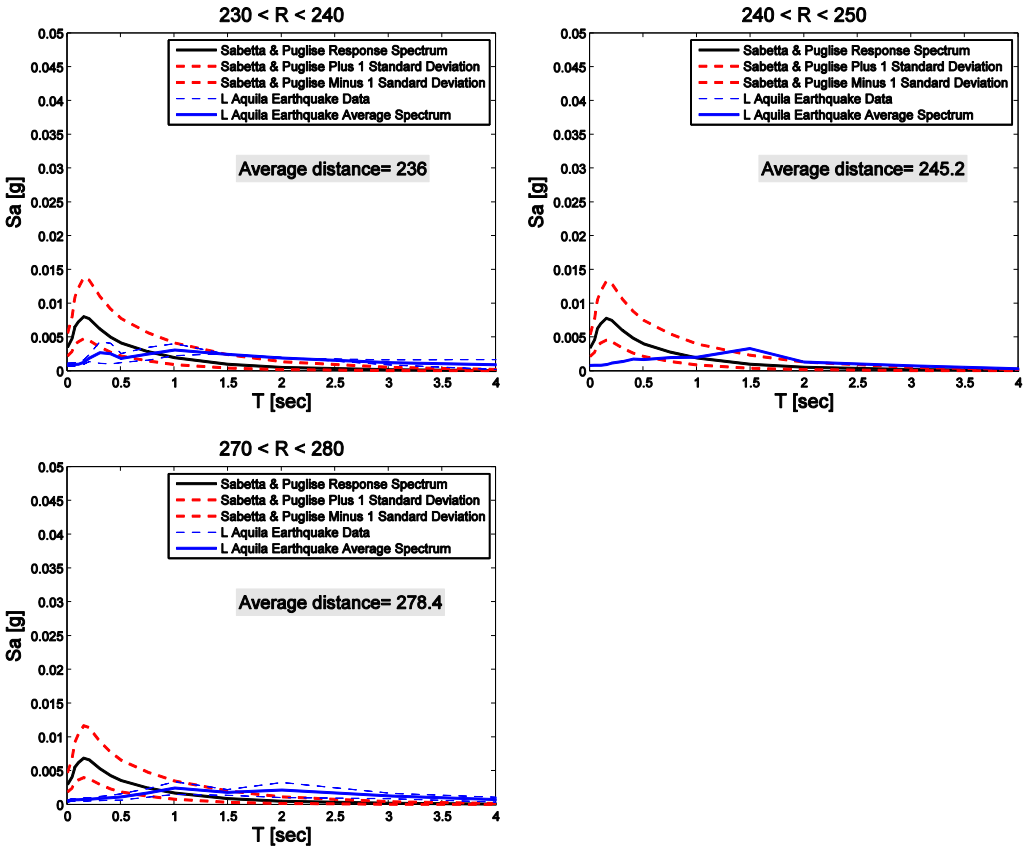

Integral parameters

Integral parameters are computed for the horizontal component with maximum PGA of each station. In particular in the following plots *Arias Intensity* (I_A) (Hancock, 2006) and *Cosenza and Manfredi Index* (I_D) (Cosenza et al., 1993) are compared with Sabetta and Peugliese (1996) and with Iervolino et al. attenuation relationship (2005) respectively.

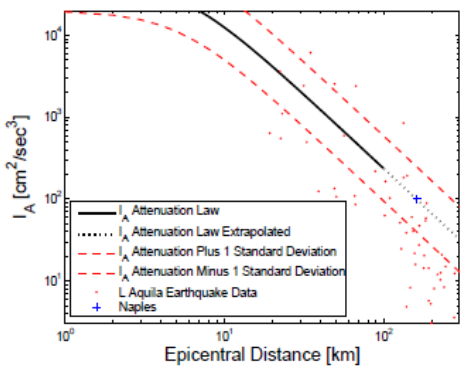

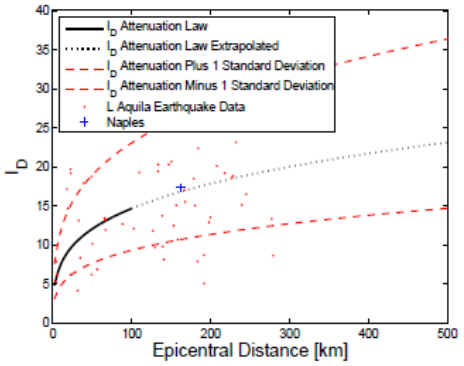

Durations computed for each record are: *Significant Duration* (Sd) and *Bracketed Duration* (Bd), the former estimated between 5% and 95% of the I_A, the latter assuming as reference value 0.05 PGA.

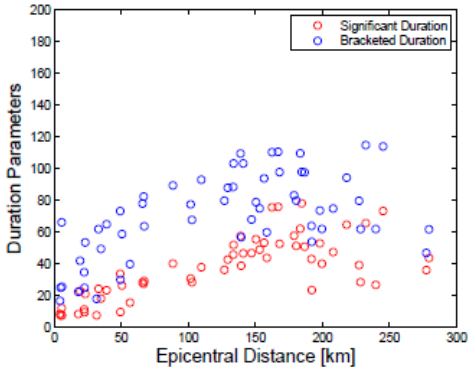

Numerical values of all plotted dimensions and further information about non linear response of SDoF systems are available at Chioccarelli et el. (2009).

References

Chioccarelli, E., De Luca, F., Iervolino, I. (2009) Preliminary Study of L'Aquila Earthquake Ground Motion Records. [Available at http://www.reluis.it/doc/pdf/Aquila/Peak_Parameters_L_Aquila_Mainshock_V5.2.pdf]

Cosenza E., Manfredi G., Ramasco R, 1993: The Use of Damage Functionals in Earthquake Engineering: A Comparison between Different Methods. Earthquake Engineering and Structural Dynamics, 22 (10), 855-868.

DPC-S4 project website, http://esse4.mi.ingv.it/.

Hancock J., 2006: The Influence of Duration and the Selection and Scaling of Accelerograms in Engineering Design and Assessment, Ph. D. Thesis.

Iervolino I., Manfredi G. and Cosenza E., 2005: Ground motion duration effects on nonlinear seismic response. Earthquake Engineering and Structural Dynamics, 35, 21-38.

Iervolino I.,Giorgio M., Galasso C. and Manfredi G., 2008: Prediction Relationships for a Vector-Valued Ground Motion Intensity Measure Accounting for Cumulative Damage Potential. 14th World Conference on Earthquake Engineering, October 12-17, Beijing, China.

Sabetta F., Pugliese A., 1996: Estimation of Response Spectra and Simulation of Nonstationary Earthquake Ground Motion. Bulletin of the Seismological Society of America, 86, 337-352.